IMAGING-MODEL-BASED VISIBILITY RECOVERY FOR SINGLE HAZY IMAGES

by

Ming-ye Ju

Supervisor: **Prof. Yingjie Jay Guo**

Co-supervisor: **Dr. Can Ding**

Dissertation submitted in fulfilment of the requirements

for the degree of

DOCTOR OF PHILOSOPHY

School of Electrical and Data Engineering
Faculty of Engineering and Information Technology
University of Technology Sydney
Sydney, NSW 2007, Australia

September 2020

ABSTRACT

Low-quality images captured in hazy weather can seriously impair the proper functioning of vision system. Although many meaningful works have been done to realize the haze removal, there are still two key issues remain unsolved. The first one is the long processing time attributed to the involved tools; the second one is existing prior employed in state-of-the-art approaches cannot be suitable for all situations. To address such problems, a series of haze removal techniques have been developed. The main contributions of this dissertation can be summarized as the following.

For efficiency, a gamma correction prior is proposed, which can be used to synthesize a homogeneous virtual transformation for an input. Relying this prior and atmospheric scattering model (ASM), a fast image dehazing method called IDGCP is developed, which converts single image haze removal into multiple images haze removal task.

Unlike the IDGCP, another solution for accelerating dehazing (VROHI) is to utilize a low complexity model, i.e., the additive haze model (AHM), to simulate the hazy image. AHM is used on remote sensing data restoration, thus the first step of VROHI is to modify the AHM to make it suitable for outdoor images. The modified AHM enables to achieve single image dehazing by finding two constants related to haze thickness.

To overcome the uneven illumination issue, the atmospheric light in ASM is replaced or redefined as a scene incident light, leading to a scene-based ASM (Sb-ASM). Based on this Sb-ASM, an effective image dehazing technique named IDSL is proposed by using a supervised learning strategy. In IDSL, the transmission

estimation is simplified to simple calculation on three components by constructing a lineal model for estimating the transmission.

According to previous Sb-ASM and the fact that inhomogeneous atmosphere phenomenon does exist in real world, a pixel-based ASM (Pb-ASM) is redefined to handle the inhomogeneous haze issue. Benefitting from this Pb-ASM, a single image dehazing algorithm called BDPK that uses Bayesian theory is developed. In BDPK, single image dehazing problem is transformed into a maximum a-posteriori probability one.

To achieve high efficiency and high quality dehazing for remote sensing (RS) data, an exponent-form ASM (Ef-ASM) is proposed by using equivalence infinitesimal theorem. By imposing the bright channel prior and dark channel prior on Ef-ASM, scene albedo restoration formula (SARF) used for RGB-channel RS image is deduced. Based on Rayleighą́s law, SARF can be expanded to achieve haze removal for multi-spectral RS data.

CERTIFICATE OF ORIGINAL AUTHORSHIP

I, Ming-ye Ju declare that this thesis, is submitted in fulfilment of the requirements for the award of the degree of DOCTOR OF PHILOSOPHY, in the Faculty of Engineering and Information Technology at the University of Technology Sydney.

This thesis is wholly my own work unless otherwise reference or acknowledged. In addition, I certify that all information sources and literature used are indicated in the thesis.

This document has not been submitted for qualifications at any other academic institution.

This research is supported by the Australian Government Research Training Program.

Signature: Production Note:
Signature removed prior to publication.

Date: 20/09/2020

ACKNOWLEDGMENTS

As a student at University of Technology Sydney (UTS), Australia, I feel extremely honored to be able to pursue a PDH degree at UTS. During that, I have gained a lot of fruitful wealth, e.g., knowledge, friendship, and perseverance, which is inseparable from each member of Big Data Technologies Centre (GBDTC). At this final stage of studying in UTS, thousands of words would fill in my heart.

I would like to express the sincerest respect and heartfelt thanks to my supervisor, Prof. Y. Jay Guo, who is expert in various fields including data processing and wireless communications, especially in antenna. He has provided me a valuable opportunity to pursue a PHD degree at UTS. As a distinguished professor, he not only gave me guidance and help in research, but also his thoughtful and resourceful thinking have made me earn a lifetime.

I would like to express the sincere appreciation and gratitude to my co-supervisor, Dr. Can Ding, who is extremely kind and also knowledgeable. His sharp thinking and smart brain always gave me a lot of suggestions and ideas in research. Without his help and suggestion, my research outputs may be much weaker than now. As a co-supervisor, he is more like a friend than a supervisor, which is quite admirable.

I would like to thank all the members of the room 607 at Global Big Data Technologies Centre (GBDTC), especially, Tian-yu Yang, Shu-ling chen, and Yi-jiang Nan for their enthusiasm and inspiration.

Finally, I especially thank my parents (Nian-feng Ju and Zai-Fang Zhang) and

my wife (Yuan-mei Fan) as well as lovely son (Mai-ting Ju) for their consistent guidance, encouragement, and love.

To My parents

&

Brother and sister

Contents

List of Figures

List of Tables

Acronyms

ASM	Atmospheric scattering model
Sb-ASM	Scene-based atmospheric scattering model
Pb-ASM	Pixel-based atmospheric scattering model
Ef-ASM	Exponent-form atmospheric scattering model
GC	Gamma correction
GCP	Gamma correction prior
GOF	Global-wise optimization function
AHM	Additive haze model
MAHM	Modified additive haze model
HTM	Haze thickness map
LFC	Low-frequency component
ALC	Atmospheric light correction
DCT	Discrete cosine transform
GEM	Guided energy model
AF	Accelerating framework
MAP	Maximum a posteriori probability
HVP	Human visual perception
AMT	Alternating minimizing technique
RS	Remote sensing
SARF	Scene albedo restoration formula
E-SARF	Expansion scene albedo restoration formula
BCP	Bright channel prior
DCP	Dark channel prior
TDCP	Translational dark channel prior

Chapter 1

Introduction

1.1 Funding

This study is derived from the National Natural Science Foundation (NSFC) “Research on Multi-source Video Compressed Sensing Methods in Wireless Sensor Networks”, and belongs to its sub-topic “Key technologies for fast defogging of images and videos”. Meanwhile, this study is also funded by Global Big Data Technologies Centre(GBDTC), University of Technology Sydney, Australia. This study focuses on exploring the fast and high-quality technique for single image haze removal, which aims to meet the real-time performance of "smart cities" as much as possible under the premise of good user experience. Consequently, how to achieve the best balance between recovery quality and processing efficiency for single image haze removal technique is the key of this study.

1.2 Motivation

With the sharp of artificial intelligence, lots of outdoor machine vision systems have been widely used in military and livelihood. Among them, “smart city” [5,6] is a comprehensive utilization of the internet of things and information processing technologies to sense key

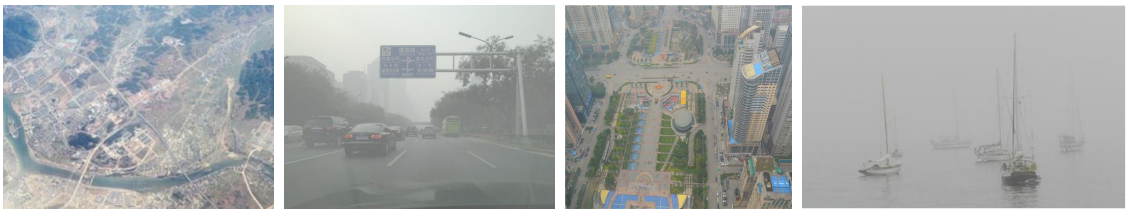

Figure 1.1: Several haze images captured by machine vision systems or cameras.

information of the city's operating system, and then makes intelligent responses according to various requirements. However, as an important perception source of "smart city", high resolution camera would suffer the interferences from turbid media in some bad weathers. This reduce the imaging accuracy of the optical sensors, thereby resulting in the reduction of visual quality of captured image, such as blurred contrast, color migration, and shortened dynamic range [7, 8]. Although infrared camera can alleviate such low-quality problems to some extent, the images it takes do not have rich color information. In addition, high cost and cumbersome maintenance also restrict its application.

Fig 1.1 shows several different types of hazy images. It can be seen from this figure that haze might interfere with machine vision systems applied in various industries, such low-quality images usually cannot support the sufficient information to meet the needs of applications or human eye. For example, many application systems in the fields of image classification [9–11], autonomous driving [12–14], and target tracking [15, 16] require the input images or videos that are taken in ideal weather, the low quality of which would have a certain impact on the accuracy of subsequent research, analysis, identification, and measurement results. In other words, the perception source affected by the haze seems like a blinded eye, which not only degrades the quality of information received from real world, but also is a great challenge to well operation of the "smart city". Therefore, image dehazing technology has extremely significance for both the people's livelihood and the military.

Currently related works may have the ability to dehaze for specific images, but there are still two key issues remain unsolved. The first one is the long processing time attributed to the involved refining tools and redundant computations, i.e., low real-time performance; the second one is the existing prior knowledge employed in state-of-the-art approaches cannot be suitable for all situations, such as the images with inhomogeneous haze or with uneven illumination, leading to the vulnerable results and visual inconsistency (low robustness capability). To overcome aforementioned problems, this dissertation develops some new techniques deploying different strategy or theory.

1.3 Organisation of Thesis

Eight chapters are included in this dissertation. Chapter 1 is introduction, Chapter 2 illustrates the background and state-of-the-art of this dissertation. Several novel dehazing techniques are developed in chapters 3 to 7 to address the facing problems of current alternatives. In specific, Chapters 3 and 4 mainly focus on dehazing efficiency while Chapters 5 to 7 are concentrate on the recovery quality. Finally, chapter 8 concludes this dissertation.

Chapter 1: Introduction. This chapter firstly introduces the motivation of image or video dehazing. Subsequently, it also presents the organization and contributions of this dissertation. The related publication of author is listed in the last part of this chapter.

Chapter 2: Background and State-of-the-Art. This chapter reviews the background and the state-of-the-art of image dedehazing, and points out the advantages and disadvantages of current available techniques.

Chapter 3: IDGCP: Image Dehazing Based on Gamma Correction Prior. This chapter mainly focuses on the the processing speed of image dehazing. In IDGCP, an input hazy image is preprocessed by the proposed gamma correction prior (GCP), resulting in a ho-

mogeneous virtual transformation of the hazy image. Then, from the original input hazy image and its virtual transformation, the depth ratio is extracted based on atmospheric scattering model (ASM). Finally, a "global-wise" strategy and a vision indicator are employed to recover the scene albedo (haze-free result), thereby restoring the high-quality hazy image from single hazy images.

Chapter 4: VROHI: Visibility Recovery for Outdoor Hazy Image Based on Modified Additive Haze Model. This chapter still aims to attain a highly efficient image dehazing method for hazy outdoor images. According to the low-frequency feature (LFC) of haze, additive haze model (AHM) is modified via gamma correction technique to make it suitable for modeling outdoor images. Relying on modified AHM (MAHM), a simple yet effective method called VROHI then is proposed to enhance the visibility of an outdoor hazy image.

Chapter 5: IDSL: Image Dehazing with Supervised Learning. This chapter redefines a scene-based ASM (Sb-ASM) to overcome the limitation of uneven illumination. Benefitting from this Sb-ASM, a fast single image dehazing algorithm called IDSL is presented by using a supervised learning strategy. In IDSL, by constructing a linear model under the visual feature, the transmission can be directly estimated. Combining the transmission and a guided energy model (GEM), scene incident light and the scene albedo can be restored via Sb-ASM. Moreover, an accelerating framework (AF) is provided to further reduce the computational complexity of dehazing procedure.

Chapter 6: BDPK: Bayesian Dehazing Using Prior Knowledge. In order to better deal with the inhomogeneous haze image, this chapter adopts a pixel-based strategy to improve the traditional ASM, denoted this model as Pb-ASM. Based on this Pb-ASM, a simple yet effective Bayesian dehazing algorithm (BDPK) is proposed based on multiple prior knowledge. In BDPK, the haze removal optimization function is first deduced by creating probability density function. Then, by combining the optimization function and

the introduced alternating minimizing technique (AMT), visually realistic result and two by-products can be obtained.

Chapter 7: Remote Sensing Image Haze Removal Using Gamma-Correction-Based Dehazing Model. In this chapter, two visibility restoration formulas are proposed for RGB-channel remote sensing (RRS) images and multi-spectral remote sensing (MSRS) images, respectively. More specifically, a exponent-form ASM (Ef-ASM) is firstly approximated, which can better address the non-uniform illumination problem in hazy images. Then, the scene albedo restoration formula (SARF) used for RRS images is obtained by imposing the existing prior knowledge on this RGDM, which enables us to simultaneously eliminate the interferences of haze and non-uniform illumination. In subsequence, according to Rayleigh's law, an expanded restoration formula (E-SARF) is further developed for MSRS data restoration.

Chapter 8: Conclusions and Future Work. This chapter briefly summarizes the conclusions for different image dehazing approaches proposed in this dissertation, and describes their shortcomings as well as the further work in the last part.

1.4 Contributions

The key contributions of this thesis are fast and robust image dehazing technology by using redefined or approximated imaging model, as well as develops more advanced dehazing mechanism. Specific contributions are outlined below:

1. A novel technique (IDGCP) to achieve highly efficiency image dehazing is developed in Chapter 3. IDGCP utilizes the proposed gamma correction prior to decrease the uncertain of ASM, which converts haze removal task as a global-wise optimization function. Unlike previous methods, IDGCP only needs to determine one unknown constant without any refining process to attain a high-quality restoration, thereby leading to significantly

reduced processing time and computation cost.

2. A new and simple way (VROHI) to realize fast outdoor images haze removal is presented in Chapter 4. In VROHI, AHM designed for hazy remote sensing data is modified via gamma correction technique to make it suitable for modeling outdoor images. Based on this modified AHM, a visibility recovery technique for single hazy images is further developed. The key of VROHI is to excavate the low-frequency component (LFC) of hazy image, and restore the scene albedo by fully utilizing the latent image feature to constrain the MAHM, which enables to determine one unknown parameter rather than estimating the transmission to achieve a haze-free result, thereby significantly improving the execution efficiency of haze removal.

3. A novel method (IDSL) to attain high-quality recovery performance for uneven illumination hazy image is developed in Chapter 5. It redefines the atmospheric light in ASM as the scene incident light, which is able to simultaneously dehazing and exposure for single images without the needs of introducing any post-proposing. More importantly, IDSL can directly calculate the transmission by using a liner model that is created according to the visual feature.

4. A novel approach (BDPK) that merges multiple prior to address the issue of inhomogeneous haze is presented in Chapter 6. BDPK is based on a pixel-based ASM (Pb-ASM) revised by breaking the scattering constant assumption. The core idea of BDPK is to convert the single image dehazing problem into a maximum a-posteriori probability (MAP) one that can be approximated as an optimization function using the existing priori constraints. To efficiently solve this optimization function, the alternating minimizing technique (AMT) is introduced, which enables us to directly restore the scene albedo.

5. Two novel scene albedo restoration formulas to simultaneously dehaze and deshadow for remote sensing data is presented in Chapter 7. A modified exponent-form ASM

(Ef-ASM) with significantly enhanced robustness is proposed for fast RRS and MSRS image dehazing. Then a scene albedo restoration formula (SARF) used for RRS images is derived by combining the existing priori constraint and this RGDM. The propsoed SARF is able to simultaneously exclude the interferences of haze and nonuniform-illumination with less calculation load. According to Rayleigh's law, an expanded restoration formula (E-SARF) is proposed to restore the MSRS data.

1.5 Publications

A List of Publications, including both accepted and submitted, based on research conducted during the author's candidature is given below.

1. **M.-Y. Ju**, C. Ding, Y. jay Guo, and D. Y. Zhang, "IDGCP: Image Dehazing Based on Gamma Correction Prior," *IEEE Transactions on Image Processing*, vol. 29, pp. 3104-3118, 2020.

2. **M.-Y. Ju**, C. Ding, D. Y. Zhang, and Y. jay Guo, "BDPK: Bayesian Dehazing Using Prior Knowledge," *IEEE Transactions on Circuits and Systems for Video Technology*, vol. 29, no. 8, pp. 2349-2362, Aug. 2019.

3. **M.-Y. Ju**, C. Ding, Y. jay Guo, and D. Y. Zhang, "Remote Sensing Image Haze Removal Using Gamma-Correction-Based Dehazing Model," *IEEE Access*, vol. 7, pp. 5250-5261, 2019.

4. **M.-Y. Ju**, C. Ding, D. Y. Zhang, and Y. jay Guo, "Gamma-Correction-Based Visibility Restoration for Single Hazy Images," *IEEE Signal Processing Letters*, vol. 25, no. 7, pp. 1084-1088, July 2018.

5. **M.-Y. Ju**, C. Ding, Z. F. Gu, and D. Y. Zhang, "Single image haze removal based

on the improved atmospheric scattering model," *Neurocomputing*, vol. 260, pp. 180-191, 2017.

6. **M.-Y. Ju**, D. Y. Zhang, and X. M. Wang, "Single image dehazing via an improved atmospheric scattering model," *The Visual Computer*, vol. 33, pp. 1613ÍC1625, 2017.

7. **M.-Y. Ju**, Z. F. Gu, D. Y. Zhang, and J. Liu, "Single image dehazing via an improved atmospheric scattering model," *IEICE Transactions on Information and Systems*, vol. E100, no. D(12), pp. 3068-3072, 2017.

8. **M.-Y. Ju** and D. Y. Zhang, "Image enhancement based on prior knowledge and atmospheric scattering model," *Acta Electronica Sinica*, vol. 45, no. 5, pp. 1218-1225, 2017.

9. **M.-Y. Ju**, D. Y. Zhang, and Y. T. Ji, "Image haze removal algorithm based on haze thickness estimation," *Acta Automatica Sinica*, vol. 42, no. 9, pp. 1367-1379, 2016.

Chapter 2

Background and State-of-the-Art

This chapter briefly illustrate the influence of atmospheric scattering during the degradation process of captured images, and introduces the traditional atmospheric scattering model (ASM). Classical image enhancement, early image dehazing techniques, and the state-of-the-art work are later reviewed, respectively. Several challenging aspects of image dehazing are highlighted in the last part.

2.1 Background

2.1.1 Formation of Hazy Images

Haze is composed of tiny particles suspended in the atmosphere, e.g., water droplets, aerosols, dust particles. In hazy weather, due to the influences of particles suspended in atmosphere, images captured by camera usually have low contrast and color shift. The reason of leading to this phenomenon is that these suspended particles and reflected light have a strong interactive effect during the shooting process of camera system, so that the scattering effect of particles in the light path propagation becomes more serious than that of haze-free conditions. These interactions can be described as scattering, absorption,

and radiation, where scattering is the most important factor of attenuating reflected light [17, 18]. Consequently, for simplicity, only the scattering effect needs to be considered when researching on degradation mechanism of the haze images [19].

2.1.2 Atmospheric Scattering Model

Physical description of scattering phenomenon is extremely complicated. The reflected light encounters interference from different, irregular, and heterogeneous suspended particles, leading to the light intensity during the propagation process would be severely reduced. Physically, each suspended particle in the atmosphere can act as an independent scatterer, and several scatterers in the optical path consistently affect subsequent particles. This process is very difficult to be simulated using a simple mathematical way. For simplicity, atmospheric scattering model (ASM) in [20] was proposed to describe the formation of a hazy image, which is expressed as

$$\boldsymbol{I}(x,y) = \boldsymbol{A} \cdot \boldsymbol{\rho}(x,y) \cdot t(x,y) + \boldsymbol{A} \cdot (1 - t(x,y)), \tag{2.1}$$

where $\boldsymbol{I}$ represents the observed hazy image, $\boldsymbol{A}$ is the global atmospheric light, $\boldsymbol{\rho}$ is scene albedo or the expected haze-free image, and t is the medium transmission. Assuming the atmospheric particle distribution is homogeneous, i.e., the atmospheric medium is evenly distributed throughout the whole image, the transmission t can be expressed as

$$t(x,y) = e^{-\beta \cdot d(x,y)}, \tag{2.2}$$

where d is the distance between the target scene and the camera (or scene depth), β is the scattering coefficient assumed to be constant. In this model, the first term on the right side of Eq. 2.1 is used to describe the direct impact of scene reflection light $\boldsymbol{A} \cdot \boldsymbol{\rho}$ from suspended particles. This term is named as direct attenuation which decays exponentially with the scene depth d. The second term called airlight, on the contrary, increases with the

scene depth d. Furthermore, Narasimhan et al. [20] also set the conditions of using ASM: 1) Illumination is evenly distributed in whole image; 2) Particles suspended in atmosphere are homogeneous. In most cases, hazy images can meet the above using conditions, which is the main reason why the model is widely used in the field of image dehazing.

2.2 State-of-the-Art

The existing image dehazing technologies can be roughly divided into the following categories: image enhancement, extra-information based dehazing, fusion-based dehazing, prior-based dehazing, and learning-based dehazing. In general, the recovery quality of the last two categories is much better than the first three ones, because the first three categories simply increase the contrast of the hazy image through some mathematical transformations instead of physically dehazing. The last two categories is based on the degradation mechanism of hazy images, real scene reconstruction is theoretically realized by estimating the structural information and other relevant necessary imaging parameters.

2.2.1 Image Enhancement

It is well-known that image haze removal is an inherently ill-posed issue since measuring scene depth is difficult for cameras. Directly employing traditional image enhancement methods [21–29] to restore the contrast of hazy images is the most intuitive and simplest way to recall the visibility in buried regions. However, these techniques are limited due to the ignored degrading mechanism. For example, histogram equalization (HE) [21] improves the global contrast of the input image by stretching the dynamic range for the color channels, yet it lacks the capability of enlarging the local visibility in each region. Although the adaptive histogram equalization (AHE) [22] overcomes the above defect, the over-enhancement may be aroused and its large computational complexity has to

be considered. Retinex methods [23–25] have made great progress through decades of development. They realize better dynamic range compression and the tonal rendition. Regrettably, the poor edge-preserving ability would give rise to halo artifacts in discontinuous areas. The core idea of gamma correction [26] and nonlinear stretching operation [27] is to revise individual pixel value without considering its neighbor content, thus their enhanced results lack visual realism. Homogeneous filtering [28] jointly utilizes the frequency filtering and gray-scale transformation to resume the target clarity of the input image, but the recovery quality relies on the parameter initialization. Detail enhancement [29] increases the high-frequency details by sharply highlighting the object contours in the whole image. Undoubtedly, it is difficult to reach a better trade-off between the over-sharpening of close-range regions and the weak sharpening of long-range ones.

2.2.2 Extra-information based Dehazing

This category makes use of the known information or multiple images to achieve haze removal. Typically, Narasimhan et al. [20] proposed the haze removal strategy using two images of the same scene taken in different atmospheric conditions. The premise of using this method is that the original input should contain the infinite far-point and near-point. Otherwise, over-saturation will be introduced into the small-depth areas. In [30], Kopf et al. exploited the given geo-referenced digital terrain and urban models to extract the scene depth, and then automatically conducted the haze removal. According to the polarization characteristics, Schechner et al. [31, 32] utilized different polarization angles from two of same scenes in order to remove the haze from the degraded images. Generally, these approaches are capable of achieving satisfactory recovery results, but these additional requirements must be hard to fulfill, which leads to their methods lack practicality in many real applications.

2.2.3 Fusion-based Dehazing

The strategy of fusion-based dehazing approaches [33–38] is to generate two or more images by processing an input image with enhancement techniques, then to merge these processed images to get a better restoration result. For instance, Ancuti and Ancuti [33] developed a visibility recovery method based on Laplacian pyramid representation. In this work, an input image was firstly preprocessed by white balance and contrast enhancement, leading to two images with different properties. Then the two images were blended to a haze-free result by using a Laplacian pyramid representation. To achieve a better recovery quality, Choi et al. [34] introduced more image features to participate the fusion process. Later in [35, 36], Galdran et al. proposed the perceptual color correction framework (PCCF) [35] and the enhancement framework named STRESS [36], which performs image dehazing from a single input. To obtain more realistic results, their team modified the previous PCCF and further developed a fusion-based variational image-dehazing (FVID) [37] to maintain high contrast in long-range regions while preserving reasonable content in the close-range ones. Another fusion-based dehazing [38] technique was designed by simply finding contrasted/saturated regions from some artificially underexposed versions of hazy input. The main advantage of fusion-based methods is the high implementation efficiency, but their performance would be deteriorated when dealing with the dark regions in hazy image. This is due to the fact that the severe dark parts of the preprocessed images are usually misjudged as the haze-free scenes.

2.2.4 Prior-based Dehazing

The core idea of prior-based dehazing [1, 3, 4, 39–56] is to utilize the potential prior or assumption to bind the atmospheric scattering model (ASM) and then formulate the dehazing task as an energy minimization one. For instance, Tan [39] successfully removed

the haze cover in an input based on the fact that clear-day image has richer contrast than the corresponding one polluted by haze. This method is very positive for dense hazy images, but the resumed colors for misty scenes are prone to be over-saturation. Fattal [40] assumed that surface shading and medium transmissions are uncorrelated in a local patch, and the haze is eliminated by utilizing independent component analysis (ICA). Obviously, this technique is challenged when the images contain less color information. Later in [41], Fattal further derived a local model that explains the color-lines meaning in vague region and used it to seek the more accurate transmission. Still, this approach may fail with the mono-color images where the notion of color-lines is trivialized. The significant contribution of the dark channel prior (DCP) [4] allows us to directly detect the rough haze thickness, thereby recovering the realistic results by refining the initial transmission using soft matting (SM) [42]. Unfortunately, this prior cannot fully suitable to the case where the scene brightness is naturally similar to the airlight. Besides, DCP's results always appear too dark and this approach is time-consuming due to the complex SM. To improve the recovery quality of the DCP, the dynamic repair strategy [1], the I_2-norm-based DCP [43], and the Laplacian-based mechanism [44] were proposed to boost the performance of estimated transmission. Fisher's linear discriminant-based scheme [3] was designed to exclude the interference of localized light sources and the scene radiance constraint [45] was provided to tackle the darkness problem of dehazed scenes. For efficiency, Huang[1] et al. [46] defined a hybrid DCP for circumventing halo effects in the recovered results, Gibson et al. [47], Huang[2] et al. [48], He[1] et al. [29], Yu et al. [49] and Xiao et al. [50] sought the replacements of SM to reduce the computational complexity, such as the median filter, improved median filter [48], guided image filtering [29] and guided joint bilateral filtering [49, 50]. From the geometric perspective of DCP, Meng et al. [51] presented the dehazing algorithm with a boundary constraint and contextual regularization. This method can thoroughly unveil the scene structures of interesting parts, yet it does not

fundamentally solve the inherent shortcomings of DCP. The strategy proposed by Chen et al. [52], which includes two modules designed using Bi-Histogram modification, is able to produce the restored results with satisfactory visual quality. Nevertheless, the rebuilt sky would suffer from serious color shift when the constant-airlight assumption is invalid. Relying on the difference structure preservation prior, He[2] et al. [53] computed the scene transmission by assuming that each patch can be linearly represented to a dictionary. Lai [54] introduced both theoretic and heuristic bounds to restrict the solution space, and designed two objectives for scene priors to excavate the optimal transmission. Kim et al. [55] estimated the transmission using the defined cost function that consists of the contrast term and the information loss term, and its dehazing effect can be adjusted by manually setting the coefficient involved in the function. Based on the color attenuation prior (CAP), Zhu et al. [56] created a linear model and determined the parameters in this model with a supervised learning method, which makes mining the depth structure task more convenient. Regrettably, the recovery quality is not guaranteed due to the unspecified scattering coefficient.

2.2.5 Learning-based Dehazing

The last category is deep-learning-based methods [1, 4, 41–44, 57–60]. Benefitting from the development of deep learning (DL) theory, haze removal can be realized by merging or learning several haze-relevant features with the DL framework. For instance, a convolutional neural network (CNN) based dehazing system, called DehazeNet, was proposed in [41] by fully utilizing the existing image priors. In subsequence, a multi-scale CNN (MSCNN) was proposed in [4] to achieve a better recovery quality by learning more useful features. However, these approaches need to introduce guided filter or fine-scale net to repair the artifacts in the estimated rough transmission. To remedy this, Li et al. [42] built a dehazing model called All-in-One Dehazing Network (AoD-Net) to directly restore

the haze-free result without the needs of estimating the transmission. In [57], a gated fusion network was proposed by learning confidence maps for three inputs processed from the original input. Similar to the second category of dehazing method, this fusion network also lacks the ability to recover the scenes misjudged as the haze-free. Moreover, most deep-learning-based techniques are only trained by synthetic hazy datasets (e.g., NYU Depth dataset [61] and Make3D dataset [62]), thus they may not uncover the latent contents for the real-world images well, especially for images with heavy haze [29]. Although a semi-supervised learning network [58] has been provided by training both synthetic and real-world hazy images, this method still performs less effective when processing the image suffers from severe haze, as discussed in [58].

2.2.6 Common Limitations

Basically, compared to image enhancement, extra-information based and fusion based dehazing, prior-based and learning-based dehazing behave a better recovery performance. This is because the first three categories only highlight the contrast information without considering the imaging mechanism of haze, while the two later categories are based on ASM, and implement haze removal by estimating the parameters in ASM. Another difference that needs to be pointed out is prior-based dehazing can have a promising result for images with heavy haze, but it may introduce the over-enhancement and over-saturation in the mist images after haze removal. On the contrary, learning-based dehazing has the ability to avoid such unfavorable phenomenon in the dehazed results, while haze residue will be found in dense haze areas. The key reason is that there are not enough samples collected from real-world to train the high-quality network for learning-based dehazing, and hand-crafted priors for image dehazing cannot be satisfied with all different types of images. Apart from the limitations mentioned in above, there are still two key issues remain unsolved in these existing techniques. The first one is that the current image pri-

ors or assumptions cannot work well on all conditions, which results in vulnerable results and visual inconsistency for some special conditions, such as inhomogeneous haze image and uneven illumination image. The second one is the long processing time attributed to the involved refining tools and redundant computations, which reduces the real-time performance of haze removal.

2.2.7 Methodology

It is well known that how to fairly evaluate our designed work is also a difficult issue. To demonstrate the superiority or achievement of the new techniques proposed in this dissertation and to better understand where the superiority comes from, qualitative and quantitative comparisons were made between the new method and the state-of-art technologies. More specifically, subjective evaluation is to firstly assess the restored image by the human vision, which is simple and reliable. To overcome the inherent shortcomings of subjective evaluation, some widely used metrics are later employed to quantitatively measure the quality of recovery. Generally, common metrics can be roughly divided into two categories: non-reference metric and reference metric. The former is a blind evaluation index method, which uses mathematical means to simply access the image in one or more features, such as information entropy, average gradient, and average brightness. The latter uses the ground truth image as a reference, and the difference between the dehazed result and the corresponding reference is used to evaluate the image quality level, such as peak signal-to-noise ratio, mean square error, and structural similarity.

2.3 Summary

This chapter firstly illustrated the formation reason of hazy images and the corresponding imaging theory, i.e., ASM. Next, the advantage and disadvantage of existing work related

to this thesis are summarized or outlined. Finally, the common limitations of current techniques are summarized into two aspects, i.e.,low robust ability, high computational complexity, and failure on inhomogeneous haze image and uneven illumination image. In following chapters, several novel methods or strategies will be proposed to address these problems.

Chapter 3

IDGCP: Image Dehazing Based on Gamma Correction Prior

To solve low real-time performance issue of current methods, this chapter proposes a novel and effective image prior, i.e., gamma correction prior (GCP). By imposing this GCP on ASM, a fast dehazing method named IDGCP employing a global-wise strategy is proposed. In IDGCP, when acquiring the transmission information, the input image is considered as a whole block rather than dividing the image into several pixels [50, 63–68], patches [40, 44, 51, 53, 56, 69, 70], scenes [71–73], or approximate objects [74–76] as illustrated in Chapter 2. A step-by-step procedure of the proposed IDGCP is as follows. First, an input hazy image is preprocessed by the proposed GCP, resulting in a homogeneous virtual transformation of the hazy image. Then, from the original input hazy image and its virtual transformation, the depth ratio is extracted based on atmospheric scattering theory. Finally, a "global-wise" strategy and a vision indicator are employed to recover the scene albedo, thereby restoring the hazy image.

3.1 Gamma Correction Prior (GCP)

The image dehazing (IDGCP) in this chapter is based on the ASM proposed by Narasimhan and Nayar [20] to describe the formation of hazy images. However, it is commonly known that ASM-based dehazing is a highly under-constrained problem since the number of unknowns is much greater than the number of available equations. This section will introduce a robust gamma correction prior (GCP) to reduce the uncertain of haze removal, which is able to get a virtual misty result under homogeneous atmosphere from the original input.

3.1.1 Motivation

In [77], gamma correction (GC) strategy was proposed by Liu et al. to preprocess hazy input image. Despite the fact that this valuable strategy can improve the overall brightness of images, it suffers from a problem that the haze cover in hazy image is also processed by GC without considering the scene depth information [71]. In specific, the preprocess can be expressed by

$$\boldsymbol{I}_p^c = (\boldsymbol{I}^c)^\Gamma, \tag{3.1}$$

where $c \in \{\mathrm{R}, \mathrm{G}, \mathrm{B}\}$ is the color channel index, $\boldsymbol{I}^c$ is the color channel of the input $\boldsymbol{I}$, $0 < \Gamma < 1$ is the correction factor, and $\boldsymbol{I}_p$ is the preprocessed result. Assuming that $\boldsymbol{I}_p$ meets the premise of using ASM, Eq. 3.1 can be transformed into

$$\begin{aligned} &\boldsymbol{A}_p^c \cdot ((\boldsymbol{\rho}^c(x,y) - 1) \cdot e^{-\beta_p \cdot d(x,y)} + 1) \\ &\quad = (\boldsymbol{A}^c)^\Gamma \cdot ((\boldsymbol{\rho}^c(x,y) - 1) \cdot e^{-\beta \cdot d(x,y)} + 1)^\Gamma, \end{aligned} \tag{3.2}$$

where β_p and $\boldsymbol{A}_p^c$ are the scattering coefficient and atmospheric light, respectively, of the color channel $\boldsymbol{I}_p^c$. Obviously, the location of atmospheric light in a given image should remain the same before and after the GC preprocess. Therefore, we let $\boldsymbol{A}_p^c = (\boldsymbol{A}^c)^\Gamma$ and

subtract $(\boldsymbol{A}^c)^\Gamma$ from each side of Eq. 3.2, which yields

$$\begin{aligned}(\boldsymbol{\rho}^c(x,y)-1)\cdot e^{-\beta_p\cdot d(x,y)}\\ =\{(\boldsymbol{\rho}^c(x,y)-1)\cdot e^{-\beta\cdot d(x,y)}+1\}^\Gamma-1.\end{aligned} \tag{3.3}$$

Considering the fact that $(\boldsymbol{\rho}^c(x,y)-1)\cdot e^{-\beta\cdot d(x,y)}$ is close to 0 in general, especially for dense hazy regions, Eq. 3.3 is then simplified according to the equivalent infinitesimal theorem.

$$\begin{aligned}(\boldsymbol{\rho}^c(x,y)-1)\cdot(e^{-\beta_p\cdot d(x,y)}-\Gamma\cdot e^{-\beta\cdot d(x,y)})\approx 0\\ \Rightarrow \beta_p\approx\beta-\tfrac{\ln(\Gamma)}{d}.\end{aligned} \tag{3.4}$$

Since the correction constant Γ is a constant and $[\ln(\Gamma)<0]$, the obtained scattering coefficient of the preprocessed image β_p decreases with scene depth d. This indicates a fact that the GC preprocess turns the homogeneous input image into an inhomogeneous virtual output image, i.e., the spatial distribution of the atmospheric medium varies throughout the image. In close-range regions with small d, β_p is higher, which leads to a brighter result than the homogenous case. In contrast, in long-range regions, the preprocessed results will appear to be darker. This problem increases the complexity of the haze removal. Even with a known scene depth, one would need to estimate the spatially variable scattering values to achieve a high performance image dehazing.

3.1.2 GCP Model

Inspired by the above conclusion, a modified preprocessing method called gamma correction prior (GCP) is proposed. The main difference between GC [77] and GCP is the fact that their outputs are inhomogeneous and homogeneous, respectively. The proposed GCP model is described as

$$\boldsymbol{I}_s^c=1-(1-\boldsymbol{I}^c)^\Gamma, \tag{3.5}$$

where $\boldsymbol{I}_s$ is the virtual result. In this process, the hazy image $\boldsymbol{I}$ get inverted first into $\mathbf{1}-\boldsymbol{I}$. Then it is processed by the GC and inverted back to get the virtual result. The

Figure 3.1: Visual observation of hazy images $\boldsymbol{I}$ (top row) and the inverted results accordingly $(\mathbf{1} - \boldsymbol{I})$ (bottom row).

inverse strategy was firstly proposed in [78] and used in image enhancement [79,80] based on an observation that the inverted low-light images look similar to hazy images. Inspired by this, we made a further assumption that the inverted hazy image $\mathbf{1} - \boldsymbol{I}$ is also visually very similar to low-light images (see Fig. 3.1). By inverting the image, the brighter regions and the darker regions are swapped. Since the inverse strategy and the GC have adverse effects on the scattering coefficient β with different scene depth, the GCP has a potential to compensate the nonlinearity in GC and stabilize the scattering coefficient β.

A large amount of experiments were conducted to investigate the GCP's ability to stabilize β. In the experiments, the input $\boldsymbol{I}$ in ASM was replaced by $\boldsymbol{I}_s$ to compute the scattering values β_s for each pixel in $\boldsymbol{I}_s$. Therefore, we have

$$\beta_s(x,y) = -\log\left(\frac{(1-(1-\boldsymbol{I}^c(x,y))^{\Gamma} - \boldsymbol{A}_s^c)}{\boldsymbol{A}_s^c \cdot (\boldsymbol{\rho}^c(x,y) - 1)}\right)/d, \tag{3.6}$$

where $\boldsymbol{A}_s^c$ is the atmospheric light of the virtual results $\boldsymbol{I}_s^c$. There are various methods can be used to locate the atmospheric light. With the overall consideration of performance and efficiency, the quad-tree subdivision method proposed in [64] was selected since it can accurately locate the atmospheric light from the most haze-opaque region by combining the average grays and gradients based assessment criteria and quad-tree subdivision.

Here we remark that one can also use other methods to estimate the atmospheric light depending on the main concerns. As illustrated in Eq. 3.6, the ground depth information (d) is required to calculate β_s. However, it is very hard to get the depth information from real world images. Therefore, in this work, the image samples were synthesized using the depth maps and ground truth images in Middlebury Stereo Datasets [81–83] according to ASM. This synthesis procedure is named as SMP in the following sections for the ease of clarify.

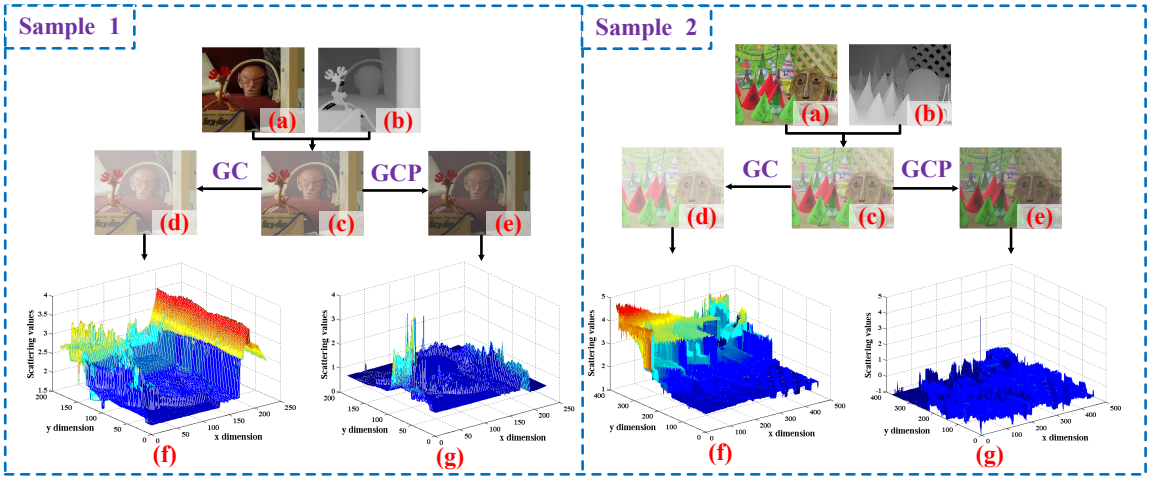

Figure 3.2: Illustration of the GC and GCP processes on two example images. **(a)** Ground truth images. **(b)** Depth maps. **(c)** Synthesized images via SMP with $\boldsymbol{A}^c = 1$ and $\beta = 1$. **(d)** Obtained virtual results using GC with $\Gamma = 0.5$. **(e)** Obtained virtual results using GCP with $\Gamma = 0.5$. **(f)** The scattering values of all pixels in (d). **(g)** The scattering values of all pixels in (e).

Fig. 3.2 shows the simulated results of two samples using GC and GCP with $\Gamma = 0.5$, as well as the computed scattering coefficients. According to Fig. 3.2(f) and 3.2(g), GCP demonstrates a significantly enhanced ability of stabilizing the scattering coefficients compared to that of GC. Fig. 3.3 illustrates the GCP process on a third sample with different Γ values. It is observed that scattering coefficients of the outputs of the GCP

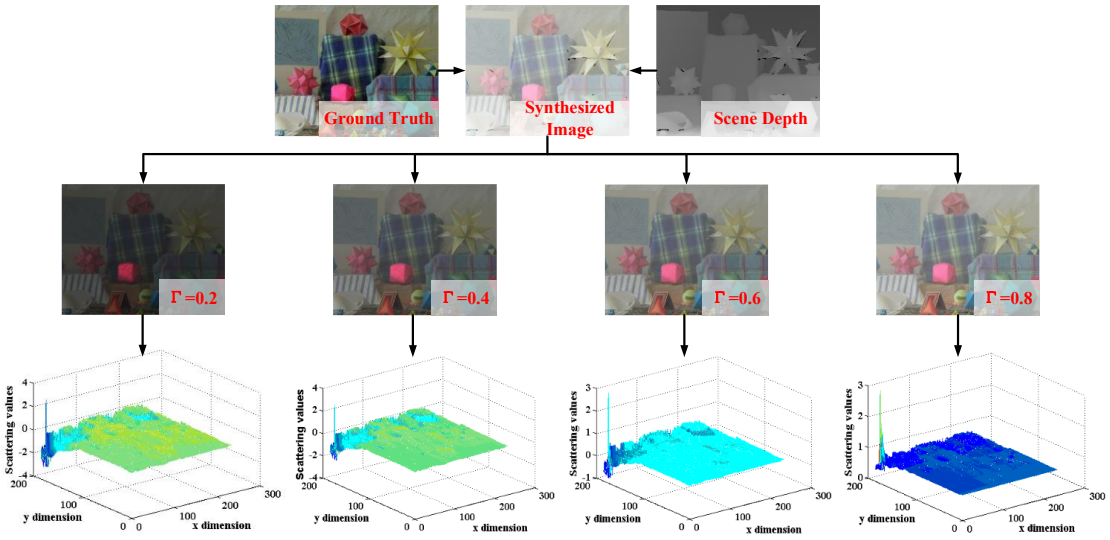

Figure 3.3: Robustness evaluation of GCP with different values of Γ. **Top row:** Sample image. **Middle row:** Virtual results using GCP with different Γ. **Bottom row**: Corresponding scattering coefficient values for all pixels.

always have a high level of stability which is independent to Γ values. Moreover, to quantitatively evaluate the robustness of GCP, a statistic indicator is defined as

$$\Psi = \sqrt{\frac{1}{|\Omega|} \sum_{(x,y)\in\Omega} (\beta_s(x,y) - \overline{\beta_s})^2}, \tag{3.7}$$

where $\overline{\beta_s}$ is the average value of β_s, Ω and $|\Omega|$ are the image index set and image resolution, respectively. Generally, the smaller the value of Ψ is, the more stable the scattering coefficients, which indicates that the GCP is more reliable. The calculated Ψ values of 200 different samples processed by GCP are shown in Fig. 3.4(a), and the statistic histogram is shown in Fig. 3.4(b). It is observed that 90% of the samples have small Ψ values ≤ 0.3, which validates the reliability of the proposed GCP. It can be summarized that the proposed GCP process overcomes the limitation of the GC since the homogeneity of input images is well maintained in the output images.

It should be noted that, although the proposed GCP is a modification of GC, they have

different targets. GC can and is only used to increase the contrast of a hazy image, whereas GCP allows us to obtain a virtual misty image from a single hazy image. Combining the input hazy image with the obtained virtual image, single image dehazing problem can be converted into multiple image haze removal. The main benefit is to ease the uncertainty of depth information, which significantly facilitates the subsequent image dehazing process based on ASM.

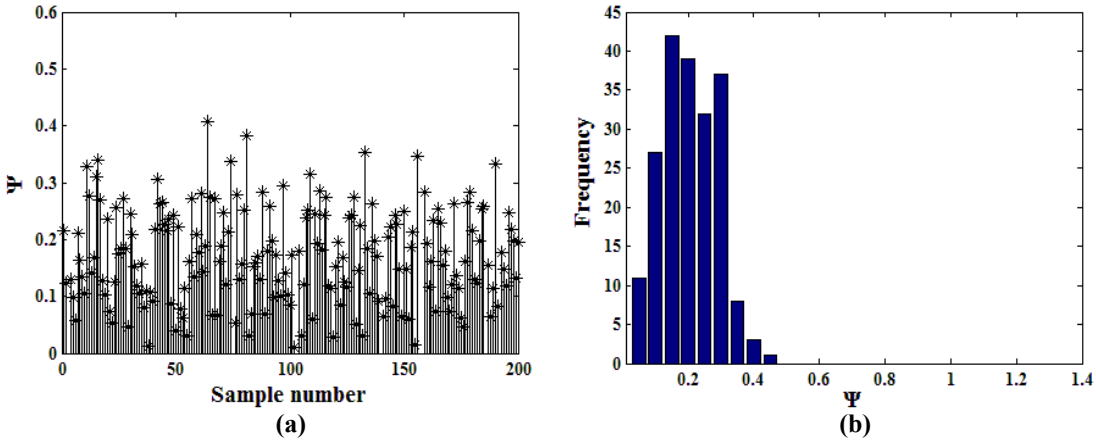

Figure 3.4: Statistics of the index Ψ. **(a):** The values of Ψ over 200 test samples. **(b):** The statistical histogram corresponding to the left statistics.

3.2 Image Dehazing Based on GCP (IDGCP)

Based on the ASM proposed in [20] and the GCP described in the previous section, a fast image dehazing method called IDGCP is developed based on a global-wise strategy. The proposed method can extract the depth ratio efficiently by fully leveraging the latent relation of the image structure, thereby attaining haze-free results. Only two major modules are utilized in IDGCP, i.e., the depth ratio extraction module and the image

recovery module.

3.2.1 Extracting Depth Ratio

The fundamental idea of IDGCP is to mine the depth structure information from the two hazy images: one is the hazy input and the other is the virtual hazy image obtained from GCP. The first step is to utilize GCP to get the virtual image $\boldsymbol{I}_s$ from the original input $\boldsymbol{I}$. Then, two imaging equations for $\boldsymbol{I}_s$ and $\boldsymbol{I}$ are obtained based on the ASM and the structure invariance principle described in [20].

$$\begin{aligned} \boldsymbol{I}^c(x,y) &= \boldsymbol{A}^c \cdot \boldsymbol{\rho}(x,y) \cdot e^{-\beta \cdot d(x,y)} + \boldsymbol{A}^c \cdot (1 - e^{-\beta \cdot d(x,y)}) \\ \boldsymbol{I}_s^c(x,y) &= \boldsymbol{A}_s^c \cdot \boldsymbol{\rho}(x,y) \cdot e^{-\beta_s \cdot d(x,y)} + \boldsymbol{A}_s^c \cdot (1 - e^{-\beta_s \cdot d(x,y)}). \end{aligned} \tag{3.8}$$

By solving this equation set, the scene depth can be obtained as

$$d = \frac{-\ln \frac{\max(\boldsymbol{A}^c - \boldsymbol{I}^c, \epsilon_1)}{\max(\boldsymbol{A}_s^c - \boldsymbol{I}_s^c, \epsilon_2)} - \ln \frac{\boldsymbol{A}_s^c}{\boldsymbol{A}^c}}{\beta - \beta_s}, \tag{3.9}$$

where ϵ_1 and ϵ_2 are very small positive constants, ϵ_1 is introduced to avoid the numerator to exceed the function definition field, and ϵ_2 is introduced to make sure the denominator is not zero. It is further assumed that the weather condition does not change spatially, thus we have

$$d = \frac{1}{\beta - \beta_s} \cdot d_0 \propto d_0 = -\ln \frac{\max(\boldsymbol{A}^c - \boldsymbol{I}^c, \epsilon_1)}{\max(\boldsymbol{A}_s^c - \boldsymbol{I}_s^c, \epsilon_2)} - \ln \frac{\boldsymbol{A}_s^c}{\boldsymbol{A}^c}. \tag{3.10}$$

Note that the depth ratio d_0 is a known component since $\boldsymbol{A}_s^c$ and $\boldsymbol{A}^c$ can be easily obtained [29]. In this work, we selected the blue channels $\boldsymbol{I}^B$ and $\boldsymbol{I}_s^B$ for the calculation of d_0. We remark that similar results can also be obtained by adopting the red channels or the green channels. Several examples of the calculated depth ratios are illustrated in Fig. 3.5, demonstrating a fact that the depth ratio maps obtained are sharp and exactly in consistence with our intuition.

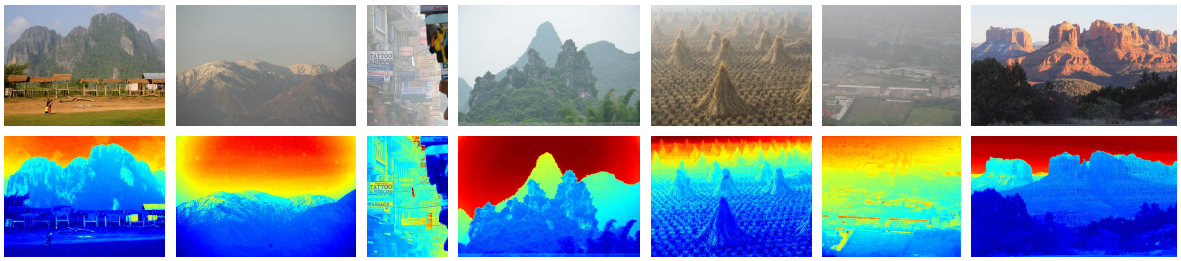

Figure 3.5: Example images and the estimated depth ratio maps. **Top row:** Input hazy images. **Bottom row:** Scene depth ratio maps obtained using Eq. 3.10.

3.2.2 Scene Albedo Recovery Using Global-wise Strategy

The dehazed image $\boldsymbol{\rho}^c$ can be obtained by substituting Eqs. 2.1 and 3.10 into ASM (Eq. 2.1), which yields

$$\boldsymbol{\rho}^c = \frac{\boldsymbol{I}^c - \boldsymbol{A}^c}{\boldsymbol{A}^c \cdot e^{-\frac{\beta}{\beta-\beta_s}\cdot d_0}} + 1. \tag{3.11}$$

To avoid pixel overflow, it is set that $0 \leq \boldsymbol{\rho}^c \leq 1$. Therefore, the final expression used for restoring the scene albedo can be rewritten as

$$\begin{aligned} \boldsymbol{\rho}^c &= \text{dehaze}(\theta, \boldsymbol{I}^c, \boldsymbol{A}^c, d_0) \\ &= \min(\max(\frac{\boldsymbol{I}^c - \boldsymbol{A}^c}{\boldsymbol{A}^c \cdot e^{-\theta \cdot d_0}}) + 1, 0), 1), \end{aligned} \tag{3.12}$$

where dehaze$(\cdot)$ is the abbreviation of albedo restoring function. Note that dehaze$(\cdot)$ is a function of four parameters, where $\boldsymbol{I}^c$ is the input, $\boldsymbol{A}^c$ can be easily calculated according to [64], d_0 is the depth ratio obtained in the previous subsection, and $\theta = \beta/(\beta - \beta_s)$ is the only unknown parameter. Determining the right value of θ to get the transmission map $t = e^{-\theta \cdot d_0}$ is critical to the dehazing quality. To estimate the value of θ with low complexity but high accuracy, a global-wise optimization function is designed as

$$\theta = \text{argmin}\{\sum_c f(\text{dehaze}(\theta, (\boldsymbol{I}^c)\downarrow^n, \boldsymbol{A}^c, (d_0)\downarrow^n))\}, \tag{3.13}$$

where $f(\cdot)$ represents a vision indicator designed via single or multiple image prior, and $\downarrow^n$ is a down-sampling operator with coefficient n. Numerous experiments show that

generally a down-sampled image with an approximate size of [100 × 100] is good enough to determine the value of θ since it still holds the original important features of the input image. Therefore, in this work, the coefficient n is adaptively defined as

$$n = \frac{max(w, l)}{100}, \tag{3.14}$$

where w and l are the width and length of input image, respectively. Considering that the goal of image dehazing is to improve the visual contrast of the degraded image while avoiding excessive loss of information [55], the vision indicator is defined as

$$f(\boldsymbol{In}) = -\sum_{c} \phi(\bigtriangledown(\boldsymbol{In}^c)) + \lambda \cdot \sum_{c} \varphi(\boldsymbol{In}^c), \tag{3.15}$$

where $\boldsymbol{In}$ is the image to be evaluated, $0 \leq \lambda < 1$ is the regulation parameter, $\phi(\cdot)$ is the mean operator, and $\varphi(\cdot)$ is an operator to compute the percentage of pixels that are completely black or white. In Eq. 3.15, the first term ensures the image $\boldsymbol{In}$ has rich texture information, and the second term is used to measure the lost information cost.

Note that Eq. 3.13 is a one-dimensional optimization function. In this work, Fibonacci method (FM) is adopted to solve Eq. 3.13 since it is able to gradually narrow the search interval for one-dimensional optimization problem until convergence condition is satisfied. In specific, the initial interval and the final interval length are defined as $[a_1, a_2]$ and ε, respectively. Once the coefficient θ is determined, the scene albedo can be directly recovered by Eq. 14. For clarity, the entire procedure of IDGCP is outlined in Algorithm 3.1.

It should be pointed out that all the other dehazing methods are based on pixel-wise, patch-wise, scene-wise, nonlocal-wise, and learning-wise strategies. The proposed global-wise strategy is the second key contribution in this paper, which enables us to attain a high-quality restoration by only determining one unknown constant.

Algorithm 1 IDGCP

Input: Hazy Input $\boldsymbol{I}$

Pre-set parameters: $\epsilon_1 = \epsilon_2 = 10^{-5}$, $\lambda = 0.5$, $\Gamma = 0.5$, $[a_1, a_2] = [0, 6]$, $\varepsilon = 0.1$

Do the job:

1. Simulate the virtual image using GCP (Eq. 3.5).
2. Locate the atmospheric lights of the original input and the virtual image via quad-tree subdivision method [64].
3. Extract the rough depth ratio d_0 via Eq. 3.10.
4. Determine the constant θ via Eq. 3.13 with FM.
5. Restore the scene albedo via Eq. 3.12.

Output: Recovery result $\boldsymbol{\rho}$.

3.3 Performance Evaluation

To demonstrate the superiority of IDGCP and to better understand where the superiority comes from, a series of experiments were conducted and comparisons were made between IDGCP and the state-of-the-art technologies. All the experiments were implemented in MATLAB2010 environment on a PC with Intel(R) Core(Tm) i5-4210U CPU@ 1.70GHz 8.00 GB RAM. The parameters used in the compared dehazing methods were also optimized according to the corresponding references.

3.3.1 Initial Parameter Setup and Robustness Evaluation

As listed in Algorithm 3.1, there are several parameters that are initialized manually in the proposed IDGCP. They are the positive constants ϵ_1 and ϵ_2, the correction factor Γ,

the regulation constant λ, the FM's initial interval $[a_1, a_2]$, and the FM's final interval width ε. Note that the pre-set parameters illustrated in Algorithm 3.1 is an optimized combination which works for all kinds of hazy inputs, which can be validated by the subsequent experiments. Once their values are determined, it can be used on all images straightforwardly. In this subsection, how the values of the parameters are chosen will be described and their effects on the performance will be discussed.

The parameters ϵ_1 and ϵ_2 are introduced only to ensure that Eq. 3.10 remains valid. As long as they are small positive constants, their values have no effect to the final results. In this work, both ϵ_1 and ϵ_2 are set to be 10^{-5}. The correction factor Γ is a parameter of the proposed GCP (see Eq. 3.5). According to the previous analysis in subsection 3.1.2 and the experiment results illustrated in Fig. 3.3, the scattering coefficients β_s of the output virtual image always exhibit a high level of stability throughout the image, which is independent to Γ values. As long as β_s can be seen as a constant, the GCP is valid. Although different values of Γ leads to different scattering coefficients β_s (see Fig. 3.3), it almost has no effect on the quality of the final dehazed results. Fig. 3.6 shows the IDGCP dehaze results on an example images with different Γ values. During the experiment, the other parameters were fixed at the values illustrated in Algorithm 3.1. As shown in the figure, there is barely any difference between the dehazed results when Γ has different values. However, different values of Γ lead to different values of θ (Eq. 3.13) and affect the processing time. The processing time is slightly different with different values of Γ because the FM used to determine the value of θ needs different numbers of iterations. For example, as shown in Fig. 3.6, when $\Gamma = 0.6$, the number of iteration to find θ is 8; when $\Gamma = 0.8$, the number of iteration to find θ is 9. However, the Γ value's effect on the processing time is minor. In this work, Γ is set to be 0.5.

The regulation constant λ is introduced in the vision indicator (Eq. 3.15) to correctly determine the value of θ. To investigate how λ affects the recovery performance, a recovery

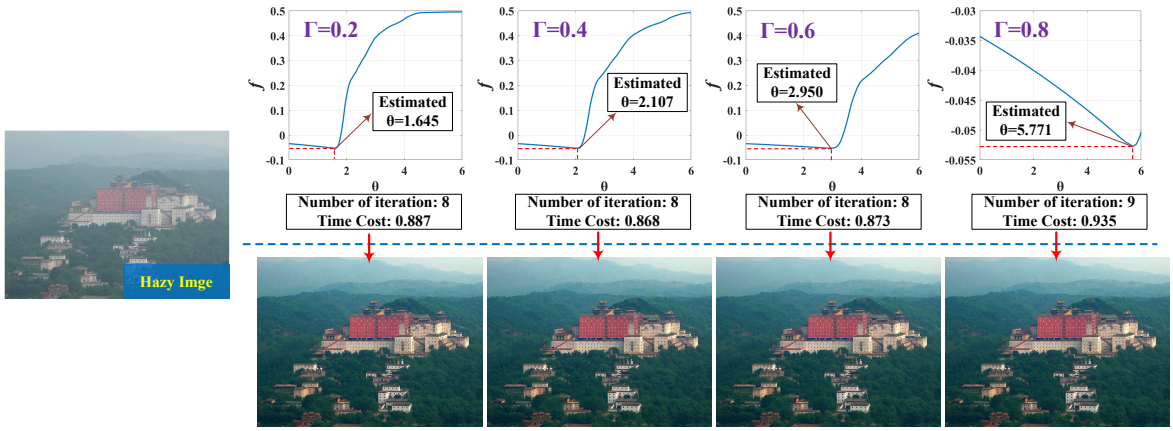

Figure 3.6: IDGCP robustness evaluation of the pre-set parameter Γ on an example hazy images. **Top:** Curves of f with respect to θ using different values of Γ. **Bottom:** Results of IDGCP with different values of Γ.

quality test was conducted with different values of λ. Fig. 3.7 shows the results restored via IDGCP from three different types of hazy images with different values of λ when other parameters are fixed at the values listed in Algorithm 3.1. As shown in the figure, too small λ results in over-saturation in the mist image, whereas too large λ can not completely uncover the scene content in the image with dense haze. As a tradeoff, $\lambda = 0.5$ is selected.

Experiments on numerous sample images demonstrate that once Γ and λ are fixed, the resultant θ values of the images will always lie in a specific confidence interval. When $\Gamma = 0.5$ and $\lambda = 0.5$, the confidence interval is $[0, 6]$. For example, as shown in Fig. 3.7, the θ values of the three typical images are 0.043, 1.463, and 4.64. More test results can be found on the authors' website[1]. Therefore, to reduce the processing time of IDGCP, the initial interval and final interval width used in FM are set to be $[a_1, a_2] = [0, 6]$ and $\varepsilon = 0.1$, respectively.

[1] `https://www.researchgate.net/profile/Mingye_Ju`

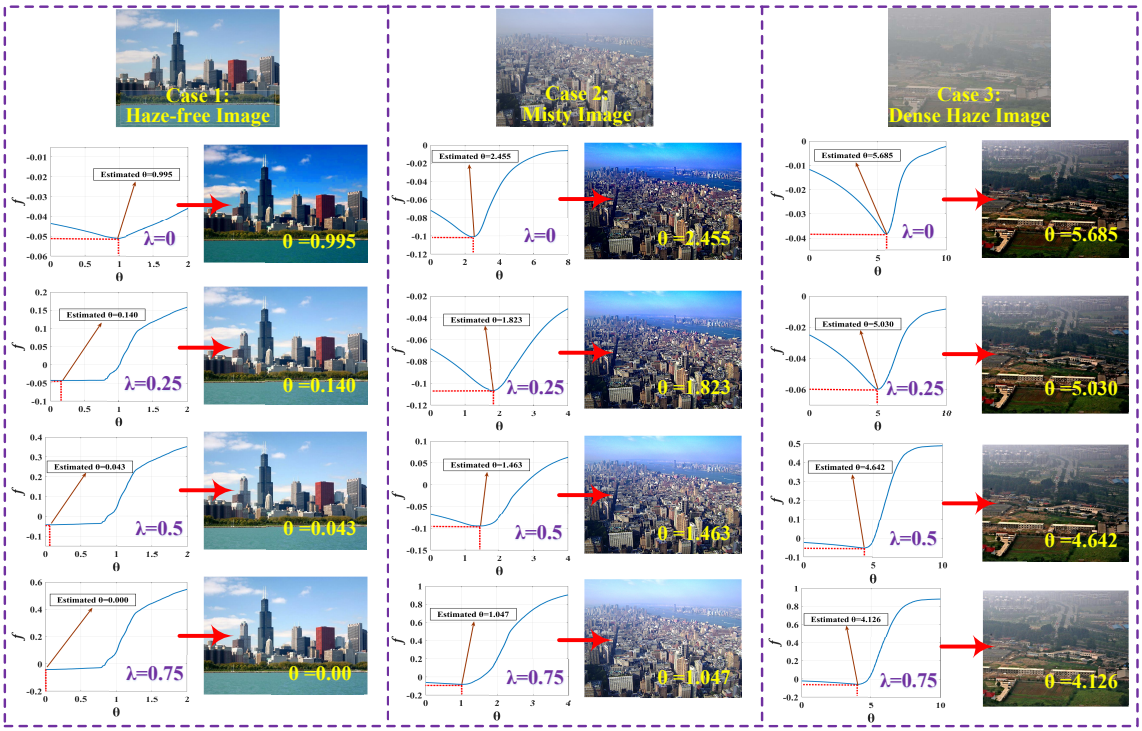

Figure 3.7: IDGCP robustness evaluation of the pre-set parameter λ on three example images.

3.3.2 IDGCP Performance Demonstration

3.3.2.1 Evaluation of IDGCP on different sample images

First, several sample images were selected from [40] to test the performance of IDGCP. The original sample images, the restored results, and the transmission maps are depicted in Fig. 3.8 to intuitively demonstrate the capability of IDGCP. As observed in the figure, the proposed IDGCP thoroughly removes the haze and unveils reasonable scene details in hazy regions, while the transmission maps are quite consistent with the objective reality of the real world. Although these estimated transmission maps seem to have a few undesirable or illogical texture details, the visual quality of the recovered results shown in Fig. 3.8 is already more than sufficient for most cases. Here we remark that further blurring the

Figure 3.8: Image restoration results using the proposed IDGCP.

texture details in transmission maps can improve the restoration quality. However, in this work, the blurring step is omitted as the quality is already satisfactory and the efficiency is the main concern.

3.3.2.2 Evaluation of the GCP

The first step of IDGCP is to obtain the depth ratio using GCP. A sharp depth ratio is the premise of the final accurate restoration. In Fig. 3.9, we compare the obtained scene depth from GCP and that from the widely used color attenuation prior (CAP) [56]. According to the figure, although CAP has a better local-constant feature than GCP (owing to the abandoned blurring step and the ignored locally constant assumption in IDGCP), it is not able to achieve a balance between the over-saturation problem in close-range regions and a complete haze removal in long-range regions by changing the scattering coefficient settings (see the zoom-in patches in Figs. 3.9(c) to 3.9(f)). In contrast, GCP is able to solve this problem and achieve satisfactory results by selecting an appropriate value of constant θ (see the zoom-in patches in Fig. 3.9(k)).

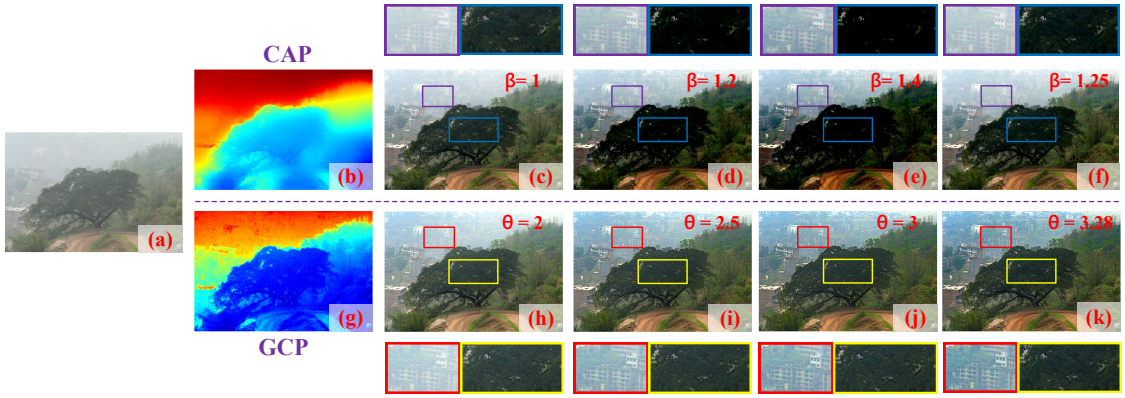

Figure 3.9: Comparison of the scene depth obtained by the widely used CAP proposed in [1] and by the proposed GCP. **(a):** Input hazy image. **(b):** Depth map obtained via CAP. **(c)-(f):** Recovered images with different scattering coefficients of β =1, 1.2, 1.4, and 1.25, respectively. $\beta = 1.25$ was determined via the proposed vision indicator. **(g):** Depth map obtained via GCP. **(h)-(k):** Recovered images with different constants of $\theta = 2, 2.5, 3$, and 3.28, respectively. $\theta = 3.28$ was determined via the proposed global optimization strategy.

3.3.2.3 Evaluation of the global-wise strategy

The pixel-wise, patch-wise, scene-wise, and nonlocal-wise strategies that are designed for haze removal, as aforementioned, involve enormous redundant computations due to the spatial similarity in natural image. Fig. 3.10 illustrates the dehazing procedure and the associated time cost of the proposed IDGCP (global-wise) and other recently published works, including FID [50] (pixel-wise), DCP [4] + GF [29] (patch-wise), DIM (scene-wise) [71], and NID (nonlocal-wise) [74]. For fairness of comparison, the redefined scene luminance of DIM was replaced by the atmospheric light, and the atmospheric light of FID, DCP, DIM, NID, and IDGCP were set to have the same value in initialization. As observed in Fig. 3.10, it is noticed that the transmission maps (or depth maps) estimated via pixel-wise, patch-wise, scene-wise, and nonlocal-wise strategies fail to preserve the edge

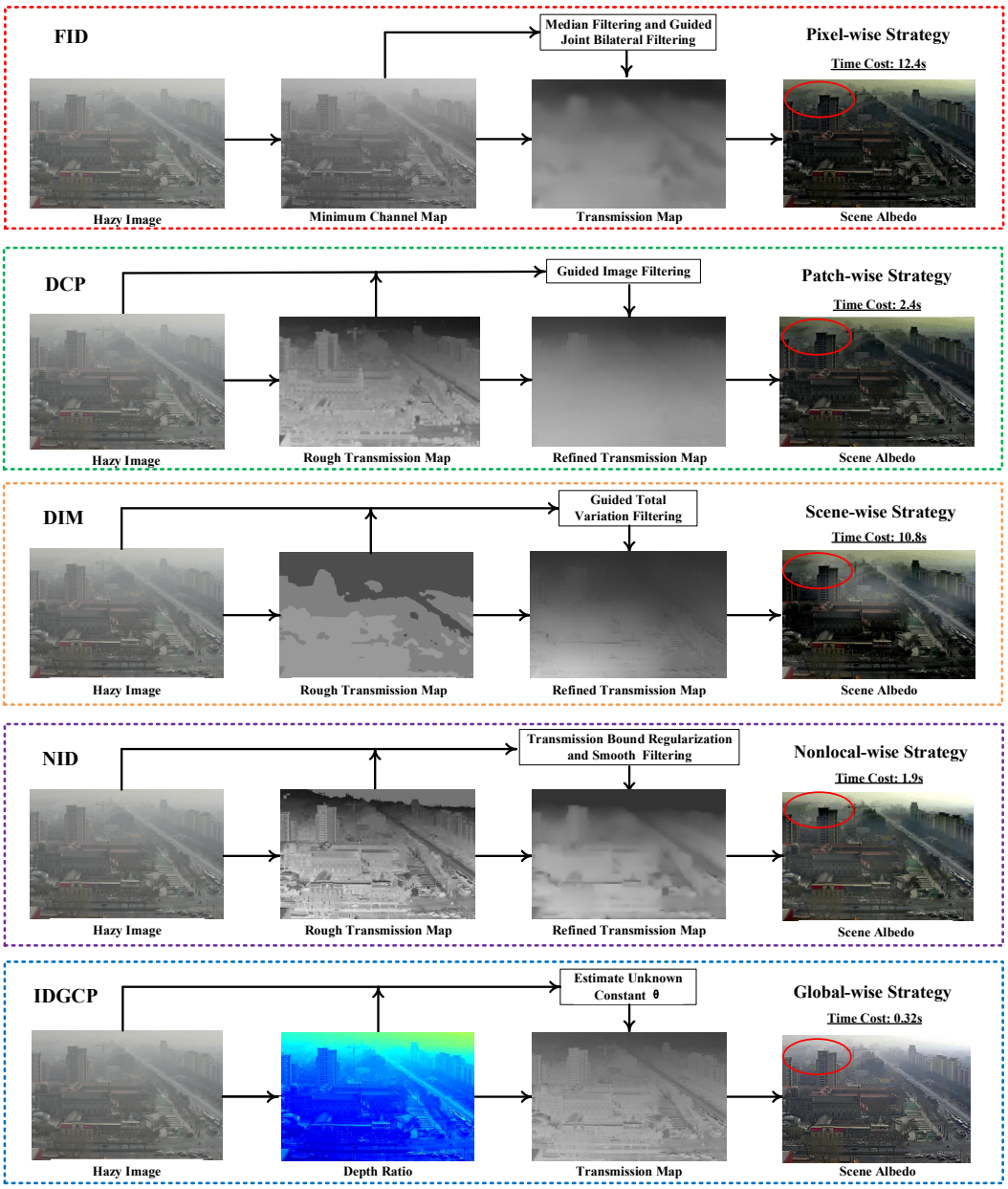

Figure 3.10: Overview of image dehazing procedures using FID, DCP + GF, DIM, NID, and the proposed IDGCP. (Note that the atmospheric light is regarded as a known constant here).

structure of the original depth or contain many unreasonable texture details, which means that a subsequent refine-transmission step is required. In comparison, IDGCP utilizes the

global-wise strategy, which only needs to estimate one unknown constant. This leads to a significant reduction in processing time and computation cost. More importantly, since an entire image has more information than a part of the image, the global-wise strategy can get a more visually comfortable result (as highlighted by red circles in Fig. 3.10).

3.3.3 Qualitative Comparison

3.3.3.1 Comparison with state-of-the-art dehazing techniques on challenging real-world images

Almost all the mainstream dehazing techniques are able to get satisfactory restoration results from general outdoor hazy images as discussed in [65]. Sometimes it is hard to tell the differences of the restoration quality using different techniques. In this work, we adopted five widely used challenging real-world benchmark images (collected in [56]) with large white or gray scenes to facilitate the comparison as shown in Fig. 3.11. The selected pictures are challenging to dehaze because most of the algorithms are sensitive to the gray-white color. The five hazy images are given in Fig. 3.11(a). The dehazed results using DEFADE (fusion-wise) [34], FVR (pixel-wise) [63], BCCR (patch-wise) [51], IDAET (scene-wise) [73], IDHL (nonlocal-wise) [75], MSCNN (learning-wise) [69], DehazeNet (learning-wise) [84], and the proposed IDGCP (global-wise) are illustrated in Figs. 3.11(b) to 3.11(i), respectively. Some zoom-in detailed are shown in Fig. 3.11(j) for a clearer comparison.

In Fig. 3.11(b), it is observed that DEFADE can recognize rough haze regions and increase visual visibility for most of the hazy samples, but its performance is deteriorated when dealing with dark regions (highlighted in the zoom-in subfigure). This is attributed to the fact that the severe dark aspects of the preprocessed images play a dominate role when performing the multi-scale fusion operation. As shown in Fig. 3.11(c), FVR is able

to recover the hidden details of hazy regions, whereas the restoration scenes are quite deviate from the real ones that expected. The reason is that the atmospheric veil used in FVR is a particular case of DCP, and the overestimation transmission problem gets more severe. In addition, for the third picture, halo artifact appears near the depth jumps (see the corresponding zoom-in part in Fig. 3.11(j)). This is due to the poor structure-preserving performance of the median filter. Similarly, we notice that BCCR has the same drawback, as shown in Fig. 3.11(d), because of the fact that the inherent defect of DCP is not addressed and the noise amplification phenomenon still exists in the white regions of the images (as highlighted in Fig. 3.11(j)). For IDAET as shown in Fig. 3.11(e), it fails to attain promising results for the dense regions. The reason is that the dense regions are misjudged as “sky" by the transmission compensation module used in this method. IDHL avoids the haze residue for the dense regions by introducing the lower bound of transmission, as seen in Fig. 3.11(f). However, the over-saturation was unfortunately introduced in recovered result (see the purple patch in Fig. 3.11(j)). This may be caused by the detection failure of similar colors. Although MSCNN and DehazeNet can avoid the over-enhancement problem to some extent (see Fig. 3.11(g) and Fig. 3.11(h)), haze residue can be found in their dehazed results (detailed in the yellow and green patches). This is mainly attributed to the fact that the training samples for the deep dehazing methods are usually artificially synthesized images rather than real-world images, thus limiting the performance of the learning-wise dehazing methods. Compared with these state-of-the-art techniques, IDGCP is free from over-enhancement, halo effect, and over-saturation problems that degrade the image quality. As displayed in Fig. 3.11(i), the sky regions and the clouds in the recovery images are very natural, and the texture details of the targets are well enhanced.

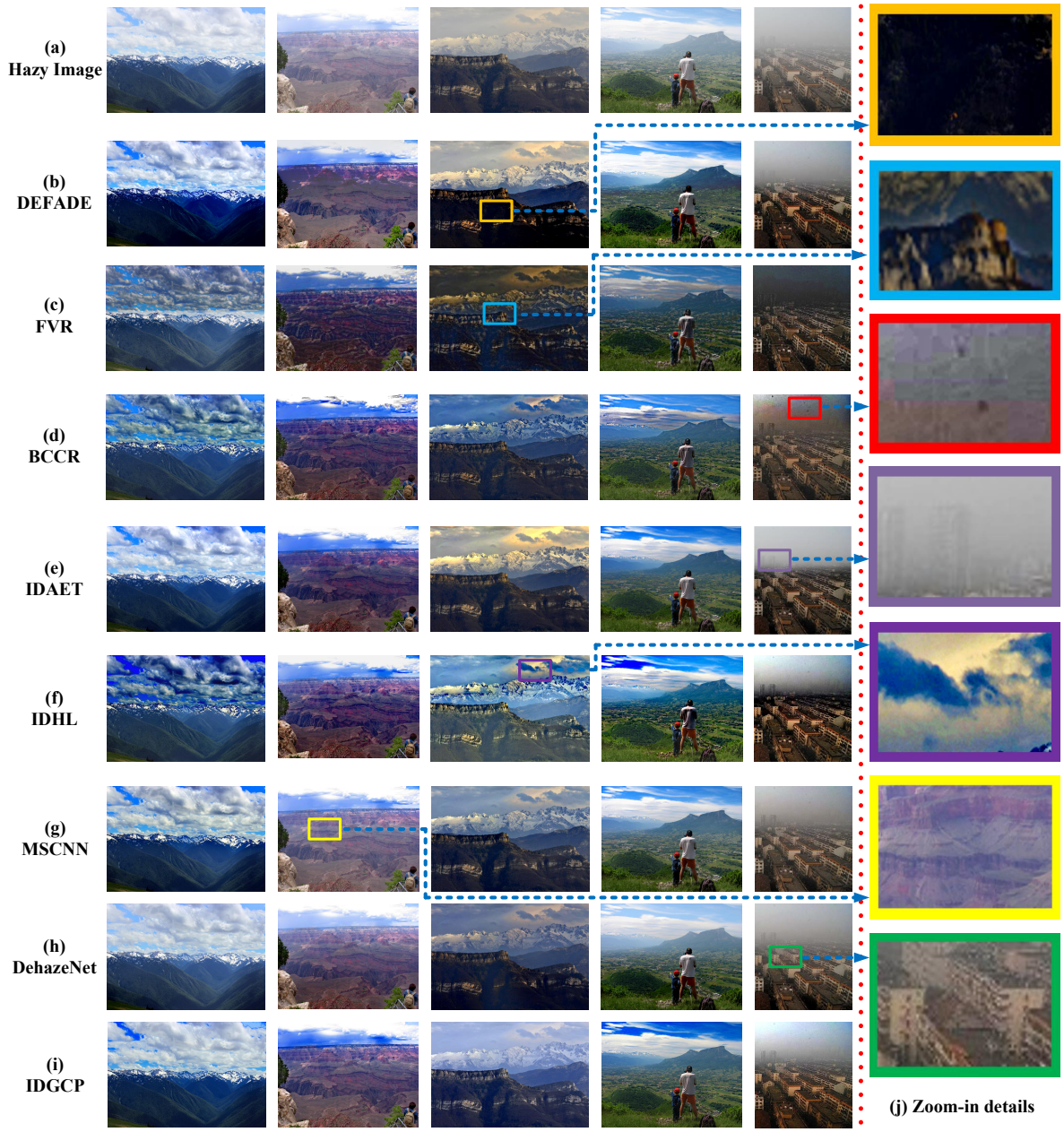

Figure 3.11: Qualitative comparison between the proposed IDGCP and other state-of-the-art techniques on five benchmark images.

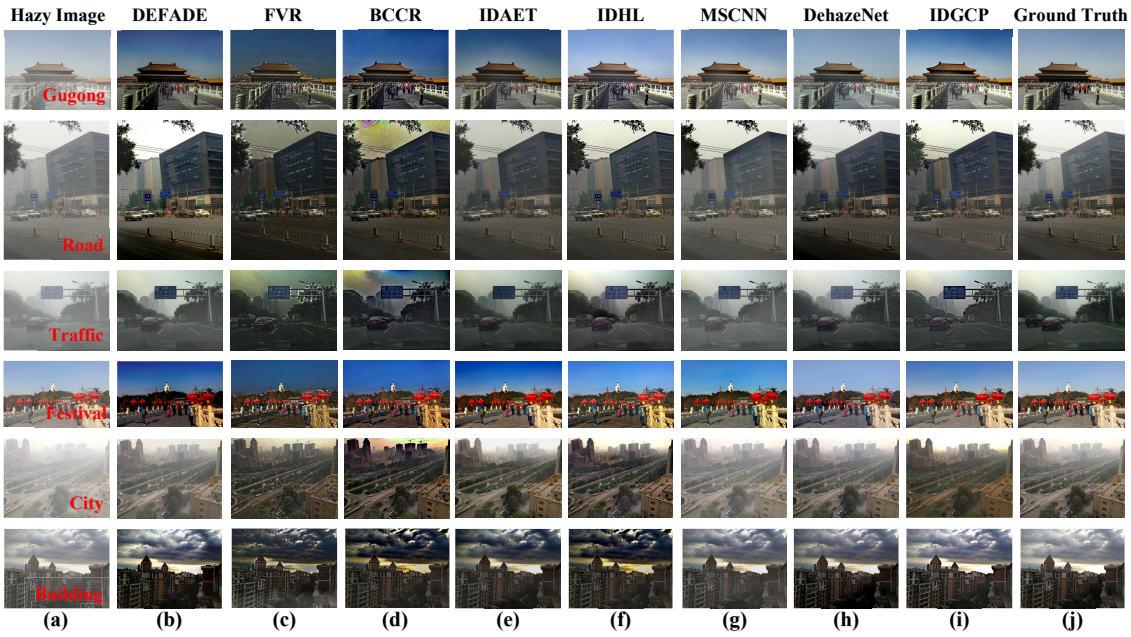

Figure 3.12: Qualitative comparison between the proposed IDGCP and other state-of-the-art techniques on synthetic images.

3.3.3.2 Comparison with state-of-the-art dehazing techniques on synthesized images

Assessing dehazing techniques is a very tricky task since it is difficult to get haze-free reference images from real-world. The comparisons between IDGCP and state-of-the-art techniques were further conducted on the Realistic Single Image Dehazing (RESIDE) dataset [85] consisting of both hazy images and the corresponding haze-free images. Figs. 3.12(a) and 3.12(j) give the hazy images and the corresponding ground truth images, respectively. Figs. 3.12(b) to 3.12(i) show the recovered results based on the synthesized hazy images using DEFADE, FVR, BCCR, IDAET, IDHL, MSCNN, DehazeNet, and IDGCP, respectively. In Figs. 3.12(b) to 3.12(d), the restored results using DEFADE, FVR, and BCCR can clearly indicate the target contour for the given examples, but their restored colors are generally over-saturated (see the festival image and the building

image). As shown in Figs. 3.12(e) and 3.12(f), the over-enhancement still exists in the festival images after the dehazing process of IDAET and IDHL. According to Figs. 3.12(g) and 3.12(h), MSCNN and DehazeNet are capable of producing the haze-free results with vivid color and necessary details for mist scenes. However, they lack the ability to uncover the details for the scenes with dense haze (see the city image). In comparison, IDGCP's results do not show any negative effects and can maintain the original tones of most scene targets as shown in Fig. 3.12(i).

3.3.4 Quantitative Comparison on Synthetic Images

In order to guarantee the fairness of the qualitative comparison in Fig. 3.12, quantitative comparisons were made on four commonly used evaluation indexes. The selected performance indexes are fog aware density evaluator (FADE) [34], edges newly visible after restoration (e) [86], structural similarity (SSIM) [87], and mean square error (MSE). The calculated values of these indexes for the four images shown in Fig. 3.12 are summarized in Table 3.1. Note that a larger e or a smaller FADE represents a lower perceptual haze density; a larger SSIM means a better structure similarity between the dehazed result and the ground truth image; a lower MSE indicates that the recovered image is more acceptable. It can be concluded from the table that the proposed IDGCP has the highest average value of SSIM and the lowest average value of MSE among all the methods, which means that IDGCP's results are more similar to the ground truth compared with the results obtained by other methods. Although IDGCP has a higher average value of FADE and a lower average value of e than FVR, BCCR, and IDHL, the results produced by these methods appear to be over-saturated and too dark. This could further reduce the perceptual fog density of the dehazed images and increase the pseudo-edge of scene targets.

Table 3.1: Quantitative Comparison of Dehazed Images Shown in Fig. 3.12 using FADE, e, SSIM, and MSE

Test Criterion	Image	DEFADE	FVR	BCCR	IDAET	IDHL	MSCNN	DehazeNet	IDGCP
FADE	Gugong	0.4201	0.5012	**0.3947**	0.6571	0.5983	0.7556	1.1620	0.5655
	Road	0.4514	0.6388	**0.4344**	0.6524	0.5879	0.8593	0.5460	0.5201
	Traffic	1.6470	**0.6795**	0.7824	1.1191	1.0212	2.1235	1.5703	1.1876
	Festival	**0.2656**	0.3636	0.3702	0.6231	0.4159	0.5160	0.7604	0.6313
	City	0.9992	0.4355	**0.3906**	0.6948	0.3916	1.1996	0.8427	0.5231
	Building	**0.2592**	0.2892	0.3412	0.4891	0.3904	0.7444	0.2901	0.4580
FADE mean value		0.6738	0.5816	**0.4522**	0.7059	0.5675	1.0331	0.8619	0.6476
e	Gugong	0.4210	0.6115	**0.8995**	0.4738	0.5727	0.4249	0.4186	0.5208
	Road	1.5946	**2.2091**	1.8563	1.1783	1.1941	0.6083	1.6055	1.3358
	Traffic	0.6102	1.4777	**1.9566**	1.7857	1.6927	0.4664	1.4089	1.0192
	Festival	0.2172	**0.5007**	0.2724	0.1104	0.2033	0.1522	0.0887	0.0455
	City	2.1011	2.8050	**3.7393**	2.2515	3.5591	1.5653	2.4471	3.4696
	Building	0.6383	0.7569	0.8233	0.5159	**0.8672**	0.1910	0.2310	0.3393
e mean value		0.9304	1.3935	**1.5912**	1.0526	1.3482	0.5680	1.0333	1.1217
SSIM	Gugong	0.8396	0.8399	0.8572	0.8451	0.9030	0.9069	**0.9474**	0.9270
	Road	0.8593	0.8137	0.8548	0.8339	0.9124	0.8941	0.8923	**0.9538**
	Traffic	0.9097	0.7467	0.8929	0.8658	0.9358	0.8384	**0.9615**	0.9332
	Festival	0.6828	0.8844	0.9158	0.8934	0.9229	0.8909	**0.9829**	0.9724
	City	0.3964	0.3292	0.2796	0.3161	0.2712	**0.3993**	0.3913	0.3713
	Building	0.8357	0.7455	0.8053	0.8305	0.7510	0.8534	0.8543	**0.9192**
SSIM mean value		0.7539	0.7266	0.7676	0.7641	0.7827	0.7972	0.8383	**0.8462**
MSE	Gugong	0.0343	0.0345	0.0200	0.0470	0.0088	0.0080	**0.0041**	0.0072
	Road	0.0084	0.0201	0.0201	0.0197	0.0138	0.0087	0.0106	**0.0052**
	Traffic	0.0096	0.0517	0.0286	0.0097	0.0090	0.0208	**0.0025**	0.0061
	Festival	0.0747	0.0199	0.0242	0.0437	0.0163	0.0156	**0.0025**	0.0036
	City	0.0378	0.0782	0.0654	0.0526	0.0651	0.0479	**0.0309**	0.0340
	Building	0.0140	0.0335	0.0531	0.0471	0.0535	0.0147	0.0159	**0.0083**
MSE mean value		0.0298	0.0397	0.0352	0.0366	0.0278	0.0193	0.0111	**0.0107**

3.3.5 Comparison of Processing Time

Except the high restoration quality, the most significant advantage of the proposed IDGCP is the low computation complexity thus reducing processing time. Eqs. 3.5, 3.10, 3.13 and the quad-tree subdivision method [64] used in IDGCP are all simple operations, and the main calculation cost of IDGCP is the gradient operation to determine the unknown constant θ. Therefore, given an image of size $l \times w$, the theoretical complexity of IDGCP is only $\mathcal{O}(\frac{100 \cdot l \cdot w}{max(w,l)})$. To demonstrate the efficiency of IDGCP, a comparison of the processing

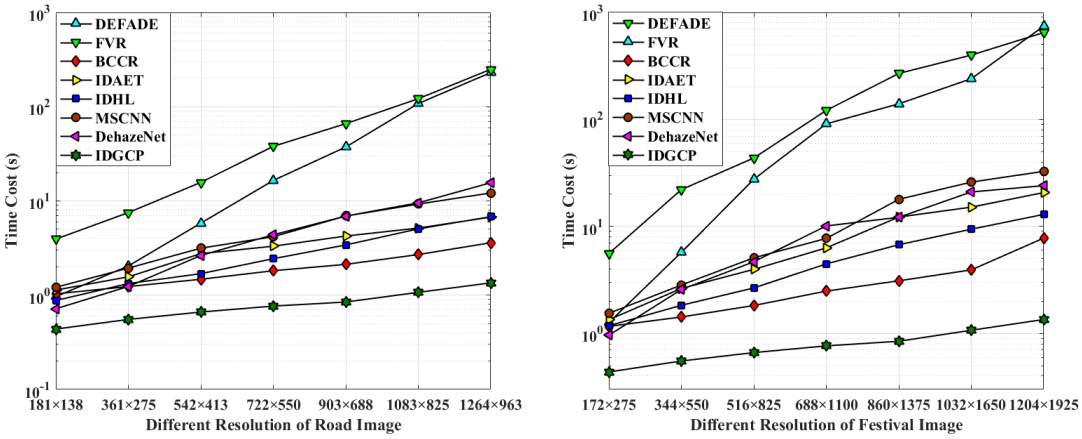

Figure 3.13: Comparison of the processing time of dehazing two example images with tunable resolutions using the proposed IDGCP and other states-of-the-art techniques.

time between different techniques dealing with images with different resolutions is shown in Fig. 4.11. To ensure the fairness of the comparison, two pictures (the “road" and “festival" images shown in Fig. 3.12) with tunable resolutions were used in comparison and all the tests were performed five times to get the average time cost. It can be easily concluded from Fig. 4.11 that IDGCP is significantly faster than all the other techniques regardless of the resolution of the images.

Overall, the comparison results shown in Figs. 3.8 to 4.11 and Table 3.1 demonstrate that the proposed IDGCP outperforms most of the state-of-the-art methods in terms of haze removal, color restoration, and processing time while avoiding almost all of the negative effects.

3.4 Conclusion

In this chapter, a very simple yet powerful gamma correction prior (GCP) was proposed, leading to an extremely efficient single image dehazing method called IDGCP. The proposed GCP allows us to approximately simulate a homogeneous misty image from an

input hazy image. Based on this prior and ASM, IDGCP was developed to overcome the low real time performance and low robustness ability of available techniques. Different from previous works, IDGCP converts single image dehazing into multiple images haze removal task. The benefit is to ease the uncertainty of depth information, so that the haze removal task can be redefined as a global-wise optimization function to determine only one unknown constant. IDGCP can obtain a high-quality transmission map without any refining process, which significantly reduces the processing time. A series of experimental results demonstrate that IDGCP achieves noticeably higher efficiency and outstanding dehazing ability compared to the state-of-the-art techniques.

Chapter 4

VROHI: Visibility Recovery for Outdoor Hazy Image Based on Modified Additive Haze Model

This chapter also aims to provide a highly efficient image dehazing method for hazy outdoor images. Unlike the IDGCP proposed in chapter 3, the technique proposed in this chapter is based on an additive haze model (AHM) which has a potential to increase the efficiency of the dehazing procedure. In this chapter, according to the low-frequency feature (LFC) of haze, AHM is modified via gamma correction technique to make it suitable for modeling outdoor images. Based on this modified AHM (MAHM), a simple yet effective method called VROHI is proposed to enhance the visibility of an outdoor hazy image. In specific, a low complexity LFC extraction method is designed by utilizing characteristic of the discrete cosine transform. Subsequently, by constructing the linear function of unknown parameters and imposing the saturation prior on MAHM, the image dehazing problem can be derived into a global optimization function. To overcome the problem of visual darkness and color cast, the dehazed result is later enhanced by correcting its

atmospheric light.

4.1 Modified Additive Haze Model

Additive haze model (AHM) proposed in [2] is used to describe remote sensing (RS) images in machine vision and computer graphics. This model is expressed as

$$\boldsymbol{DN}^i_{observed}(x,y) = \boldsymbol{DN}^i(x,y) + \boldsymbol{HR}^i(x,y), \tag{4.1}$$

where (x, y) is image coordinate, i is band index, $\boldsymbol{DN}_{observed}$ is multi-spectral RS data captured by satellite, $\boldsymbol{DN}$ is expected surface radiance, and $\boldsymbol{HR}$ is haze contribution. Unlike the RS data containing both visible bands and additional infrared bands, only three visible RGB bands are included in outdoor images, which means AHM can be further optimized to reduce its complexity.

According to Rayleigh's law [19], the interference of haze depends on the wavelength of light. Since the wavelength variation between the RGB bands for outdoor images is much smaller than that in the multi-bands for RS images, here we assume that the haze contribution to the RGB bands of outdoor images is similar. Consequently, when using AHM to represent RGB bands outdoor hazy images, we propose to use a haze thickness map (HTM) $\boldsymbol{H}$ to replace HR^i in Eq. 4.1. This then leads to:

$$\boldsymbol{I}^c(x,y) = \boldsymbol{J}^c(x,y) + H(x,y), \tag{4.2}$$

where $c \in \{r, g, b\}$ is color channel index, $\boldsymbol{I}$ is outdoor image contaminated by haze, and $\boldsymbol{J}$ is haze-free scene albedo. In [88], Li et al. verified that haze is highly related to the illumination component and is concentrated in the low-frequency band of an input image. There exists a quasi-linear relationship between the HTM and the low-frequency component (LFC) of the input image. Here, by considering the quasi-linear relationship

and based on an observation of the haze distribution characteristic of numerous hazy images, gamma correction (GC) is used to relate the HTM with the LFC, i.e.,

$$H(x,y) = \sigma \cdot (L_f(x,y))^{\gamma}, \tag{4.3}$$

where L_f is the LFC of the input image, $\gamma \in [0,1]$ is the GC parameter to adjust the haze distribution, and $\sigma \in [0,1]$ is a constant related to the haze density. By accurately extracting the LFC and properly setting the values of σ and γ, one is able to get accurate HTM from the LFC of hazy image, which is the premise of subsequent high-quality haze removal.

Combining Eq. 4.2 and Eq. 4.3, a modified AHM (MAHM) for outdoor image dehazing can be obtained as

$$\boldsymbol{J}^c(x,y) = \boldsymbol{I}^c(x,y) - \sigma \cdot (L_f(x,y))^{\gamma}. \tag{4.4}$$

According to MAHM, the key of image dehazing is to mine LFC and estimate the two constants σ and γ from the input hazy image $\boldsymbol{I}$, which will be presented in the next section.

4.2 Proposed VROHI

In this section, based on the MAHM described in the previous section, a fast visibility recovery method called VROHI is developed for outdoor hazy images. The proposed VROHI consists of two major modules, i.e., global-optimization-based dehazing module and atmospheric light correction (ALC) module.

4.2.1 Global-Optimization-Based Dehazing

1) **Extraction of LFC**: According to Rayleigh's law [19], the blue channel of a hazy outdoor image I^b is more susceptible to the interference of haze compared to the red and

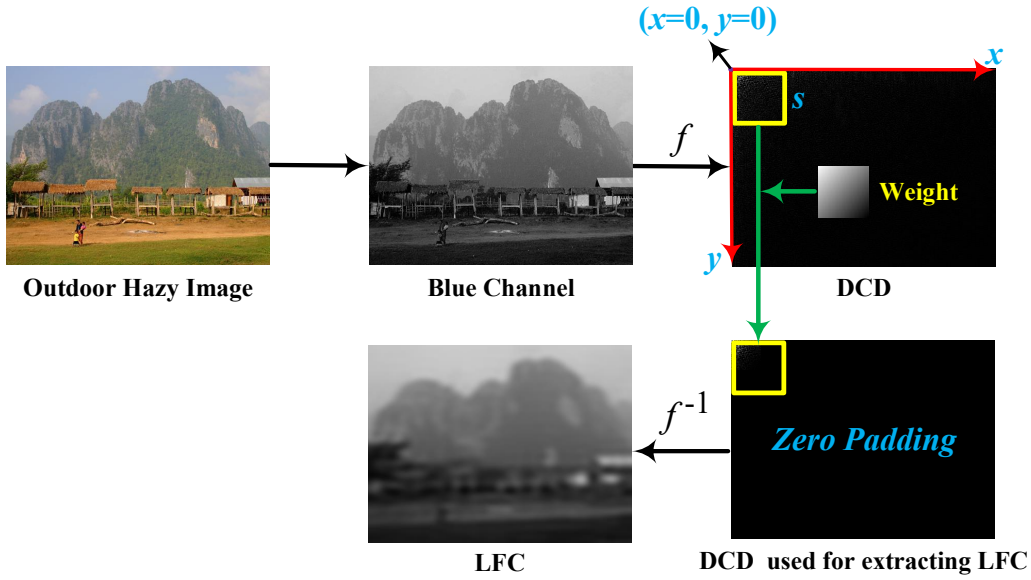

Figure 4.1: The working mechanism of Eq. 4.5.

green channels. Therefore, here we attempt to excavate the LFC from I^b. Directly employing image blur tools with edge protection, e.g., guided filter (GF) [29], joint bilateral filter(JBF) [50], and guided total variation (GTV) [71], is the most intuitive way to calculate the LFC. However, these techniques all need complex convolution operators to get the filter weights for each pixel in whole image, which would reduce the computational efficiency of haze removal. To this end, a low complexity discrete cosine transform based LFC extraction method is proposed. Specifically, this procedure can be expressed by

$$\begin{cases} F' = f\left(I^b\right) \\ F_L\left(x,y\right) = \begin{cases} W\left(x,y\right) \cdot F'\left(x,y\right), 0 \le x \le s, 0 \le y \le s \\ 0, else \end{cases} \\ L_f = f^{-1}\left(F_L\right) \end{cases} \tag{4.5}$$

where $f\left(\cdot\right)$ and $f^{-1}\left(\cdot\right)$ are the discrete cosine transform (DCT) operator and inverse DCT (IDCT) operator, F' is the discrete cosine domain (DCD) of I^b obtained via DCT, F_L is the weighted F, s is the size of a square patch selected on F' for weighting, and W is the introduced weighting factor.

For clarity, the working mechanism of Eq. 4.5 is illustrated in Fig. 4.1. The first step is to obtain the blue channel from input image. Then DCD of I^b is obtained using DCT. In subsequence, a square patch with the size of s at the upper left corner in the DCD is selected. This is due to the fact that the LFC data are mainly concentrated at the upper left corner in F'. Since the data should be more reliable for extracting LFC if it is more closer to the upper left corner [89], to improve the reliability, a weighting function is defined as

$$W(x, y) = 1 - \frac{x + y}{2 \cdot s} \tag{4.6}$$

Finally, the LFC is extracted from the weighted F through IDCT.

To demonstrate the superiority of the proposed LFC extracting method, Fig. 4.2 illustrates the LFCs extracted by GF, JBF, GTV, and the proposed method. As observed in the figure, the obtained results are similar but the proposed method consumes much less time.

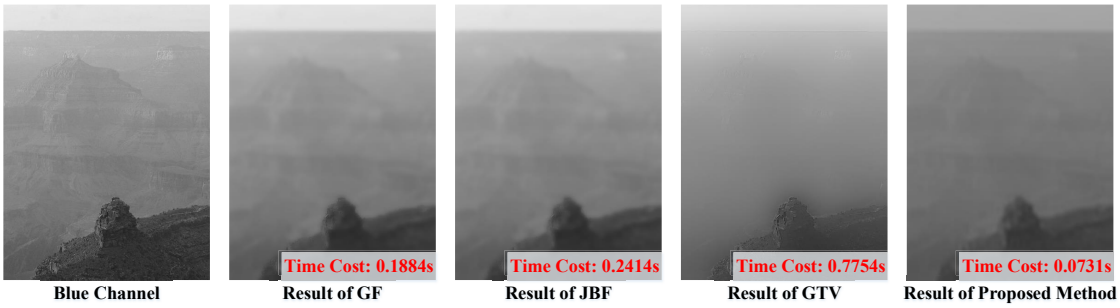

Figure 4.2: Comparison of LFC extraction effect between different operators.

2) **Estimation of σ and γ**: In general, mist images usually have sharper haze distribution than images with heavy haze, as shown in Fig. 4.3(a). In other words, images with high haze density (large σ value) tends to have fatter haze distribution; images with low haze density (small σ value) tends to have sharper haze distribution. Meanwhile, recall the characteristic of GC as shown in Fig. 4.3(b), i.e., given the input (L in Eq. 4.3), the smaller the γ, the fatter the output (H). This leads to a conclusion that there exists

an inverse proportional relationship between σ and γ (the larger the σ, the smaller the γ), when using Eq. 4.3 to model the HTM of a hazy image. There is no doubt that the HTM estimation can be significantly simplified if the relationship between σ and γ can be fitted with a linear equation. Considering that $\gamma \in [0,1]$ and $\sigma \in [0,1]$, a following linear function is proposed as

$$\gamma = 1 - \kappa \cdot \sigma \tag{4.7}$$

where κ is a parameter introduced to adjust this linear expression to achieve higher accuracy. Substituting Eq. 4.5 and Eq. 4.7 into Eq. 4.4, the recovery formula can be expressed as

$$\boldsymbol{J}^c = \boldsymbol{I}^c - \sigma \cdot \left(f^{-1}\left(F_L\right)\right)^{1-\kappa\cdot\sigma} \tag{4.8}$$

To avoid pixel overflow, the scene radiance J_c is constrained at the interval $[0,1]$. Therefore, the expression used for restoring the scene radiance can be rewritten as

$$\begin{aligned} \boldsymbol{J}^c &= VR\left(\kappa, \sigma, \boldsymbol{I}, f^{-1}\left(F_L\right)\right) \\ &= min\left(max\left(\boldsymbol{I}^c - \sigma \cdot \left(f^{-1}\left(F_L\right)\right)^{1-\kappa\cdot\sigma}, 0\right), 1\right) \end{aligned} \tag{4.9}$$

where $VR\left(\cdot\right)$ is the abbreviation of scene radiance restoring function. Note that $VR\left(\cdot\right)$ is a function of four parameters, where $\boldsymbol{I}$ is the input, F_L can be calculated via Eq. 4.5, κ is the empirical parameter, and σ is the only unknown constant related to haze density. To estimate the value of σ accurately, a saturation prior [90] based global optimization function (GOF) is designed as

$$\sigma = \omega \cdot argmin\left\{\theta - \phi\left(VR\left(\kappa, \sigma, I, f^{-1}\left(F_L\right)\right)\right)\right\} \tag{4.10}$$

where $\phi\left(\cdot\right)$ is saturation operator, θ is average saturation of high-quality image, and ω is introduced to adaptively keep a small amount of haze for distant scenes to make the dehazed results appear to be more natural. In contrast to currently used pixel-wise, patch-wise, scene-wise, and non-local-wise strategies, the designed GOF is capable of making up

the limitation of saturation prior. This is due to the fact that the information of the whole image is richer than that of a patch or scene, thus global optimum results instead of local ones can be obtained. Considering that Eq. 4.10 is also a one-dimensional optimization function, Fibonacci method (FM) is adopted to solve Eq. 4.10 since it is able to gradually narrow the search interval for one-dimensional optimization problem until convergence condition is satisfied. In specific, the initial interval and the final interval length are defined as [0, 1] and 0.05, respectively. Once θ is determined via the GOF with golden section method (GFM), the scene radiance can be directly recovered by Eq. 4.9. Taking the hazy images in Fig. 4.3(a) as examples, the HTMs and recovery results using the proposed method are shown in Figs. 4.3(c) and 4.3(d), respectively. It can be observed from these results that the estimated HTMs are in line with intuition, and the haze cover in hazy images can be thoroughly removed. Regrettably, the result restored via MAHM is too dark and has a lower contrast than original hazy image. This is since MAHM can only exclude the haze contribution from hazy input, while it lacks the ability to highlight the textures and profiles blurred by haze, thus dehazed result using MAHM needs to be further improved.

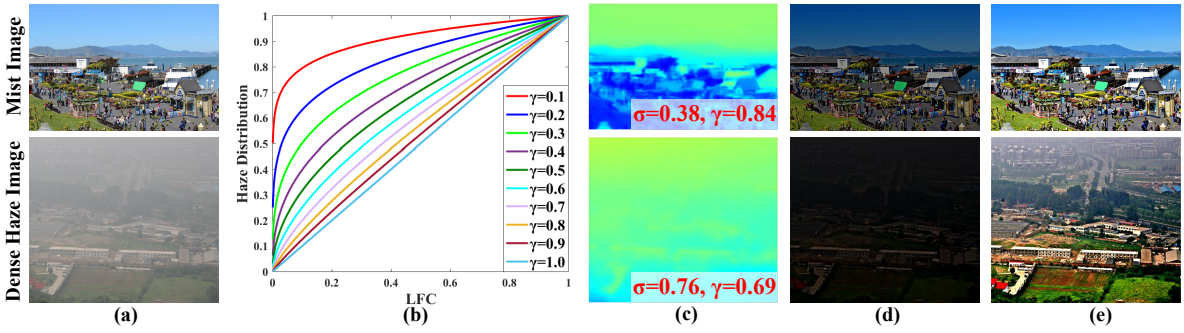

Figure 4.3: **(a):** Outdoor hazy images. **(b):** Curves of haze distribution with different values of γ. **(c):** HTMs ($\sigma \cdot \mathrm{L}^{\gamma}$). **(d):** Recovery Results. **(e):** Results enhanced by ALC.

4.2.2 Atmospheric Light Correction (ALC)

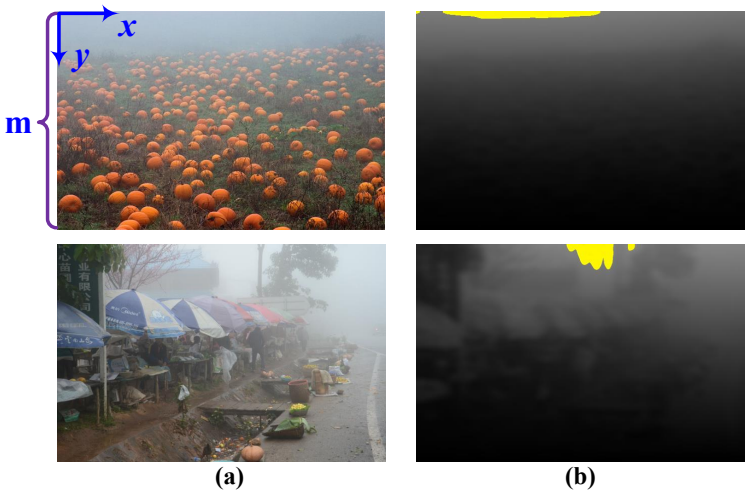

Figure 4.4: Two examples of the weighting map used for locating atmospheric light. **(a):** Hazy images. **(b):** Weighting maps obtained via Eq. (11).

To address the visual darkness problem and the interference of color cast caused by ambient light, an effective ALC technology is developed. In specific, since the atmospheric light is usually located in the sky region or dense haze regions, a weighting map for locating atmospheric light is defined as

$$W'(x,y) = \left(1 - \frac{y}{m}\right) \cdot H(x,y) \tag{4.11}$$

where m is the image height. Figs. 4.4(a) and 4.4(b) illustrate two examples of hazy images and their weighting maps to locate the atmospheric light. With the defined weighting function, the pixels with smaller y value (more close to the sky region) and large haze thickness are assigned to have larger weighting factors. The pixels having the top 0.1% weighting factors are highlighted in yellow in Fig. 4.4(b). Then, from the highlighted area, the pixel with the highest intensity in the hazy input is selected. This intensity of selected pixel is defined as the intensity of the atmospheric light A^c, thus the obtained

Table 4.1: Dehazing procedure of VROHI.

Input	Hazy Image I
Initial parameters	$\omega = 0.95$, $s = 100$, $\kappa = 0.4$, $\theta = 0.103$
Dehazing procedure	1: Calculate the weight W via Eq. 4.6; 2: Extract the LFC via Eq. 4.5 using the W; 3: Determine the constant σ via Eq. 4.10 with GFM; 4: Restore the scene radiance J via Eq. 4.09; 5: Compute the wight map W′ via Eq. 4.11; 6: Locate the atmospheric light of J based on W′; 7: Enhance the scene radiance as J_e via Eq. 4.12.
Output	Recovery result J_e

scene radiance can be transformed to

$$\boldsymbol{J_e^c}(x,y) = \frac{\boldsymbol{J}^c(x,y)}{\boldsymbol{A}^c} \tag{4.12}$$

where J_e^c is the final high-quality recovery result. By comparing the results with and without ALC as respectively shown in Figs. 4.3(d) and 4.3(e), it can be observed that the proposed ALC module effectively improves the overall contrast and truly restitute the original color.

For clarity, the step-by-step procedure of VROHI is outlined in Table 4.1. Note that the values of the pre-set parameters given in Table 4.1 are optimized results considering different scenarios. One does not need to re-estimate these parameters when using the VROHI for image dehazing. Also, it is noted that, in this dehazing procedure, steps 1, 2, 4∼7 are all simple operations and step 3 can be directly solved via GFM with low computational overhead, which guarantees a high efficiency of VROHI.

4.3 Experiments

To evaluate VROHI, each module of VROHI is further assessed by experiments. Then, qualitative and quantitative comparisons are made between the proposed VROHI and

other state-of-the-art technologies to demonstrate its superiority. In specific, we tested VROHI on various challenging hazy images and compared the results with those obtained from some well-known algorithms including HR [2], DCP [4], MSF [33], DehazeNet [84], BCCR [51], NLD [75], CAP [56], DEFADE [34], MSCNN [69], and AoD-Net [70]. Among these methods, HR is used for proving the accuracy of HTM model, DCP, MSF, and DehazeNet are included in the comparison to validate the performance of the proposed global-optimization-based strategy, and the rest algorithms are tested for qualitative and quantitative comparisons of the image dehazing capability.

In this work, experiments[1] were conducted by MATLAB2016b on a PC with Intel(R) Core (Tm) i7-8700 CPU@ 3.20 GHz 16.00 GB RAM. Note that the codes of DehazeNet, BCCR, NLD[2], CAP, DEFADE, and MSCNN are downloaded from the authors' websites. The codes of HR, MSF and DCP are not publicly available, but they are easy to implement.

4.3.1 Initial Parameter Setup

There are four parameters that need to be initialized in the proposed VROHI, i.e., ω, θ, s, and κ. In this work, the value of ω is set to be 0.95 as suggested in [23]; the value of θ is selected to be 0.103 according to saturation prior [48]. Only s and κ are new parameters introduced in this work. To find appropriate values for them, the performance test of VROHI on two examples with different combinations of s and κ was conducted, as illustrated in Fig. 4.5. It can be concluded from this figure that smaller value of s can produce more realistic colors, and the smaller value of κ is able to lead to stronger haze removal ability. However, too small value of s may introduce halo artifact and black effect

[1]The MATLAB code of VROHI is available on the authors' website: `https://www.researchgate.net/profile/Mingye_Ju`

[2]Due to the unspecific gamma factor and atmospheric light in NLD, we estimated the atmospheric light via [4] and initialized the value of gamma factor to be 1 for NLD

in the depth jumps (see the zoom-in red patches), and too small value of κ also introduce over-saturation problem in close-range scene (see the blue patches). As a tradeoff, we chose $s = 100$ and $\kappa = 0.4$ in this work since they can achieve the best visual quality. Once the parameters in VROHI are determined, it can be used on all types of images straightforwardly. In following experiments, the recovered results of VROHI are all based on the combination of the determined parameters, as listed in the Tab. 4.1.

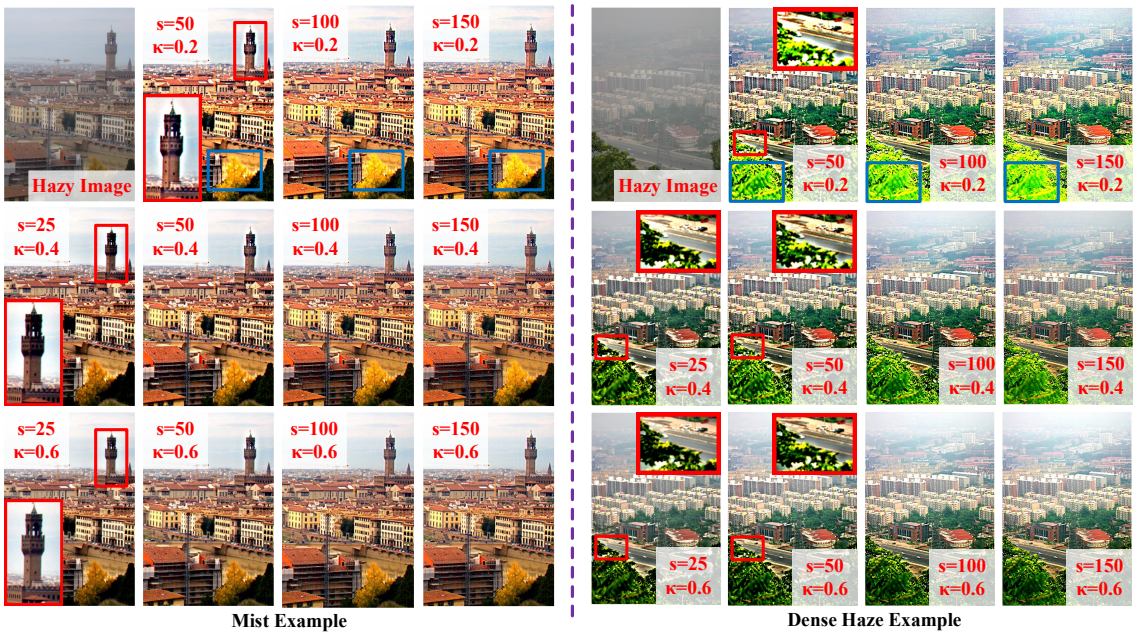

Figure 4.5: Image dehazing using VROHI with different combinations of s and κ while ω is fixed at 0.95 and θ is fixed at 0.103.

4.3.2 VROHI Performance Demonstration

4.3.2.1 Evaluation of HTM

An accurate HTM is the premise of the final high-quality dehazing. In HR [2], the HTM is estimated by employing the widely-used dark channel prior (DCP). Fig. 4.6 shows the comparison between the HTM excavated via VROHI and that obtained via HR on two

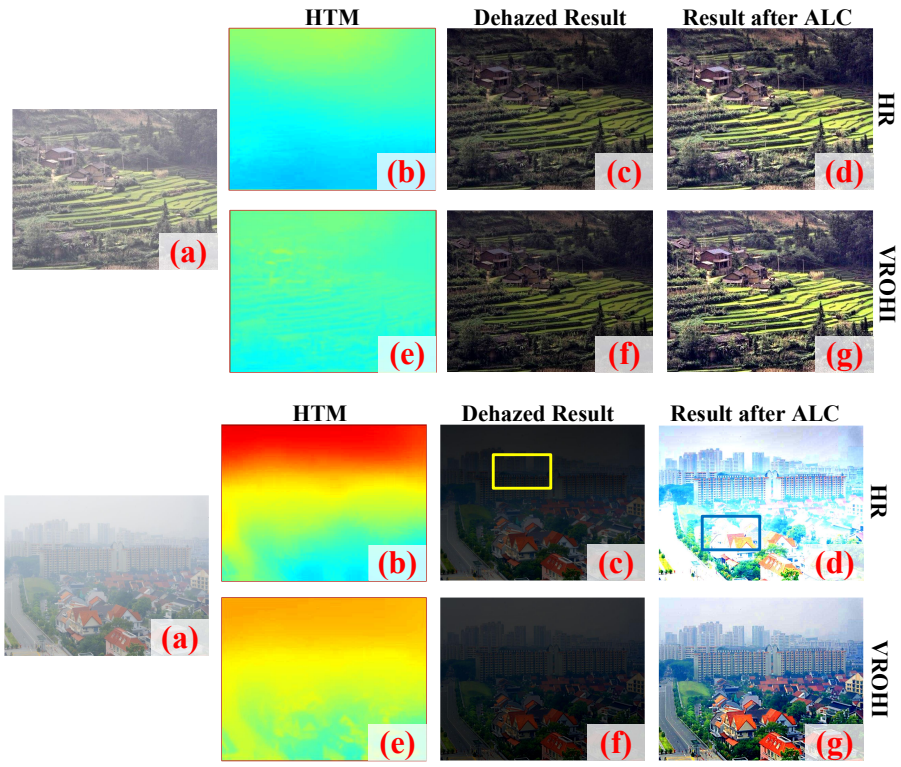

Figure 4.6: Comparison of the HTM obtained by [2] and by the proposed VROHI. **(a):** Hazy images. **(b):** HTM estimated via [3]. **(c):** Dehazed Results via MAHM using (b). **(d):** Enhanced results via ALC based on (c). **(e):** HTM estimated via the proposed VROHI. **(f):** Dehazed Results via MAHM using (e). **(g):** Enhanced results via ALC based on (f).

example hazy iamges. As can be seen from this figure, both HR and VROHI can excavate an accurate HTM and achieve a realistic recovery result for the first example. However, due to the limitation of DCP, HR is not able to deal with the bright and smooth regions for the second example, as shown in the yellow patch in Fig. 4.6(c). Moreover, this error restoration leads to information loss in the result enhanced by the ALC, as shown in the blue patch in Fig. 4.6(d). In contrast, VROHI's HTM can effectively address this issue and accurately reflect the haze distribution, thereby exhibiting a better visual quality.

4.3.2.2 Evaluation of Global-Optimization-Based Dehazing

As aforementioned, there are mainly three categories of image algorithms that are proposed to enhance the visibility of images captured in hazy weather. They are the ASM-based, multi-scale-fusion-based, and deep-learning-based methods. Fig. 4.7 illustrates the processing procedure and the associated running time of the proposed VROHI (global-optimization-based) and three representative techniques, including DCP (ASM-based) [4], MSF (multi-scale-fusion-based) [**?**], and DehazeNet (deep-learning-based) [84]. As illustrated in Fig. 4.7, the proposed VROHI only needs to determine one unknown constant while the other methods need to employ complex tools (such as guided filter and Laplacian-pyramid operator) to realize the haze removal. As a consequence, the proposed global-optimization-based VROHI takes a much shorter time to recover the hazy input.

4.3.2.3 Evaluation of VROHI on different sample images

After evaluating the embedded HTM modeling module and global-optimization strategy, the proposed VROHI was then tested on various types of outdoor hazy images obtained from well-known references [71,84]. Fig. 4.8 shows the original hazy images, the calculated HTMs, and the corresponding dehazed results to intuitively demonstrate the robustness of VROHI. It can be observed from this figure that VROHI can accurately estimate the HTM and thoroughly remove the haze from the input image, no matter whether the atmospheric particle distribution is homogeneous or inhomogeneous. Moreover, without introducing any additional post-processing as suggested in [91, 92], VROHI still successfully avoids the over-enhancement in the sky regions and the over-saturated in the mist regions.

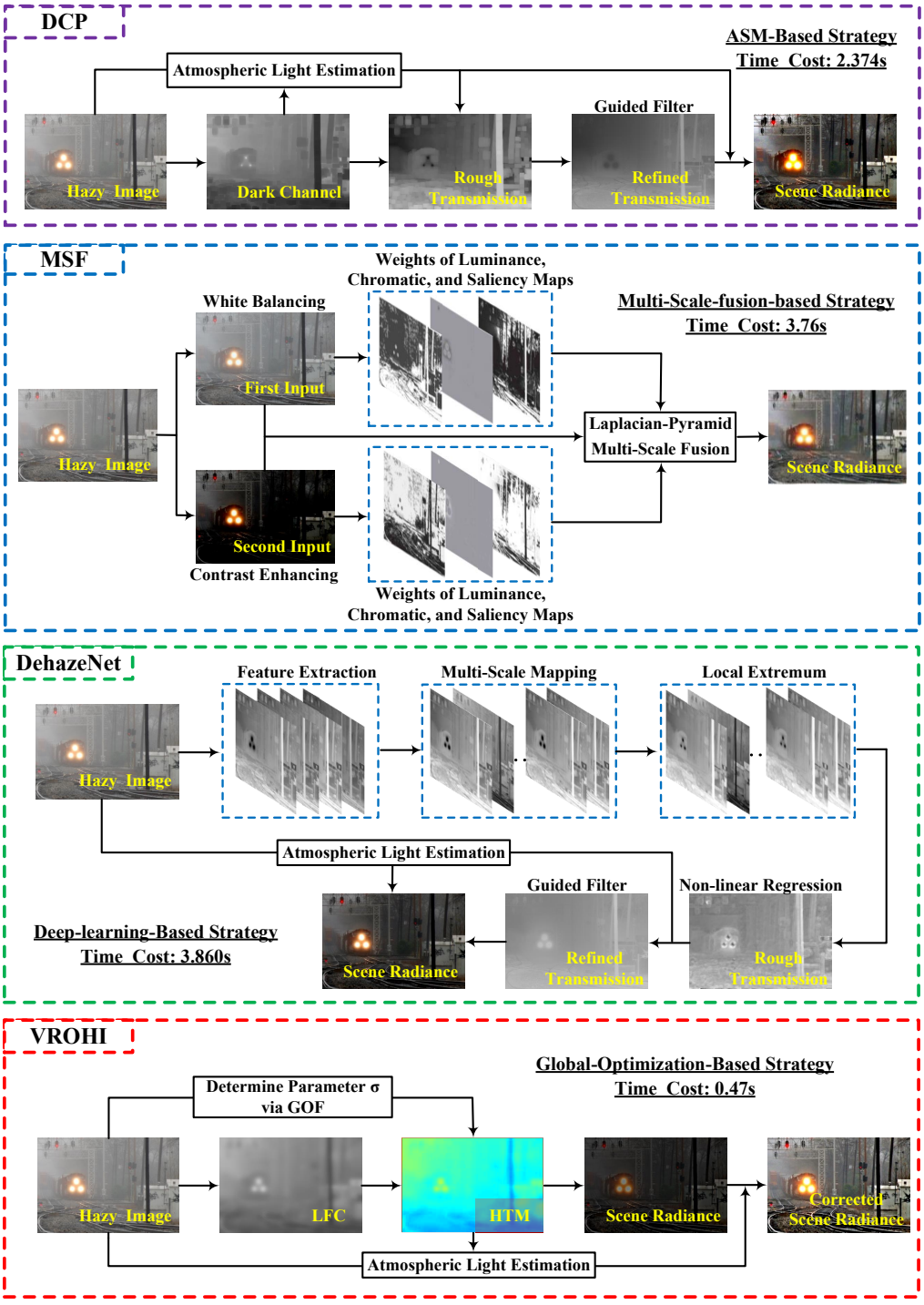

Figure 4.7: Overview of image dehazing procedures using DCP, MSF, DehazeNet, and the proposed VROHI.

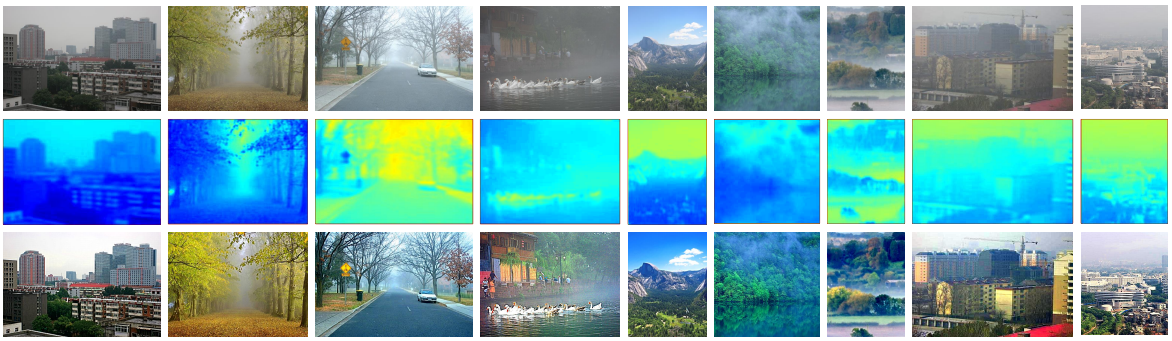

Figure 4.8: Visibility recovery result of VROHI on different types of outdoor hazy images. **Top:** Hazy images. **Middle:** Calculated HTMs. **Bottom:** Results recovered via VROHI.

4.3.3 Qualitative Comparisons with State-of-the-art Technologies

4.3.3.1 Comparison on challenging real-world images

Being able to handle hazy images with complex environment, for example, mist, heavy haze, non-uniform haze, and white-gray scene, is a significant but challenging task for dehazing techniques. Fig. 4.9 compares the processing results of BCCR (ASM-based) [51], NLD (ASM-based) [75], CAP (ASM-based) [56], DEFADE (multi-scale-fusion-based) [34], MSCNN (deep-learning-based) [69], AoD-Net (deep-learning-based) [70], and the proposed VROHI (global-optimization-based) on six challenging outdoor images.

As shown in Figs. 4.9(b) and 4.9(c), both BCCR and NLD can uncover the texture details for all the given images. However, they cannot well handle the regions where the brightness of scene targets is inherently similar to the atmospheric light. In particular, the colors in the recovered rocky areas are completely deviated from the real situation that expected (see the fifth example). For CAP as shown in Fig. 4.9(d), although it can avoid the above negative problems, its dehazing strength is very weak. This is due to the fact that scattering coefficient used in CAP is simply set as a fixed constant. In Fig. 4.9(e), DEFADE is able to thoroughly exclude the haze for most given images, but its

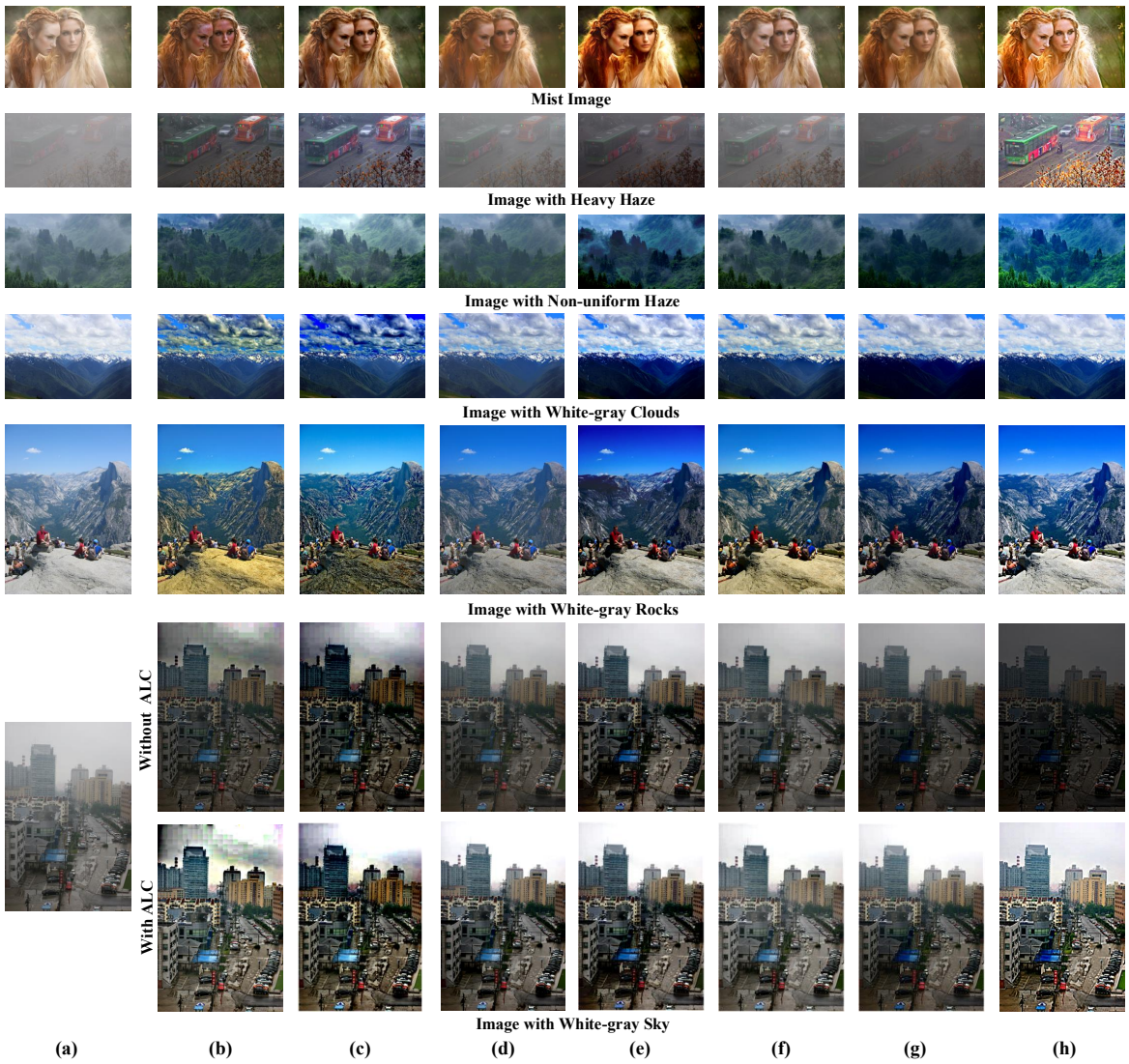

Figure 4.9: Qualitative comparison between some state-of-the-art techniques and the proposed VROHI on different kinds of challenging hazy images. **(a):** Hazy images. **(b):** BCCR. **(c):** NLD. **(d):** CAP. **(e):** DEFADE. **(f):** MSCNN. **(g):** AoD-Net. **(h):** VROHI.

recovery scenes appear to be darker than they should be. Besides, in the dark regions, the dehazed results using DEFADE suffers from information loss (see the fourth example). As seen in Fig. 4.9(f) and 4.9(g), the results obtained via MSCNN and AoD-Net are very visual compelling for mist scenes, whereas they lack the ability to restore to hidden textures for the scenes with heavy haze (see the second example). Moreover, all these comparable methods are not suitable to deal with the image with non-uniform haze (see the third example). The scenes with thick haze in the original picture are still surrounded by some mist in the dehazed results. In comparison, VROHI is able to achieve more realistic haze-free results without these negative visual effects, as shown in Fig. 4.9(h). Here we remark that, even the atmospheric light of results dehazed by these compared methods is also revised to be one using the proposed ALC module, the results produced by VROHI still hold the best visual quality (see the last example).

4.3.3.2 Comparisons on synthetic images

Despite the fact that the proposed VROHI is capable of achieving the best recovery results on real-world images, the comparison shown in Fig. 4.9 might be unfair since it is hard to capture haze-free scenes as the corresponding references of the real-world hazy images. Therefore, we further conducted a comparison between VROHI and state-of-the-art techniques on some sample images from the Realistic Single Image Dehazing (RESIDE) dataset [85], which includes both the hazy images and the corresponding haze-free images. Figs. 4.10(a)∼11(h) show the hazy images and the recovered results based on the synthesized images using BCCR, NLD, CAP, DEFADE, MSCNN, AoD-Net, and the proposed VROHI, respectively. The corresponding ground truth references are given in Fig. 4.10(i) to facilitate this comparison.

As observed in Figs. 4.10(b) and 4.10(c), the restored results using BCCR and NLD can clearly indicate the target contour for all the given examples, but the restored colors

are generally over-saturated (see the first and fourth examples). In addition, there is also an over-enhancement problem in the sky region (see the third example). As shown in Fig. 4.10(d), the haze still remains in the second and last examples after the dehazing process of CAP. According to Fig. 14.10(e), DEFADE achieves a visually pleasing result for most examples, but cannot deal with the fourth example well. As seen in Figs. 4.10(f) and 4.10(g), MSCNN and AoD-Net are capable of attaining the haze-free results with vivid color and necessary details for mist scenes. However, haze residue can be found in the second and last examples. Compared to these methods, VROHI is able to moderately uncover the contents and contours from vague scenes. More importantly, VROHI's results do not lead into any negative effects and can maintain the tones of ground truth images, as demonstrated in Fig. 4.10(h).

4.3.4 Quantitative Comparisons with State-of-the-art Technologies

Qualitative comparison depends on individual's subjective judgment, which may cause differences in judgment among different viewers. Therefore, widely-recognized metrics including the fog aware density evaluator (FADE) [34], the mean ratio of the gradients at visible edge (r) [86], the ratio of new visible edges (e) [86], and the mean square error (MSE) are used to quantitatively evaluate the proposed VROHI and aforementioned techniques. In general, a smaller FADE indicates a stronger restoration ability, larger r and e stand for a richer information contained in the recovery results, and a smaller MSE means that the dehazed result is closer to the corresponding real scene. The values of the assessment metrics on the dehazed results shown in Fig. 4.10 are summarized in Table 4.2. It can be concluded from the figure that VROHI achieves the best scores of FADE, r, and e for the examples E2, E3, and E5. This indicates that VROHI has the ability to restore richer information and remove more haze from single input image. Despite the

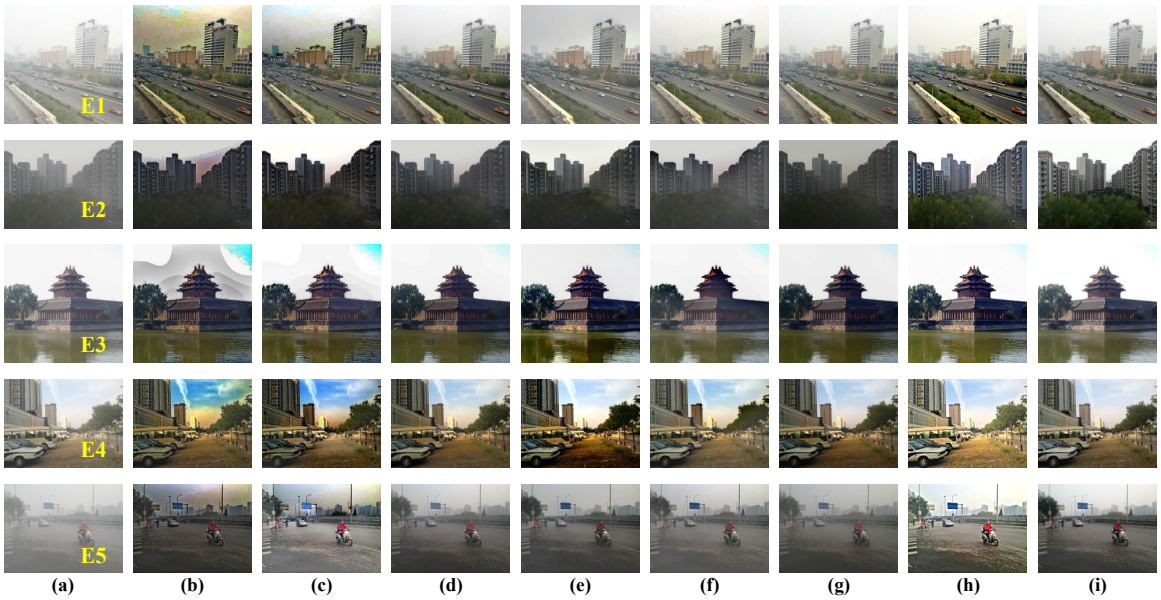

Figure 4.10: Qualitative comparison between the proposed VROHI and other state-of-the-art techniques on synthetic images. **(a):** Hazy Images. **(b):** BCCR. **(c):** NLD. **(d):** CAP. **(e):** DEFADE. **(f):** MSCNN. **(g):** AoD-Net. **(h):** VROHI. **(i):** Ground Truth Images.

fact that BCCR and NLD have the better scores of FADE, r, and e than VROHI for the remaining examples, the images dehazed via these methods appear to be over-enhanced. This might leads to some unreasonable edges, e.g., in the sky regions of the first example. For MSE, the score of VROHI is not the best compared with other techniques. In VROHI, the atmospheric light is corrected to be 1, which makes the average brightness of the final restored scene radiance might be larger than that of the corresponding ground truth. This makes the dehazed results obtained by VROHI exhibits a clearer scene than the ground truth image, thus leading to a larger MSE value. Although there is a discrepancy between the ground truth and the dehazed result obtained by VROHI, the resultant clearer scene is not a drawback.

Table 4.2: Quantitative Comparison of Recovery Images Shown in Fig. 4.10 using $\bar{r}$, e, FADE, and MSE.

Metrics	Examples	BCCR	NLD	CAP	DEFADE	MSCNN	AoD-Net	VROHI
$\bar{r}$	E1	**3.7767**	2.3792	1.8308	1.5697	1.5930	1.5257	2.3403
	E2	1.9603	2.0151	1.6435	1.8490	1.3445	1.2234	**3.7464**
	E3	1.7352	1.5047	1.4140	1.8790	0.9982	1.2079	**1.9099**
	E4	1.6842	1.5410	1.4206	1.6492	1.0953	1.2081	**2.2405**
	E5	2.5712	3.5672	1.6997	1.6405	1.5819	1.4241	**4.2017**
$\bar{r}$ mean value		2.3455	2.2015	1.6017	1.7175	1.3226	1.3178	**2.8878**
e	E1	**0.9554**	0.4320	0.3840	0.3511	0.3576	0.3350	0.3978
	E2	1.5276	1.8290	1.4496	1.0190	0.6038	1.4896	**1.8479**
	E3	0.6079	0.4665	0.4532	0.5688	0.1534	0.5342	**0.6258**
	E4	**0.2185**	0.1471	0.1209	0.0721	0.0697	0.0994	0.1327
	E5	3.5516	3.6450	3.1755	2.7531	2.2544	3.0072	**3.8867**
e mean value		1.3722	1.3039	1.1166	0.9528	0.6878	1.0931	**1.3782**
FADE	E1	**0.3683**	0.5816	0.9374	1.2254	1.1191	1.1733	0.5083
	E2	0.6667	0.7886	1.4090	1.1286	1.2724	1.0986	**0.4124**
	E3	0.5877	0.5972	0.6752	0.6278	0.8071	1.0885	**0.4947**
	E4	0.2732	**0.2562**	0.3568	0.2580	0.5099	0.4158	0.2830
	E5	0.5695	0.6592	1.3986	1.3055	1.5745	1.6388	**0.5184**
FADE mean value		0.4931	0.5766	0.9554	0.9091	1.0566	1.0830	**0.4434**
MSE	E1	0.0422	0.0314	0.0041	0.0116	0.0041	**0.0017**	0.0060
	E2	0.0480	0.0449	**0.0310**	0.0316	0.0389	0.0436	0.0359
	E3	0.0296	0.0157	**0.0111**	0.0133	0.0065	0.0140	0.0138
	E4	0.0211	0.0277	0.0064	0.0141	**0.0044**	0.0062	0.0151
	E5	0.0414	0.0340	**0.0051**	0.0103	0.0090	0.0109	0.0068
MSE mean value		0.0365	0.0307	**0.0116**	0.0162	0.0126	0.0153	0.0155

4.3.5 Efficiency Comparisons

Apart from the restoration quality, the computational complexity is another critical metric for image dehazing technique. Taking the first two hazy images in Fig. 4.10 as test examples, we further give a comparison of the running time between aforementioned methods and VROHI with different resolutions, as shown in Fig. 4.11. Please note that AoD-Net is implemented in Pycaffe and the remaining techniques are carried out in Matlab, thus we did not show the running time of AoD-Net for fairness. Due to the employed global-optimization-based strategy, it is not surprising that the proposed VROHI exhibits significantly shorter processing times compared to other techniques. It is more appealing that the time cost curve of VROHI has the smallest slope among

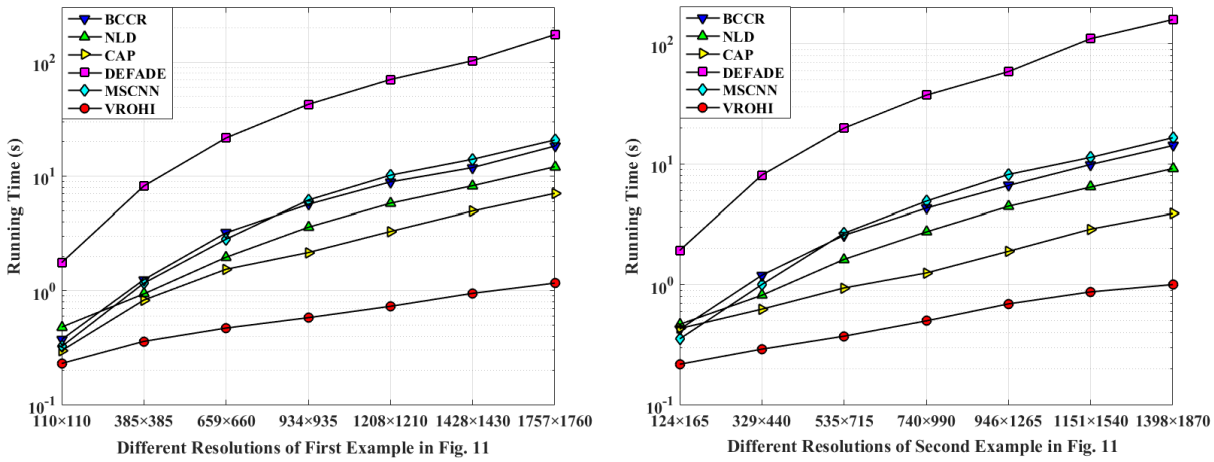

Figure 4.11: Comparison of the running time of the states-of-the-art techniques and the proposed VROHI.

those of different algorithms. This illustrates that, as the image resolution increases, the superiority of the proposed VROHI over other techniques, i.e., faster processing, becomes more significant.

4.4 Conclusion

In this chapter, a modified additive haze model (MAHM) is introduced for fast hazy image restoration. Based on this MAHM, a visibility recovery technique for single hazy images called VROHI is further developed. By combining the low-frequency component of hazy image and the saturation prior, VROHI only needs to determine one unknown constant to achieve visibility recovery, and can work well on both mist, heavy haze, inhomogeneous haze, and gray white scene images. In addition, all the operators used in VROHI have lower computational complexity than the tools employed in the state-of-the-art approaches, which makes it a superior candidate for real-time systems. Moreover,

an atmospheric light correction (ALC) module is employed to compensate the quality degradation due to using simplified models, which is later proved to be very effective and does not increase the processing time much. Experiments demonstrate that VROHI achieves an outstanding restoration quality and higher efficiency compared to the state-of-the-art techniques.

Chapter 5

IDSL: Image Dehazing with Supervised Learning

To address the issue of uneven illumination, this chapter proposes a scene-based ASM (Sb-ASM) by redefining the atmospheric light as scene incident light. Relying on this Sb-ASM, a fast image dehazing technique named IDSL is later presented by employing a supervised learning strategy. In IDSL, according to visual feature of hazy image, a linear model (LM) between transmission and three known components (luminance, saturation, and gradient) is firstly created. Then the supervised learning is employed to determine the unknown parameters in this model. Combining the transmission estimated by LM with a guided energy model (GEM), the incident light for each scene can be accurately obtained, thereby restoring the high-quality scene albedo via Sb-ASM. Furthermore, a Gaussian-Laplacian pyramid based dehazing framework is designed to accelerate the computational speed.

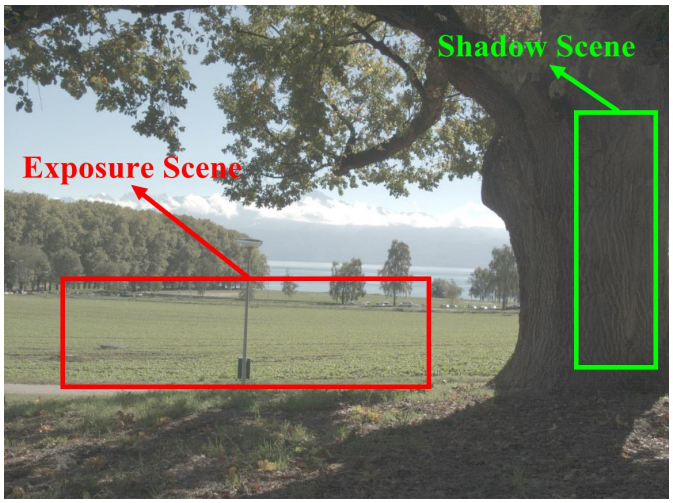

Figure 5.1: An example: hazy image with uneven illumination.

5.1 Scene-based ASM (Sb-ASM)

As mentioned in the Chapter 2, although many ASM-based dehazing studies achieve significantly progress, the restoration effect for images with uneven illumination is not compelling. For instance, the shadow scene in Fig. 5.1 is not directly exposed by the atmospheric light, and it is only covered with the faint indirect radiation from ambient light; This means the fixed atmospheric light assumed in ASM might yield some incorrect results for such cases. To this end, we intend to redefine the atmospheric light as scene incident light which varies between independent scenes. This leads to a novel scene-based ASM (Sb-ASM):

$$\boldsymbol{I}(x,y) = \boldsymbol{L}(i) \cdot \boldsymbol{\rho}(x,y) \cdot t(x,y) + \boldsymbol{L}(i) \cdot (1 - t(x,y)), (x,y) \in \Omega(i) \tag{5.1}$$

where $\Omega(i)$ and $\boldsymbol{L}(i)$ represent the pixel coordinate set and the value of incident light in i^{th} scene, respectively. It should be point out that, although Sb-ASM can better model for the hazy images with uneven illumination, it increases the uncertain of haze removal

because of the fact that global atmospheric light has been redefined by variable incident light.

5.2 Proposed IDSL

5.2.1 Linear Model for Transmission Estimation

Sb-ASM appears to be more complex compared to ASM, thus acquiring the imaging parameters in Sb-ASM is a seriously ill-posed problem. Fortunately, luminance $\bar{I}$, saturation I^{σ}, and gradient $\nabla \boldsymbol{I}$ of input image $\boldsymbol{I}$ are increased or decreased along with the change of the scene depth. This facilitates us to propose:

$$\begin{aligned} Q\left(x,y\right) =& exp\left(-\alpha \cdot \left(\nabla \boldsymbol{I}\left(x,y\right)\right)^{2}\right) \cdot exp\left(-\eta \cdot \left(1-\bar{I}\left(x,y\right)\right)^{2}\right) \\ & \cdot exp\left(-\gamma \cdot \left(I^{\sigma}\left(x,y\right)\right)^{2}\right) \end{aligned} \tag{5.2}$$

where α, η, and γ are unknown coefficients. Relying on the fact that the transmission is inversely proportional to the haze density, a linear model on transmission is constructed as:

$$t\left(x,y\right) = 1-\lambda \cdot Q\left(x,y\right) = 1-\lambda \cdot exp\left(-\alpha \cdot \left(\nabla \boldsymbol{I}\left(x,y\right)\right)^{2} - \eta \cdot \left(1-\bar{I}\left(x,y\right)\right)^{2} - \gamma \cdot \left(I^{\sigma}\left(x,y\right)\right)^{2}\right) \tag{5.3}$$

where λ is also an unknown coefficient. For convenience, Eq. 5.3 is rewritten into

$$G\left(x,y\right) = log\left(\lambda\right) + \alpha \cdot B\left(x,y\right) + \eta \cdot C\left(x,y\right) + \gamma \cdot D\left(x,y\right) \tag{5.4}$$

where $G\left(x,y\right) = log\left(1-t\left(x,y\right)\right)$, $B\left(x,y\right) = -\left(\nabla \boldsymbol{I}\left(x,y\right)\right)^{2}$, $C\left(x,y\right) = \left(1-\bar{I}\left(x,y\right)\right)^{2}$, and $D\left(x,y\right) = \left(I^{\sigma}\left(x,y\right)\right)^{2}$. In order to accurately learn the unknown coefficients, it is necessary to create a training model and collect a large amount of training samples. Referring to [93], the training model corresponding Eq. 5.4 can be described using quadratic

loss function by

$$E = \sum_{i=1}^{n} \sum_{x=1}^{|l_i|} \sum_{y=1}^{|w_i|} \left(G_i\left(x,y\right) - log\left(\lambda\right) - \alpha \cdot B_i\left(x,y\right) - \eta \cdot C_i\left(x,y\right) - \gamma \cdot D_i\left(x,y\right) \right) \tag{5.5}$$

where n is the number of training samples, and $|l_i|$, $|w_i|$, G_i, B_i, C_i, D_i denote height, width and corresponding values of G, B, C, D in the i^{th} sample, respectively. Followed by [93], Eq. 5.5 can be constructed using a matrix form, that is

$$E = \left(\Phi - \Psi X\right)^T \left(\Phi - \Psi X\right) \tag{5.6}$$

where

$$\Psi = \begin{bmatrix} 1 & B_1\left(1,1\right) & C_1\left(1,1\right) & D_1\left(1,1\right) \\ \vdots & \vdots & \vdots & \vdots \\ 1 & B_1\left(l_1,w_1\right) & C_1\left(l_1,w_1\right) & D_1\left(l_1,w_1\right) \\ 1 & B_2\left(1,1\right) & C_2\left(1,1\right) & D_2\left(1,1\right) \\ \vdots & \vdots & \vdots & \vdots \\ 1 & B_n\left(l_n,w_n\right) & C_n\left(l_n,w_n\right) & D_n\left(l_n,w_n\right) \end{bmatrix} X = \begin{bmatrix} log\left(\lambda\right) \\ \alpha \\ \eta \\ \gamma \end{bmatrix} \Phi = \begin{bmatrix} G_1\left(1,1\right) \\ \vdots \\ G_1\left(l_1,w_1\right) \\ G_2\left(1,1\right) \\ \vdots \\ G_n\left(l_n,w_n\right) \end{bmatrix} \tag{5.7}$$

According to multivariate differentiation theory, the optimal solution of Eq. 5.6 must be the stagnation point of E, thus we have

$$\frac{\partial E}{\partial X} = \Psi^T\left(\Phi - \Psi X\right) = 0 \Rightarrow X = \left(\Psi^T\Psi\right)^{-1}\Psi^T\Phi \tag{5.8}$$

To find the optimal solution, we collected several various types of hazy images from flickr.com and several other image search engines using 50 most popular tags annotated by the flickr users. Among these collected images, we select 1,000 images and manually cut out the sky regions to serve as training samples. Note that the selected samples contain different scenes, different haze density, different weather, etc. Here it should be remarked that different sample sets may lead to different optimal solutions, thus a training sample dataset composed of multiple images with different attributes is beneficial to train the optimal solution. After collecting images, the transmission for each sample is estimated

using [4]. With these samples, the unknown coefficients can be directly learned from Eq. 4.8. Through experiments, the final learning results are that $\lambda = 0.8191$, $\alpha = 2.6560$, $\eta = 3.0507$, and $\gamma = 2.3801$. Once these unknown coefficients have been determined, they can be used to compute the transmission map by the Eq. 5.3 for any hazy images. Fig. 5.2 shows the transmission estimated by approach proposed in IDSL. As observed, despite the depth structure of estimated transmission maps are sharp and consistent with the relevant original images, excessive texture details do still exist in these transmission maps, which is not expected for haze removal [63]. Therefore, the guided filter [4] is used to further eliminate these details while maintaining the original depth structure.

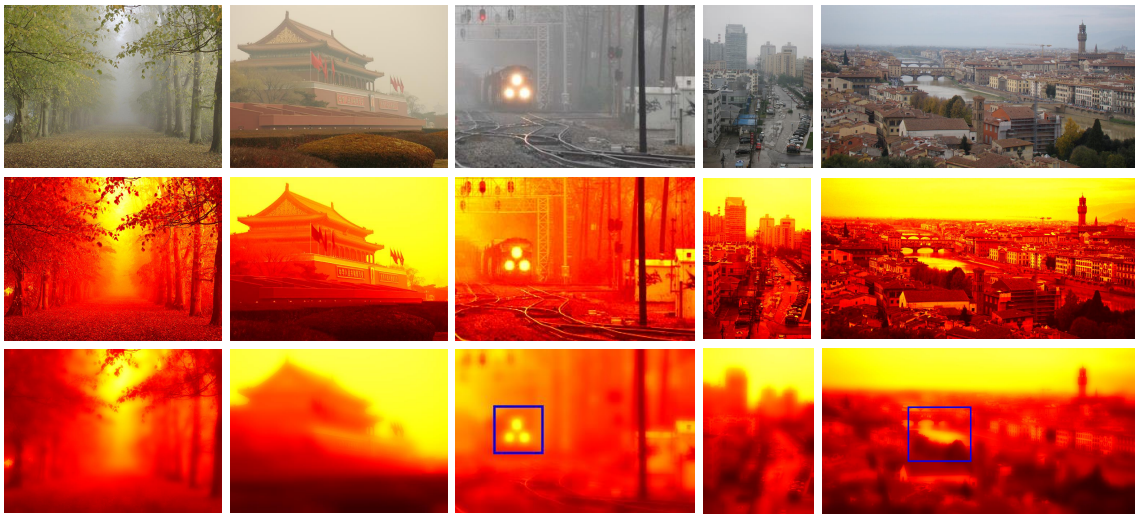

Figure 5.2: Example images and the estimated depth maps. **Top**: Input hazy images. **Middle**: Transmission maps estimated using Eq. 5.3. **Bottom**: The blurred outputs obtained using [4].

5.2.2 Estimation of Scene Incident Light

Different from atmospheric light, scene incident light needs to be firstly estimated for each independent scene. So it is necessary to segment the input image into separated parts.

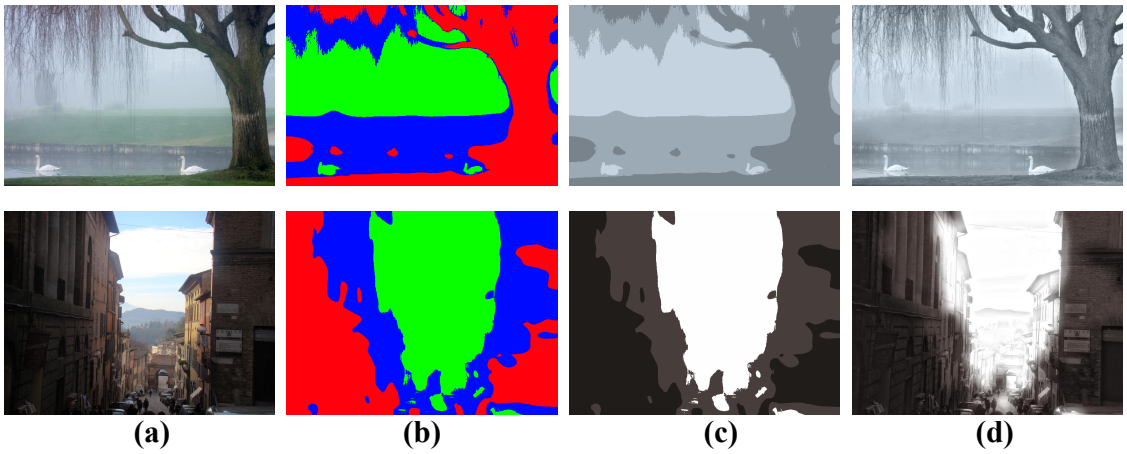

Figure 5.3: The scene incident light estimation procedure. **(a)** Input hazy images. **(b)**The segmentation results (the identical color indicates the same scene). **(c)** The scene incident light (consist of three color components) before edge enhancement. **(d)** The scene incident light (consist of three color components) after edge enhancement.

According to [71], the fuzzy C-means [94] is used to segment the blurred transmission $\tilde{t}$:

$$U = \operatorname{argmin} \left\{ \sum_{i=1}^{c_n} \sum_{j=1}^{res} \mu_i \cdot \left[\tilde{t}\left(j\right)\right]^2 \cdot \left[\tilde{t}\left(j\right) - v_i\right]^2 \right\} \tag{5.9}$$

where μ_i denotes the membership function, $m = 2$ is the weighted index, and $c_n = 3$ is the number of target clusters, v_i is the center of i^{th} cluster, res is the resolution of input image, and U denotes the fuzzy matrix of $\tilde{t}$. With this result, the incident light $L^c\left(i\right)$ for the i^{th} scene can be directly estimated using [4]. Unfortunately, the cluster operator may fail to preserve the edge structure of the original image (see Figs. 5.3(a,b)). To address this issue, a guided energy model (GEM) for enhancing the edge of scene incident light is proposed

$$\tilde{\boldsymbol{L}}^c = \operatorname{argmin} \left\{ \left\| \boldsymbol{L^c} - \tilde{\boldsymbol{L}}^c \right\|_2^2 + \theta \cdot \left\| \nabla \tilde{\boldsymbol{L}}^c - \nabla R \right\|_2^2 \right\} \tag{5.10}$$

where $\theta = 0.5$ is the regularization parameter. The first term imposes that $\boldsymbol{L}^c$ and $\tilde{\boldsymbol{L}}^c$ should be similar, and the second term ensures that the edge features in $\tilde{\boldsymbol{L}}^c$ correspond

to the guiding image $R = \bar{I}$. According to [65], the iterative form of Eq. 5.10 can be expressed as

$$\tilde{\boldsymbol{L}}_{\boldsymbol{j}}^{\boldsymbol{c}}(x,y) = \frac{\boldsymbol{L}^{\boldsymbol{c}}(x,y) - \theta \cdot \left(\sum_{(x',y') \in N(x,y\ )} \left(\tilde{\boldsymbol{L}}_{\boldsymbol{j-1}}^{c}(x',y') - R(x',y') \right) + |N| \cdot R(x,y) \right)}{(1 - \theta \cdot |N|)} \tag{5.11}$$

where $\tilde{L}_j^c$ denotes the j^{th} iteration result, $N(x,y)$ is a 15×15 local patch centered at (x,y), and $|N|$ is the number of pixels in $N(x,y)$. Figs. 5.3(c,d) show the scene incident light before and after the edge enhancement. It is obvious that this scene incident light after enhancement conforms more closely to the realistic distribution of ambient light than does a fixed atmospheric light.

5.2.3 Image Restoration

Now that both scene incident light $\tilde{\boldsymbol{L}}^{\boldsymbol{c}}$ and transmission map $\tilde{t}$ are determined, scene albedo in each color channel $\boldsymbol{\rho}^c$ can be recovered via Sb-ASM (Eq. 5.1) as

$$\boldsymbol{\rho}^c = \frac{\boldsymbol{I}^c - \tilde{\boldsymbol{L}}^{\boldsymbol{c}} \cdot \left(1 - \tilde{t}\right)}{\tilde{\boldsymbol{L}}^{\boldsymbol{c}} \cdot \tilde{t}} \tag{5.12}$$

Simultaneously, to avoid producing too much noise, the transmission $\tilde{t}$ is restricted to a lower bound t_0. Accordingly, the final recovery formula of the scene albedo can be expressed as

$$\boldsymbol{\rho}^c = \frac{\boldsymbol{I}^c - \tilde{\boldsymbol{L}}^{\boldsymbol{c}} \cdot \left(1 - \max\left(\tilde{t}, t_0\right)\right)}{\tilde{\boldsymbol{L}}^{\boldsymbol{c}} \cdot \max\left(\tilde{t}, t_0\right)} \tag{5.13}$$

5.2.4 Accelerating Framework

It is obvious that haze mainly affects the low frequency component of the hazy image. This means dehazing for whole image might involve a large number of redundant computations. To this end, a Gaussian-Laplacian pyramid based accelerating framework (AF) is proposed. The step-by-step of AF is described as following:

Step 1: Decompose the hazy image $\boldsymbol{I}$ into low frequency component I_l and high frequency component $I_h^1, I_h^2, ..., I_h^k$ via the Gaussian-Laplacian pyramid.

Step 2: Dehaze the low frequency component I_l using the proposed IDSL, and its recovery result is denoted as $I_{l-dehazed}$.

Step 3: Enhance the high frequency component by

$$\tilde{I}_h^i = \delta \cdot (k-i) \cdot \left(\left(\max \left(1 - \frac{\zeta}{\xi} \right) \right) \downarrow^{2 \cdot i} + 1 \right) \cdot I_h^i, i \in \{1, 2, ..., k\} \tag{5.14}$$

where ξ is just noticeable difference (JND) of luminance component [95], ζ is the actual pixel difference, and $\delta = 2$ is the empirical parameter.

Step 4: Reconstruct the haze-free image via pyramid reconstruction with $I_h^1, I_h^2, ..., I_h^k$ and $\mathrm{I}_{l-dehazed}$. Fig. 5.4 reveals the recovery results of IDSL both with and without AF. As a tradeoff, $k = 3$ is selected in IDSL.

Figure 5.4: Dehazing results with and without the AF (with different values of k).

5.3 Experimental Comparison and Analysis

In the following experiments, all the algorithms are implemented in the Matlab (R2014a) environment on a PC with Intel(R) Core(TM) i5-4300M CPU with 2.60GHz and 8.00 GB RAM. The parameters of our proposed IDSL are set as described in above.

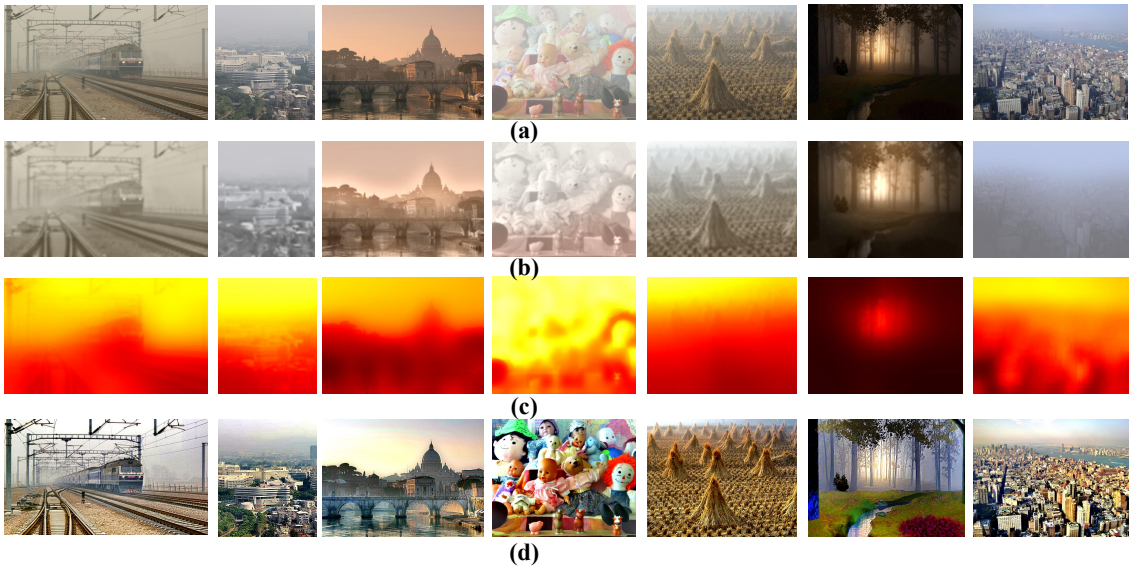

Figure 5.5: Dehazing Performance of IDSL. **(a)** Hazy images. **(b)** The estimated scene incident light (enlarged 16 times). **(c)** The estimated transmission maps (enlarged 16 times). **(d)** Dehazing results using IDSL.

5.3.1 Recovery Quality

Without loss of generality, different types of hazy images are picked and the performance of IDSL is tested on them. Some of the results are shown in Fig. 5.5; Fig. 5.5(a) displays several hazy images, Figs. 5.5(b) and 5.5(c) show the corresponding estimated scene incident light and transmission map, respectively; Fig. 5.5(d) presents the results resorted by the proposed IDSL. As can be seen, the haze cover in these images is removed completely and most of the scene objects can be noticed clearly, the overall contrast is also significantly increased, while the estimated transmission and scene incident light are both consistent with our intuitions.

5.3.2 Qualitative Comparison on Real-World Images

Although most current techniques are able to generate good results for single input images, it is hard to compare them visually. For fair comparison, we carried out the test among different methods on some challenging real-world images including images with mist, dense haze, gray-white region, sky region and uneven illumination. Fig. 5.6 shows the comparison of dehazing results with the ten state-of-the-art dehazing techniques [34, 56, 63, 69, 84, 96, 97] on challenging real-world images. Fig. 5.6(a) depicts the hazy images to be dehazed. Figs. 5.6(b-k) show the results of the methods of DEFADE [34], FVR [63], A-DCP [96], NC [97], CAP [56], DehazeNet [84], MSCNN [69], respectively. The results of the IDSL are given in Fig. 5.6(l). As can be seen from Fig. 5.6(b), DEFADE's results are not visually compelling since the results are generated using a multi-scale fusion strategy and the image degradation mechanism is not taken into account (for instance, the recovered color of the human face in the first image and the rocks in the third image are significantly inconsistent with their appearances should be). In Fig. 5.6(c), the results using FVR can recover abundant texture details; however, the visual effect is over-enhanced (see the rocks of the third image). The reason is that the estimated atmospheric veil is an extreme case based on the DCP and the problem of overestimating transmission is inevitable. Moreover, halo artifacts appear nearby to the depth jumps (see the details demonstrated in the yellow box of the second image) due to the poor edge-preserving behavior of the median filter used in [63]. In contrast, A-DCP can significantly improve the visual effect of the haze images, but the color shift phenomenon still exists in the region with white objects (see the green box of the fourth image in Fig. 5.6(d)) because the dark channel has bright values near such objects. In Fig. 5.6(e), it can be noticed that the image recovered using NC generally looks dim, since the haze removal magnitude which is determined via a negative correction strategy would lead to the over-decreasing

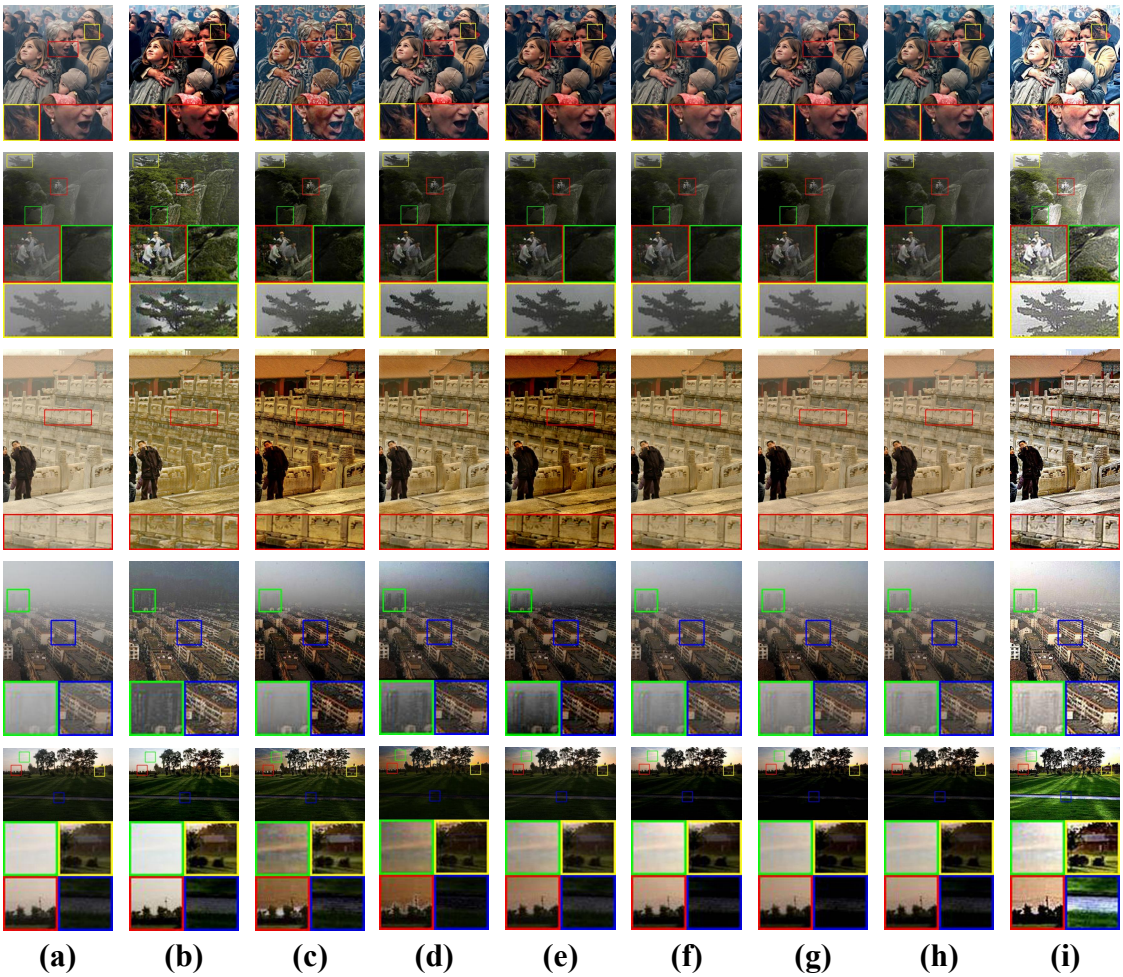

Figure 5.6: Qualitative comparison of different methods on real-world images. **(a)** Hazy images. **(b)** DEFADE. **(c)** FVR. **(d)** A-DCP. **(e)** NC. **(f)** CAP. **(g)** DehazeNet. **(h)** MSCNN. **(i)** IDSL.

of the true scene brightness (see the third image). As we discussed in above, the fixed scattering coefficient does not always conform to the real world, and for this reason, the dehazing results of CAP are not quite satisfactory for dense hazy image (see the zoom-in of Fig. 5.6(f)). As we can observe in Figs. 5.6(g,h), DehazeNet and MSCNN can avoid the over-enhancement for the sky regions using the machine learning framework, but the dehazing effect for the non-sky regions is relatively weak, which may be caused by the insufficient training samples. Compared with the results of these techniques, IDSL has better performance in terms of haze removal ability, color fidelity and visual effect (see Fig. 5.6(i)). Furthermore, as depicted in the last row of Fig. 5.6, IDSL outperforms the other algorithms in aspect of overall contrast.

5.3.3 Qualitative Comparison on Synthetic Images

To verify the effectiveness on complete images, the proposed IDSL is also tested on synthesized hazy images from stereo images with a known depth map, and compared with the ten method mentioned above. We choose 6 pairs of stereo images from the Middlebury Stereo Dataset [81–83] and D-HAZY Dataset [85]. The hazy images are synthesized from the haze-free images using the known depth maps and ASM, as shown in Fig. 5.7(a). The dehazing results of different approaches are shown in Fig. 5.7(b-l). Fig. 5.7(m) gives the ground truth images for comparison. As we can see in Fig. 5.7(b-c), the results of DEFADE and FVR are subject to significant over-enhancement and tend to be darker than the ground truth images. the results using A-DCP are more consistence with the ground truth images, but the color shift appears in the white desk of the last image of Fig. 5.7(d). As shown in Fig. 5.7(e), NC can enhance details of hazy images and can achieve fine effect generally. However, for the desk image, the floor looks too dark and haze remains in the upper part. By observing the images in Fig. 5.7(f-h), we can find that the results of CAP, DehazeNet, and MSCNN are still covered with mist. For ex-

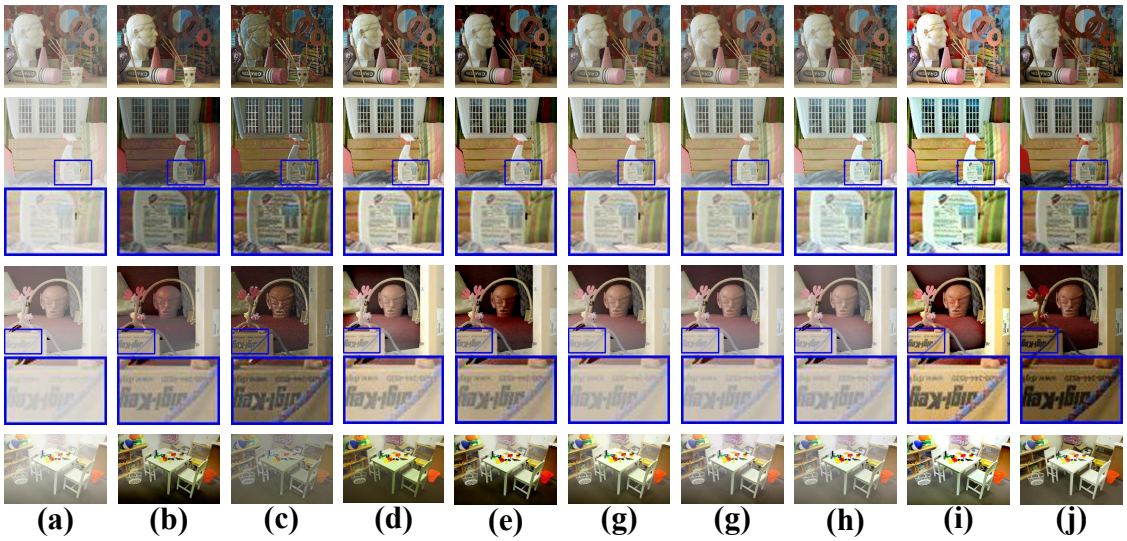

Figure 5.7: Results on Synthetic images for which the ground truth images are known. **(a)** Hazy images. **(b)** DEFADE. **(c)** FVR. **(d)** A-DCP. **(e)** NC. **(f)** CAP. **(g)** DehazeNet. **(h)** MSCNN. **(i)** IDSL. **(j)** Ground Truth.

ample, the texture details of the laundry image and the reindeer image are still blurred, especially within the zoom-in patches. In contrast, the results dehazed by IDSL maintain the original tone of the true scene, avoid the over-enhancement and recover more vivid color than the relevant ground truth images (see Fig. 5.7(i,j)).

5.3.4 Quantitative Comparison

To quantitatively assess and rate these algorithms, six well-known evaluation indexes are employed in this work. Fog Aware Density Evaluator (FADE) predicts the visibility on a hazy scene without reference to a corresponding haze-free image, and it correlates well with human judgments of haze density [34]. Structural similarity (SSIM) image quality assessment index evaluates the ability to preserve the structural information of the algorithms [87]. Mean squares error (MSE) indicates the average difference between the recovered image and the reference ground truth image. According to [86], the percentage

of new visible edges e represents edges that are newly visible after restoration, the contrast restoration quality $\bar{r}$ measures the mean ratio of the gradients at the visible edges, and the saturation Σ computes the percentage of pixels that become completely black or completely white after restoration. In general, the smaller value of FADE implies the lower perceptual haze density; a higher SSIM means better structure similarity between the recovered image and the ground truth image; a lower MSE represents that the recovered image is more acceptable; a higher value of e and a value of Σ closer to zero imply better performance, and a higher value of $\bar{r}$ implies stronger recovery of the local contrast.

The corresponding assessment results are listed in Table 5.1. In summary, IDSL usually achieves the smallest value of FADE, the highest value of $\bar{r}$ and e, and the second-highest value of SSIM, as well as the saturation Σ is nearly close to zero; but the MSE value of our algorithm is relatively higher than others, whereas this does not imply the poor performance for IDSL, since it has the illumination compensation ability which may cause the difference between the dehazing result and the relevant ground truth image.

The computational complexity is another important evaluation factor for a dehazing algorithm. In Fig. 5.8, we give the computational time comparison of different methods using Fig. 5.7 (with different resolutions). As we can see, IDSL is much faster than those of DEFADE, FVR, DehazeNet and slightly faster than A-DCP, NC, CAP, MSCNN and it has high efficiency even when the resolution of the input image is large. This advantage of efficiency mainly benefits from the proposed linear model for the transmission estimation and the designed AF. Overall, the qualitative and quantitative comparison results in Figs. 5.6, 5.7 and Table 5.1 demonstrate that IDSL has advantages over other state-of-the-art dehazing methods in terms of haze removal, visibility improvement, and illumination compensation, while avoiding most of the negative effects.

Table 5.1: Quantitative comparison of the dehazing results shown in Fig. 5.7 using FADE, SSIM, r, Σ, e, and MSE

Index	Image	DEFADE	FVR	A-DCP	NC	CAP	DehazeNet	MSCNN	IDSL
FADE	art	0.30	0.16	0.22	0.14	0.33	0.36	0.37	0.14
	laundry	0.36	0.26	0.32	0.25	0.47	0.54	0.48	0.19
	reindeer	0.62	0.35	0.45	0.37	0.68	0.86	0.99	0.28
	desk	0.35	0.84	0.46	0.38	0.69	0.96	0.99	0.31
SSIM	art	0.83	0.78	0.85	0.76	0.85	0.84	0.77	0.84
	laundry	0.78	0.85	0.90	0.89	0.88	0.87	0.82	0.90
	reindeer	0.70	0.81	0.67	0.71	0.67	0.63	0.56	0.81
	desk	0.73	0.77	0.81	0.71	0.83	0.83	0.79	0.81
MSE	art	0.46	0.152	1.03	0.08	1.18	1.35	2.48	5.37
	laundry	0.15	0.19	2.97	1.01	4.02	4.18	6.24	5.72
	reindeer	4.51	0.61	8.91	3.43	8.61	9.84	12.58	7.20
	desk	0.46	0.70	0.29	0.85	2.07	2.63	3.63	2.47
$\overline{r}$	art	1.30	1.84	1.72	1.44	1.26	1.23	1.40	2.27
	laundry	1.52	2.48	2.44	2.21	1.87	1.68	2.11	3.61
	reindeer	1.78	2.23	2.19	1.74	1.63	1.54	1.66	3.24
	desk	1.88	1.54	1.91	2.05	1.83	1.53	1.54	4.12
e	art	0.31	0.74	0.30	0.30	0.21	0.20	0.22	0.49
	laundry	1.01	1.31	0.78	0.76	0.62	0.56	0.58	1.37
	reindeer	1.48	2.71	1.39	1.46	1.09	0.84	0.74	1.98
	desk	2.51	2.42	2.59	2.21	2.19	1.76	0.56	3.06
Σ	art	0.00	0.00	0.00	0.01	0.00	0.00	0.00	0.00
	laundry	0.01	0.00	0.01	0.03	0.00	0.00	0.00	0.00
	reindeer	0.00	0.00	0.02	0.06	0.00	0.00	0.00	0.00
	desk	0.04	0.00	0.02	0.01	0.00	0.00	0.00	0.02

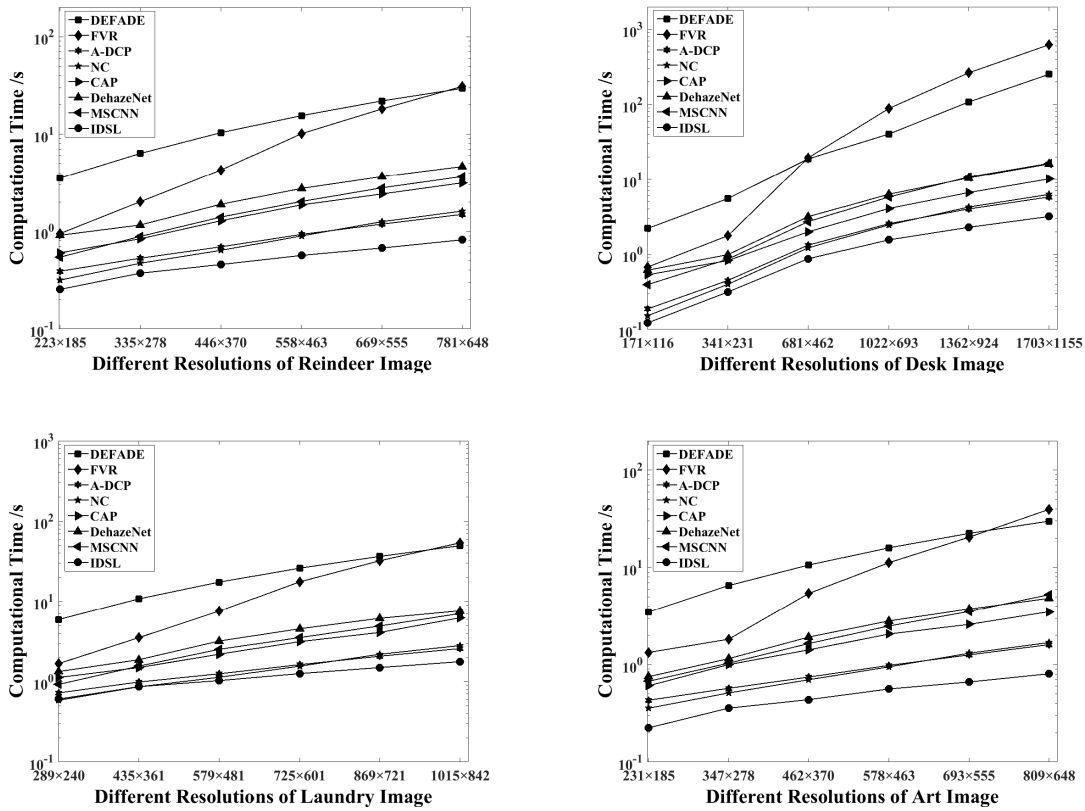

Figure 5.8: Time comparison of different algorithms using Fig. 5.7 (with different resolutions)

5.4 Conclusions

Atmospheric scattering model (ASM) is formulated under the even illumination assumption, which might be invalid under some particular scenarios. In this chapter, a scene-based ASM (Sb-ASM) is proposed by replacing atmospheric light as the scene incident light. Taking Rb-ASM as the imaging theory of hazy images, a fast single image dehazing algorithm named IDSL has been later presented. In IDSL, the transmission estimation process is coverted to a linear operation on the three known components related to the hazy image, which significantly reduces the computation efficiency of haze removal. Based on the proposed GEM, the the scene incident light can be easily obtained, thereby recovering the scene albedo via Rb-ASM. Besides, an AF that uses Gaussian-Laplacian pyramid is further provided to improve the computational efficiency. Experimental results demonstrate that IDSL achieves dramatically high efficiency and outstanding dehazing effects.

Chapter 6

BDPK: Bayesian Dehazing Using Prior Knowledge

In this chapter, a pixel-based ASM (Pb-ASM), which is extremely adaptable for various practical scenarios, is proposed to overcome the issue of inhomogeneous haze. Benefiting from this Pb-ASM, a Bayesian dehazing dehazing algorithm (BDPK) is developed by merging the prior knowledge. The strategy of BDPK is to convert the single image dehazing task into a maximum a-posteriori probability (MAP) model that can be approximated as an optimization function using the existing priori constraints. To efficiently solve this optimization function, the alternating minimizing technique (AMT) is introduced, which enables us to directly restore the scene albedo from optimization function.

6.1 Pixel-based ASM (Pb-ASM)

Besides the uneven illumination limitation described in Chapter 5, ASM also lacks the capability to deal with the images with inhomogeneous haze. The key reason is that the scattering coefficient is set to be a constant. Actually, $\beta_0 - constant$ assumption would face the difficulties when processing the inhomogeneous haze cases (see Fig. 6.1). Accord-

ingly, we break this plausible assumption, i.e., redefine the constant β as the scattering distribution β_0 that varies along with the pixel coordinate. Based on above analysis, a more reliable pixel-based ASM (Pb-ASM) is obtained as

$$\boldsymbol{I}(x,y) = \boldsymbol{L}(i) \cdot \boldsymbol{\rho}(x,y) \cdot e^{-\beta(x,y)\cdot d(x,y)} + \boldsymbol{L}(i) \cdot \left(1 - e^{-\beta(x,y)\cdot d(x,y)}\right), (x,y) \in \Omega(i) \quad (6.1)$$

where $\beta(x,y)$ represents the scattering value for pixel coordinate (x,y). Note that the atmospheric light in Pb-ASM is replaced scene incident light defined in Rb-ASM, which aims at simultaneously overcoming the problems of uneven illumination and inhomogeneous haze. Although Pb-ASM is more in line with the real world compared to ASM and Sb-ASM, it is a more challenge task when using the proposed model to dehaze because the available structure information is significantly insufficient.

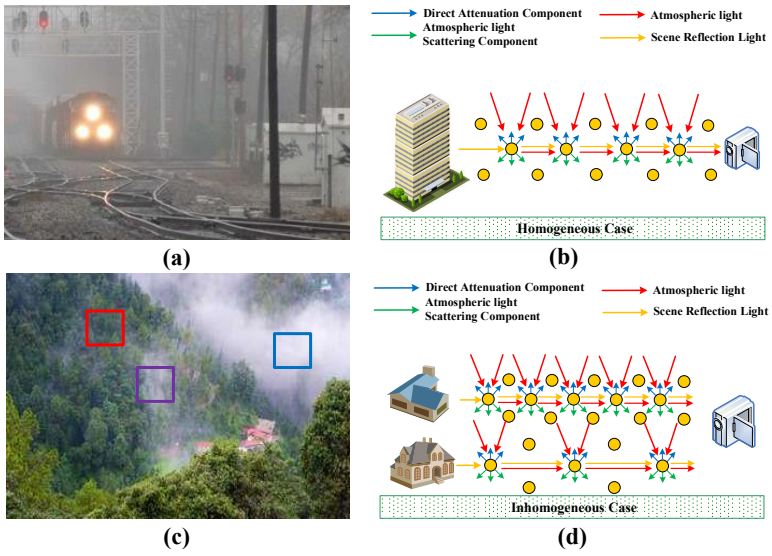

Figure 6.1: **(a)** Homogeneous atmosphere case. **(b)** Atmosphere scattering model illustrated for homogeneous case. **(c)** Inhomogeneous atmosphere case (Distribution of suspended particles varies among the different color boxes). **(d)** Atmosphere scattering model illustrated for inhomogeneous case.

6.2 Proposed BDPK

As we explained in Chapter 2, the success of single image haze removal depends on the validity of the prior knowledge, whereas the limitations of the aforementioned priors are inevitable in some exceptional circumstances. To this end, a Bayesian theory based image dehazing technique called BDPK is developed. It can compensate for these shortcomings and deal with the inhomogeneous haze image by fully leveraging the latent relationships of the image priors, and thereby recover the more visually comfortable results.

6.2.1 MAP Model

Motivated by [98–100], the key step of BDPK is to factorize the hazy image $\boldsymbol{I}$ into scene albedo $\boldsymbol{\rho}$, scene depth d and scattering distribution β for each pixel across the entire input. To avoid Pb-ASM, i.e., Eq. 6.1, being nonnegative, we first reverse it as

$$\boldsymbol{L}(i) - \boldsymbol{I}(x,y) = \boldsymbol{L}(i) \cdot (1 - \boldsymbol{\rho}(x,y)) \cdot e^{-\beta \cdot d(x,y)}, (x,y) \in \Omega(i) \tag{6.2}$$

Afterwards, taking the logarithm operation of each side in Eq. 6.2 yields

$$\ln(\boldsymbol{L}(i) - \boldsymbol{I}(x,y)) = \ln(\boldsymbol{L}(i) \cdot (1 - \boldsymbol{\rho}(x,y))) - \beta(x,y) \cdot d(x,y), (x,y) \in \Omega(i) \tag{6.3}$$

Considering the noise from sensors is another important degradation factor [99] and letting $\boldsymbol{I}'(x,y) = \ln(\boldsymbol{L}(i) - \boldsymbol{I}(x,y))$, $\boldsymbol{\rho}'(x,y) = \ln(\boldsymbol{L}(i) \cdot (1 - \boldsymbol{\rho}(x,y)))$, Eq. 6.3 can be simplified as

$$\boldsymbol{I}'(x,y) = \boldsymbol{\rho}'(x,y) - \beta(x,y) \cdot d(x,y) + n(x,y) \tag{6.4}$$

where n denotes additive noise. If incident light $\boldsymbol{L}$ has been estimated using the method described in Chapter 5, we can regard $\boldsymbol{I}'$ as the "new hazy image" since it is a known component and contains all the information of $\boldsymbol{I}$. Similarly, $\boldsymbol{\rho}'$ can be considered as the

"haze-free image". According to Bayesian theory, the posterior probability constituted by all parameters in Eq. 6.4 can be described as

$$p\left(\boldsymbol{\rho}', \beta, d|\, \boldsymbol{I}'\right) = \frac{p\left(\boldsymbol{I}'|\, \boldsymbol{\rho}', \beta, d\right) \cdot p\left(\boldsymbol{\rho}'|\, \beta, d\right) \cdot p\left(\beta|\, d\right) \cdot p\left(d\right)}{p\left(\boldsymbol{I}'\right)} \tag{6.5}$$

where $p\left(\boldsymbol{I}'\right)$ is a determined constant due to the given $\boldsymbol{I}'$. Moreover, it can be noticed that $\boldsymbol{\rho}'$, β, and d are totally uncorrelated in the real world. Therefore, equation Eq. 6.5 is further equivalent to

$$p\left(\boldsymbol{\rho}', \beta, d|\, \boldsymbol{I}'\right) \propto p\left(\boldsymbol{I}'|\, \boldsymbol{\rho}', \beta, d\right) \cdot p\left(\boldsymbol{\rho}'|\, \beta, d\right) \cdot p\left(\beta\right) \cdot p\left(d\right) \tag{6.6}$$

To restore the "haze-free image" $\boldsymbol{\rho}'$, we take the logarithm operation of each side in 6.6 and then maximize its posterior probability. Accordingly,the maximum a posteriori probability (MAP) model for haze removal can be expressed as

$$\begin{aligned} &\arg\max\left\{p\left(\boldsymbol{\rho}', \beta, d|\, \boldsymbol{I}'\right)\right\} \\ &\propto \arg\min\left\{-\ln\left(p\left(\boldsymbol{I}'|\, \boldsymbol{\rho}', \beta, d\right)\right) - \ln\left(p\left(\boldsymbol{\rho}'\right)\right) - \ln\left(p\left(\beta\right)\right) - \ln\left(p\left(d\right)\right)\right\} \end{aligned} \tag{6.7}$$

where we have explicitly illustrated the inner relationship among all the probability density functions of imaging factors in Eq. 6.6. This is premise for approximating the optimization function of image haze removal.

6.2.2 Model Approximation

MAP model for haze removal is given, but it is a fundamentally under-constrained problem due to the insufficient available information. Fortunately, some image priors have been explored. This inspires us to design each probability density function (PDF) to approximate an optimization function corresponding to Eq. 6.4, which enables us to directly restore the scene albedo.

Definition I: To alleviate the model's complexity, we assume the additive noise n is white Gaussian noise. Additionally, based on the fact that the relationship among all the

parameters is constrained to Eq. 6.3 [Model Constraint Prior], we might as well define

$$p\left(\boldsymbol{I}'\right|\rho', \beta, d) = e^{-\frac{\|\boldsymbol{I}'-\boldsymbol{\rho}'+\beta\cdot d\|_2^2}{\lambda_1}} \tag{6.8}$$

where λ_1 is the variance of the exponential power distribution (Please note that the subsequent parameters λ_2, λ_3 and λ_4 have the same meaning as λ_1). The above PDF restricts the solution space of all unknown components and thus ensures the authenticity of the recovery result.

Definition II: Haze-free images possess higher visibility than the corresponding hazy ones [39], which indicates that richer image contrast information results in a higher probability that the scene is a real scene [Contrast Prior]. Following this hypothesis, the PDF of ρ' is defined as

$$p\left(\boldsymbol{\rho}'\right) = e^{-\frac{\|(F-\nabla\boldsymbol{\rho}')\|_2^2}{\lambda_2}} \tag{6.9}$$

where F is the maximum upper limit of $\nabla\boldsymbol{\rho}'$. In addition to the highlighted pure-white objects, we roughly generalize that $\nabla\boldsymbol{\rho}' \in [0, 4.6]$ due to $\boldsymbol{L}\left(i\right) \cdot \left(1 - \boldsymbol{\rho}\left(x, y\right)\right) \in [0.01, 1]$ in general. Thus, we set $F = 5$. Although the contrast prior could basically reflect the objective discipline of the scene albedo, the results recovered by Tan [39] indicate that solely stressing the enhanced of visibility in the degraded image may lead to the over-saturated phenomenon. To address the limitation of the contrast prior used in the PDF (Eq. 6.9), an esthesia matrix on haze density is introduced. It is expressed as

$$W = e^{-\frac{(\bar{I}-1)^2}{\sigma}} \cdot e^{-\frac{(I^\sigma)^2}{\sigma}} \tag{6.10}$$

where $\sigma = 0.3$ is a prescribed coefficient, $\bar{I}$ and I^σ are the brightness component and saturation component of input $\boldsymbol{I}$, respectively. It is obvious that the quantization value of the matrix is proportional to scene brightness and inversely proportional to saturation, which conforms to human visual perception (HVP) for natural haze [56]. Taking this esthesia matrix (Eq. 6.10), the final PDF of ρ' can be rewritten as

$$p\left(\boldsymbol{\rho}'\right) = e^{-W\cdot\frac{\|F-\nabla\boldsymbol{\rho}'\|_2^2}{\lambda_2}} \tag{6.11}$$

where W is able to flexibly control the contrast weights for all pixels with respect to the HVP. Generally, a thicker haze density results in a greater contrast weight. This strategy promises the restoration quality for dense hazy scenes and avoids the over-enhancement of the misty ones.

Definition III: A "good" depth map should preserve the overall depth structure consistent with the original hazy image. Hence, the PDF of d can be defined as

$$p\left(d\right) = e^{\frac{-\gamma_1 \cdot \|d-d\|_2^2 - \gamma_2 \|\nabla d\|_2^2 - \gamma 3 \cdot \|\nabla d - \nabla I\|_2^2}{\lambda 3 \cdot (\gamma 1 + \gamma 2 + \gamma 3)}} \tag{6.12}$$

where γ_1, γ_2, and γ_3 are weight coefficients and find represents the initial estimation of the scene depth. Referring to [98, 101], the minimal component of $\boldsymbol{I}$ can be regarded as the closest depth, thus we initialize this component as the initial depth, that is

$$\tilde{d} = \min_{c \in \{R,G,B\}} \left(I^c\left(x,y\right)\right) \tag{6.13}$$

where c denotes color channel index and I^c is a color channel of $\boldsymbol{I}$.

Definition IV: Similar to scene depth, we notice that the scattering distribution equally shares the original spatial structure and local smoothing feature (see Fig. 6.1(c)). Based on this observation, the PDF of β is defined as

$$p\left(\beta\right) = e^{\frac{-\gamma_4 \cdot \|\beta-\beta\|_2^2 - \gamma_5 \|\nabla \beta\|_2^2 - \gamma_6 \cdot \|\nabla \beta - \nabla I\|_2^2}{\lambda_4 \cdot (\gamma_4 + \gamma_5 + \gamma_6)}} \tag{6.14}$$

where γ_4, γ_5, and γ_6 are weight coefficients and β represents the initial estimation of the scattering distribution. Here, two different atmospheric conditions are required to be taken into account: 1) Regarding the homogeneous case, we set $\beta = 1$, which has been proven to be ample for most situations [56]; 2) The brightness of pixels in an inhomogeneous image usually sharply varies along with the change of the concentration of atmospheric particles (see Fig. 6.1(c)). Thus, we initialize the estimation $\tilde{\beta} = \bar{I}$ for inhomogeneous case.

Optimization Function: Substituting the created PDFs (Eq. 6.8, Eq. 6.11, Eq. 6.12, and Eq. 6.14) into the MAP model (Eq. 6.7), the optimization function for haze removal can be approximated as

$$\begin{aligned}&\arg\min\left\{p\left(\boldsymbol{\rho}', \beta, d|\, \boldsymbol{I}'\right)\right\}\\&= \arg\min\left(\theta_1 \cdot \|\boldsymbol{I}' - \boldsymbol{\rho}' + \beta \cdot d\|_2^2 + \theta_2 \cdot W \cdot \|F - \nabla\rho'\|_2^2 + \theta_3 \cdot \left\|d - \tilde{d}\right\|_2^2 + \theta_4 \cdot \|\nabla d\|_2^2\right.\\&\quad\left.+\theta_5 \cdot \left\|\nabla d - \nabla\bar{I}\right\|_2^2 + \theta_6 \left\|\beta - \tilde{\beta}\right\|_2^2 + \theta_7 \|\nabla\beta\|_2^2 + \theta_8 \left\|\nabla\beta - \nabla\bar{I}\right\|_2^2\right)\end{aligned} \tag{6.15}$$

where $\theta_1 = \frac{1}{\lambda_1}$, $\theta_2 = \frac{1}{\lambda_2}$, $\theta_3 = \frac{\gamma_1}{\lambda_3(\gamma_1+\gamma_2+\gamma_3)}$, $\theta_4 = \frac{\gamma_2}{\lambda_3(\gamma_1+\gamma_2+\gamma_3)}$, $\theta_5 = \frac{\gamma_3}{\lambda_3(\gamma_1+\gamma_2+\gamma_3)}$, $\theta_6 = \frac{\gamma_4}{\lambda_4(\gamma_4+\gamma_5+\gamma_6)}$, $\theta_7 = \frac{\gamma_5}{\lambda_4(\gamma_4+\gamma_5+\gamma_6)}$, and $\theta_8 = \frac{\gamma_6}{\lambda_4(\gamma_4+\gamma_5+\gamma_6)}$ are regular parameters. Minimizing Eq. 6.15 is computationally intractable because of too many unknown components. In the following section, we will introduce an efficient optimization technique to obtain $\boldsymbol{\rho}'$, β and d.

6.2.3 Effective Recovering

Instinctively, we employ the alternating minimizing technique(AMT) [102] to solve the optimization function (Eq. 6.15). The core idea of AMT is to alternatively minimize β, d, and ρ' by assuming that the other components are known. This process is repeated until they converge. Specifically, Eq. 6.15 is first separated into three independent sub-problems, which are expressed as

$$d = \arg\min\left\{\theta_1 \cdot \|\boldsymbol{I}' - \boldsymbol{\rho}' + \beta \cdot d\|_2^2 + \theta_3 \cdot \left\|d - \tilde{d}\right\|_2^2 + \theta_4 \cdot \|\nabla d\|_2^2 + \theta_5 \cdot \left\|\nabla d - \nabla\bar{I}\right\|_2^2\right\} \tag{6.16}$$

$$\beta = \arg\min\left\{\theta_1 \cdot \|\boldsymbol{I}' - \boldsymbol{\rho}' + \beta \cdot d\|_2^2 + \theta_6 \left\|\beta - \tilde{\beta}\right\|_2^2 + \theta_7 \|\nabla\beta\|_2^2 + \theta_8 \left\|\nabla\beta - \nabla\bar{I}\right\|_2^2\right\} \tag{6.17}$$

$$\rho' = \arg\min\left\{\theta_1 \cdot \|\boldsymbol{I}' - \boldsymbol{\rho}' + \beta \cdot d\|_2^2 + \theta_2 \cdot W \cdot \|F - \nabla\boldsymbol{\rho}'\|_2^2\right\} \tag{6.18}$$

To accelerate the calculation, the gradient approximation method [71] is selected to resolve sub-problems (Eq. 6.16, Eq. 6.17, and Eq. 6.18). Then, their optimal solutions after the

j^{th} iteration can be computed as

$$d_{(j)} = \frac{-\theta_1 \cdot \beta_{(j-1)} \circ M_1 + \sum \cdot (\theta_4 + \theta_5) \cdot M_3 + \theta_3 \cdot \tilde{d} + M_5}{\theta_1 \circ \beta_{(j-1)} \circ d_{(j-1)} + \sum {}^2 \cdot (\theta_4 + \theta_5) + \theta_3} \tag{6.19}$$

$$\beta_{(j)} = \frac{-\theta_1 \cdot d_{(j-1)} \circ M_1 + \sum \cdot (\theta_7 + \theta_8) \cdot M_2 + \theta_6 \cdot \tilde{\beta} + M_6}{\theta_1 \circ d_{(j-1)} \circ d_{(j-1)} + \sum {}^2 \cdot (\theta_7 + \theta_8) + \theta_6} \tag{6.20}$$

$$\rho'_{(j)} = \frac{\theta_1 \cdot \left(I' + \beta_{(j-1)} \circ d_{(j-1)}\right) + \theta_2 \sum \cdot (M_4 + F)}{\theta_1 + \theta_2 \cdot \sum {}^2 \cdot W} \tag{6.21}$$

where $\boldsymbol{M}_1 = \boldsymbol{I'} - \boldsymbol{\rho'}_{(j-1)}$, $M_{2=}\beta_{(j-1)} \otimes \Lambda$, $M_{3=}d_{(j-1)} \otimes \Lambda$, $\boldsymbol{M}_{4=}\boldsymbol{\rho'}_{(j-1)} \otimes \Lambda$, $\boldsymbol{M}_{5=}\theta_5 \cdot \Sigma \cdot \left(\Sigma \cdot \boldsymbol{I} - \bar{I} \otimes \Lambda\right)$, $\boldsymbol{M}_6 = \theta_8 \cdot \Sigma \cdot \left(\Sigma \cdot \boldsymbol{I} - \bar{I} \otimes \Lambda\right)$, $\circ$ and $\otimes$ represent element-wise multiplication and convolution operator respectively. $\Lambda = [0, 1, 0; 1, 0, 1; 0, 1, 0]$ is the convolution kernel and $\Sigma = 4$ is the sum of elemental value in Λ. It should be noted that, the mathematical meaning of PDFs (Eq. 6.12 and Eq. 6.14) constructed using the structure prior are very similar to those of the guided image filter [29], the guided joint bilateral filter [50], and the guided total variation model [71]. However, the corresponding solution formulas (Eq. 6.19 and Eq. 6.21) are not the simple filtering process due to the interaction of each imaging parameter during the iteration procedure. Once the stop criterion $\left\|\rho'_j - \rho'_{j-1}\right\|_1 / \left\|\rho'_j\right\|_1 \leq \eta$ or the maximal number of iterations $j_{\max}$ is satisfied, the iteration is terminated and the scene albedo can be restored as

$$\boldsymbol{\rho'}(x, y) = \frac{\boldsymbol{L}(i) - e^{\boldsymbol{\rho'}(x,y)}}{\boldsymbol{L}(i)} \tag{6.22}$$

To achieve a better balance between accuracy and efficiency, we empirically provide the parameters for different atmospheric conditions as listed in Table 6.1. Fig. 6.2 shows two dehazing examples of homogeneous and inhomogeneous atmospheres using our BDPK by setting $j_{\max} \in (5, 10, 15)$ with $\eta = 0$. It can be noticed that, increasing the number of iterations, more thoroughly removes the haze, and the scattering distribution map as well as scene depth are more in accordance with our intuitions. Interestingly, we do not state that the scattering value is correlated with altitude, even though the left scattering map

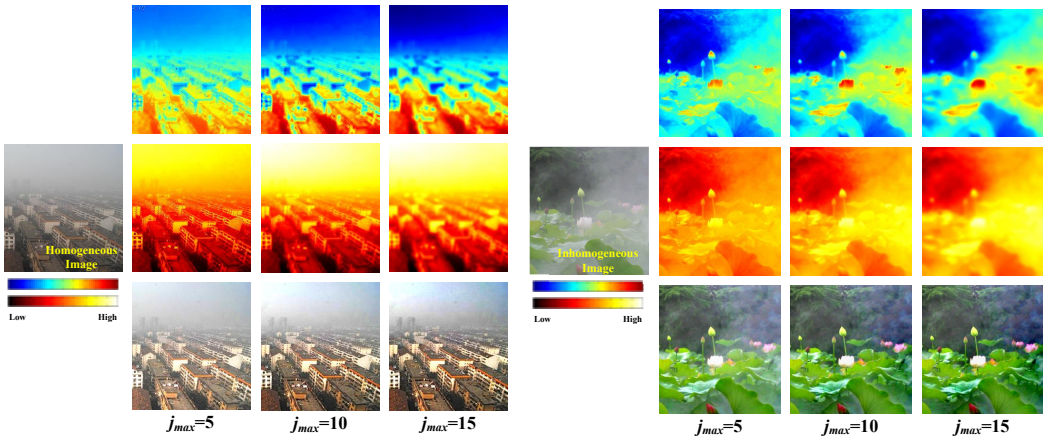

Figure 6.2: Two dehazing examples of different types of hazy images using our BDPK by setting the $j_{max} \in \{5, 10, 15\}$ with $\eta = 0$. **Top**: The scattering distribution maps (Best viewed in color). **Middle**: The scene depth maps (Best viewed in color). **Bottom**: The restored haze-free images.

Table 6.1: The empirical parameters of different atmospheric conditions used in BDPK

Condition	θ_1	θ_2	θ_3	θ_4	θ_5	θ_6	θ_7	θ_8
Homogeneous	3	0.1	0.5	$0.5 + (j-1)$	0.5	0.5	$0.5 + (j-1)$	0.5
Inhomogeneous	3	0.3	0.5	$0.5 + 2 \cdot (j-1)$	0.5	0.5	$0.5 + 2 \cdot (j-1)$	0.5

estimated by BDPK in Fig. 6.2 obviously is affected by gravity [103]. This precise result illustrates that our BDPK has the ability to merge the advantages of all introduced priors by reasonably selecting a set of regular parameters.

6.3 Experimental Comparison and Analysis

In this section, the relevance analyses of all priors introduced in BDPK are first illustrated experimentally. Next, we test BDPK on various hazy images and compare with the well-known techniques, including BD [101], BFCD [99], SIBF [100], OCE [55], MCP [39], MPE [30], FVR [63], DCP [4], SIIM [71], BCCR [51], CAP [56], and DN [85]. Among

Table 6.2: The regular parameters used in BDPK for the recovery results shown in Fig. 6.3.

Recovery Results	θ_1	θ_2	θ_3	θ_4	θ_5	θ_6	θ_7	θ_8
Fig. 6.3A	0	0.1	0.5	$0.5+(j-1)$	0.5	0.5	$0.5+(j-1)$	0.5
Fig. 6.3B	3	0	0.5	$0.5+(j-1)$	0.5	0.5	$0.5+(j-1)$	0.5
Fig. 6.3C	3	0.1	0	0	0	0.5	$0.5+(j-1)$	0.5
			set $d=\tilde{d}$ directly					
Fig. 6.3D	3	0.1	0.5	$0.5+(j-1)$	0.5	0	0	0
						set $\beta=\tilde{\beta}$ directly		
Fig. 6.3E	3	0.1	0.5	$0.5+(j-1)$	0.5	0.5	$0.5+(j-1)$	0.5
Fig. 6.3F	0	0.3	0.5	$0.5+2\cdot(j-1)$	0.5	0.5	$0.5+2\cdot(j-1)$	0.5
Fig. 6.3G	3	0	0.5	$0.5+2\cdot(j-1)$	0.5	0.5	$0.5+2\cdot(j-1)$	0.5
Fig. 6.3H	3	0.3	0	0	0	0.5	$0.5+2\cdot(j-1)$	0.5
			set $d=\tilde{d}$ directly					
Fig. 6.3I	3	0.3	0.5	$0.5+2\cdot(j-1)$	0.5	0	0	0
						set $\beta=\tilde{\beta}$ directly		
Fig. 6.3J	3	0.3	0.5	$0.5+2\cdot(j-1)$	0.5	0.5	$0.5+2\cdot(j-1)$	0.5

these techniques, the Bayesian-based BD, BFCD, and SIBF are selected for verifying the rationality of the optimization function designed in BDPK. The remaining methods qualitative and quantitative compared. The parameters involved in BDPK are initialized as follows: $j_{\max}=25$, $\eta=10^3$, and the remainder are set as described in Section III (Please note that the initialization of $\tilde{\beta}$ requires user intervention).

6.3.1 Relevance Test of Introduced Priors

In BDPK, three priori constraints are introduced for approximating the optimization function of haze removal. To check that all PDFs contained in BDPK can effectively be restrained to recover a realistic haze-free scene, we carry out the relevance test for BDPK by changing the regular parameters or redefining the PDF as a constant component. Fig. 6.3 shows the recovery results of BDPK with the different initialization states displayed in Table 6.3. Through comparison, we find the model constraint prior is particularly

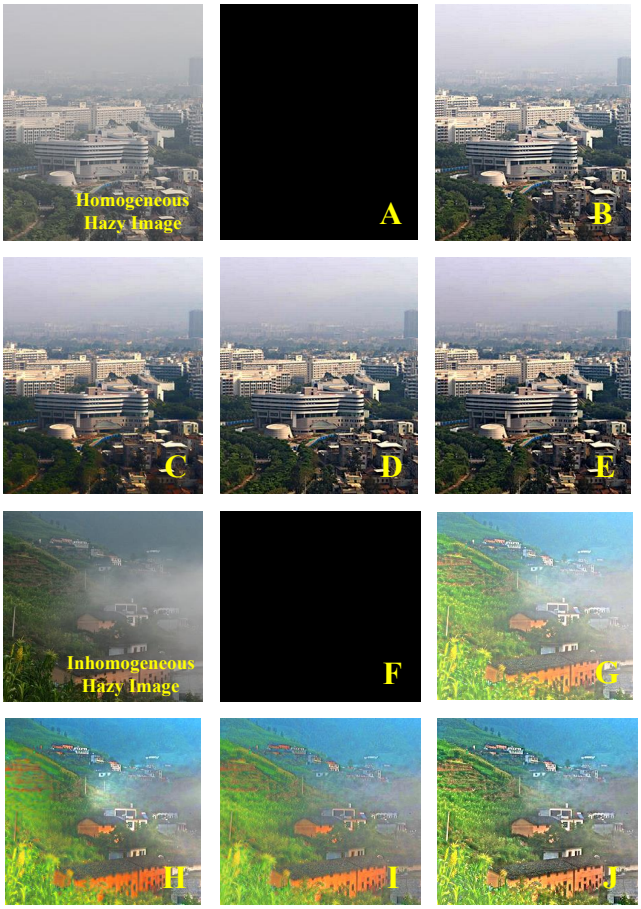

Figure 6.3: The relevance test with different initialization states listed in Table 6.3.

important for BDPK due to its influence on the constrained solution space. The contrast prior [39] is used to highlight the visual clarity of the vague image. The structure prior [71] imposes the scene depth and the scattering distribution has the efficacy to compensate for the interference of color distortion and remove the haze more thoroughly. It should be noted that although the structure prior used in BDPK is able to rectify the color distortion problem to a large extent (see Fig. 6.3G to 6.3J), the final result dehazed by BDPK shown in Fig. 6.3J still exhibits slight color shift. This is due to the fact that the incident light of each scene calculated via [71] would encounter estimation failure when the scene contains a bright target with large size. Meantime, the convolution operation

employed in formulas (Eq. 5.19, Eq. 5.20, and Eq. 5.21) might introduce some halo artifacts into depth discontinuities of recovery results, but this interference is visually negligible and does not deteriorate the recovery quality of BDPK.

6.3.2 Example Results Using BDPK

To validate the robustness of the proposed BDPK, several types of hazy images are selected from previous research [4,56] and we process them with our BDPK. The corresponding recovery results shown in Fig. 6.4 greatly reveal the scenic structures in vague regions and improve the global contrast of hazy inputs, regardless of homogeneous and inhomogeneous weather conditions. Furthermore, BDPK is also equipped with the illumination compensation capability (ICC) (see the last group example). We believe the above superior performance mainly benefits from the universality of Pb-ASM and the accuracy of the optimization function.

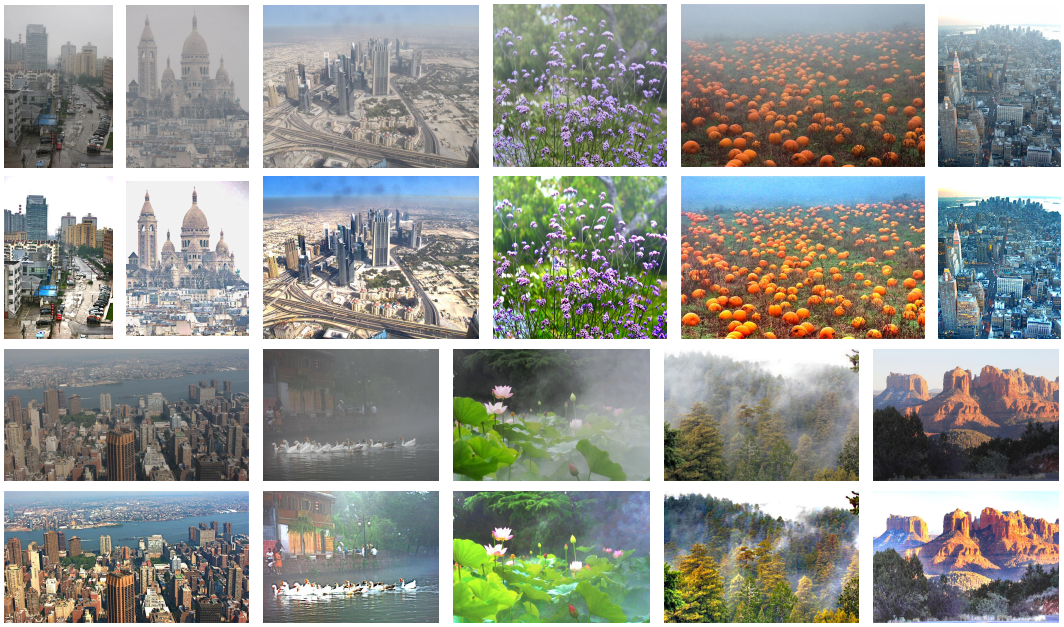

Figure 6.4: Image dehazing results using BDPK. **For each group**: the above is the hazy image and the bottom is the restored result by BDPK.

6.3.3 Qualitative Comparison with Bayesian-based Techniques

To our best knowledge, there are three Bayesian-based methods for single image haze removal. They are BD, BFCD, and SIBF. The posterior probabilities used in BD were built using the gradient distribution prior and spatial smooth prior to restore the scene albedo with the canonical expectation maximization algorithm. Based on BD, BFCD further considered the noise factor into the degradation model and employed the BM3D [104] as well as the probability density function of transmission to simultaneously remove the haze and noise. In SIBF , the minimization function for restoring the degraded images was constructed by imposing the sparse prior on both the recovery result and the transmission map. To prove that the BDPK has better properties than the existing Bayesian-based works, the comparison between these similar methods and BDPK is given in Fig. 6.5. Compared with the hazy image and the dehazed results (which are downloaded in [100]), the visual quality of each restored image shows different degrees of improvement, and all the methods can somewhat relieve the influence of haze. As shown in the first row in Fig. 6.5, BD can realize deep dehazing, but the over-enhancement often occurs in the fat areas that have slight textural details. In particular, the rocky areas in the recovered result are quite dark (see the yellow box). Likewise, due to the employed factorial Markov random fields [105], the halo artifact occurs in the red box. Similarly, BFCD suffers from over-saturation and produces much noise in the sky part (see the yellow box of the second row in Fig. 6.5). While SIBF rules out the interference of the above negative problems, the dehazing degree is visually weak (see the third row in Fig. 6.5). Conversely, BDPK's results have gentle sharpness and contrast, as well as the recovered color always looks very natural.

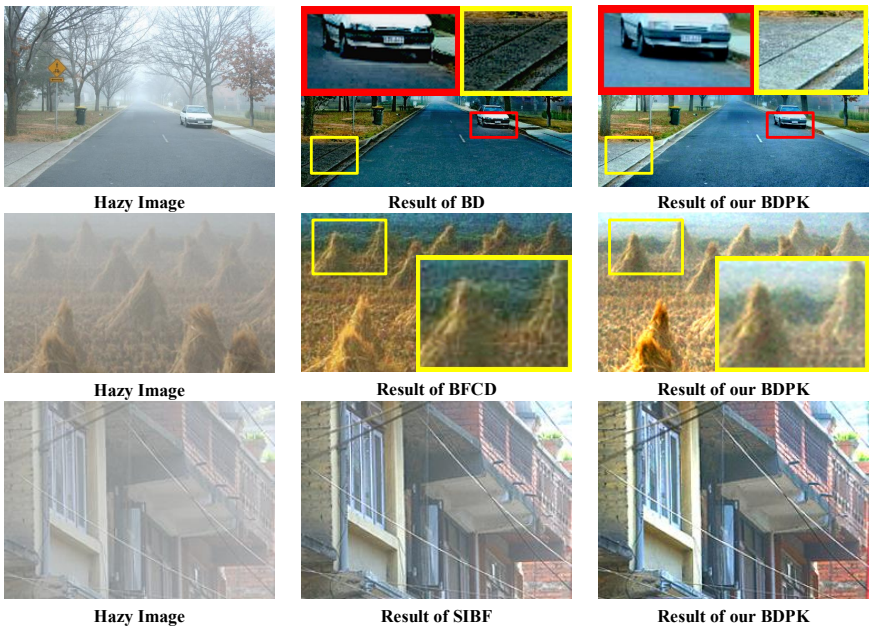

Figure 6.5: Comparison with the Bayesian-based works BD, BFCD, and SIBF.

6.3.4 Qualitative Comparison with Well-Known Techniques on Real-world Images

1) First Group: In Fig. 6.6, OCE, MCP, and MPE are processed with the two benchmark images. The reason that these methods were selected for comparison is that the recovery results are easily downloaded from Kim's websites. As we observed, OCE's results clearly show the object itself in the misty scene. However, since the control factor used in the cost function [55] is empirically set as a constant, the strength of the removed haze in the dense haze region is unstable compared to MCP, MPE and BDPK. For MCP, it can completely reveal the target contour for the given examples, yet the over enhancement was unfortunately introduced. Taking advantage of the given depth information, MPE successfully removes all the haze cover in the degenerated images. However, due to the constant atmospheric light defined in ASM, the visual clarity of recovered dark areas lacks competitiveness compared to BDPK (see the yellow box in the first row of Fig. 6.6).

Through comparison, our resumed images are more distinct and clear, have a stronger sense of stereovision, and can address all of the above unfavorable effects.

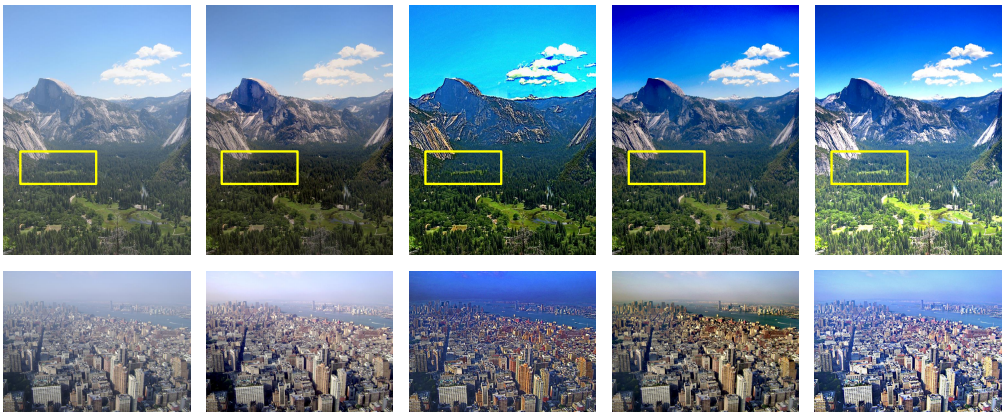

Figure 6.6: Comparison with well-known image restoration techniques. **From left to right**: Hazy images, OCE, MCP, MPE, BDPK.

2) Second Group: As is known, almost all the dehazing techniques are able to restore ideal results on general outdoor hazy images, it is very difficult to illustrate the superiority of the BDPK for restoration quality. Therefore, we focus on eight challenging real-world hazy images as the test samples of the second group, including the images with large gray scenes, misty haze, dense haze, uneven illumination and inhomogeneous atmosphere. Fig. 6.7 shows the qualitative comparison with six representative algorithms and BDPK on these challenging images. Fig. 6.7(a) depicts different types of hazy images to be dehazed, Figs. 6.7(b-h) show the restored results of FVR, DCP, SIIM, BCCR, CAP, DN, and BDPK, respectively. The recovery results corresponding to these representative methods shown in Fig. 6.7 are produced with the available MATLAB codes downloaded from the authors' websites in the MATLAB2010 environment on the same PC with Intel(R) Core(Tm) i5-4210U CPU @ 1.70GHz 8.00 GB RAM. This ensures the fair comparison.

As shown in Fig. 6.7(b), FVR recovers most of the scenic details and can be implemented in real time due to the linear complexity. However, FVR's results seriously suffer

from over-enhancement since the inherent problem of overestimating the transmission is inevitable (see the second image). Furthermore, owed to the median filter with poor edge preserving properties, the halo artifacts appear near the depth discontinuities (see the zoom-in patch of the fifth image). Although DCP has mostly promising results (see Fig. 6.7(c)), the color distortion still emerged in the sky regions (see the fourth image). This is since the accuracy of the estimated transmission mainly relies on the validity of DCP, which may be invalid when the scene's brightness is similar to the atmospheric light. For SIIM, this method could achieve impressive visual effects for most examples. However, its results might have adverse visual effects in dark regions with vague classification features (see the zoom-in patch of the fifth image in the Fig. 6.7 (d)). BCCR's results can fully eliminate the haze and unveil the scenic surface for all hazy targets. Regrettably, the dehazing results accompanied by over-saturation are bound to make the visual effect appear unrealistic. As we observe in Fig. 6.7(e), the rebuilt color in the sky region is significantly distorted, especially in the fourth and seventh images. In Fig. 6.7(f), although CAP avoids the halo artifacts and the over enhancement, the haze residual is obvious in the sixth image because simply regarding the scattering coef?cient as a fixed constant may not suitable for all situations. As displayed the first four images in Fig. 6.7(g), DN is capable of generating the restored results with vivid color and necessary details. Nevertheless, it does not work well for dense hazy images, as the corresponding results of ten appear shrouded by a small amount of haze (see the sixth image). The reason might be explained as follows. DehazeNet is designed only for transmission estimation and it lacks the contrast enhancement ability. On the other hand, the image pairs that are selected to train DehazeNet are artificially synthesized images rather than real-world images, which makes DehazeNet has a limited capability on dealing with real-world hazy images. Apart from the above-mentioned problems, these dehazing techniques still share two common limitations: 1) These methods (except for SIIM) lack the ICC and thus cannot appropri-

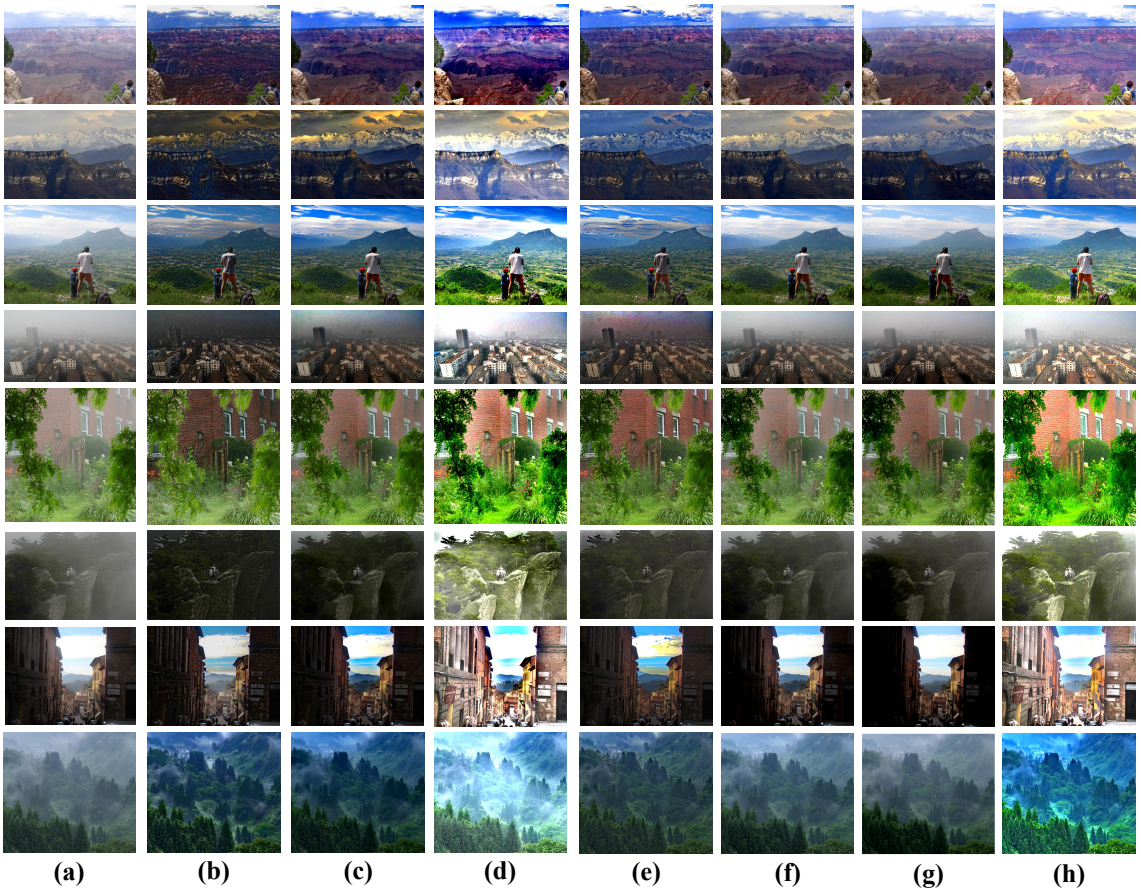

Figure 6.7: Experimental results of different methods on eight real-world hazy images. **(a)** Hazy Image. **(b)** FVR. **(c)** DCP. **(d)** SIIM. **(e)** BCCR. **(f)** CAP. **(g)** DN. **(h)** BDPK.

ately handle hazy images under uneven illumination (see the seventh row in Fig. 6.7) and 2) These methods may fail in the cases that the atmosphere is inhomogeneous (see the eighth row in Fig. 6.7). On the contrary, we notice that BDPK is completely unaffected by these limitations and can produce the realistic haze-free images while avoiding the halo artifacts, over-enhancement, over-saturation and the color distortion (see Fig. 6.7(h)).

6.3.5 Comparison with Well-Known Techniques on Synthetic Images

Assessing the recovery techniques for a single hazy image is a difficult task because the haze-free reference images could not be provided in the real-world. To verify the utility on complete images, the six representative techniques and BDPK are compared on the synthesized hazy images collected in the D-HAZY dataset [85], in which the corresponding ground truth reference images are known. In Fig. 6.8, we show the results processed with different methods on these synthesized images. Fig. 6.8(a) depicts the hazy images with names 'Piano', 'Couch', 'Jadeplant', 'Room', 'Shelves', 'Sticks', 'Bicycle' and 'Vintage'. Fig. 6.8 (b) provides the ground truth images for fair comparison. Figs. 6.8(c-i) exhibit the results of FVR, DCP, SIIM, BCCR, CAP, DN, and BDPK, respectively.

As seen in Fig. 6.8(c), FVR's results usually look much darker than the ground truth images, and the halo artifacts can be found in the depth discontinuities (see the jadeplant image). For DCP, as shown in Fig. 6.8(d), the recovered images achieve a good compromise between haze removal degree and target clarity. However, the ground of the bicycle image shows its inaccuracies. In Figs. 6.8(e,f), the results restored by BCCR and SIIM are visually compelling, yet the restored colors might be more over-saturated than they should be, especially in the sticks image. By observing Figs. 6.8(g,h), we notice that CAP and DN are very positive for the given misty examples, while their dehazed results for the other hazy images are still surrounded by a small amount of mist (see the playroom image and piano image). Different from these techniques, BDPK's results do not possess the unpleasing effects and they maintain the original tones of the scene targets. This further illustrates the outstanding performance of BDPK compared to these techniques in terms of the human visual perspective.

Figure 6.8: Experimental results of different methods on eight synthesized images. **(a)** Hazy Image. **(b)** Ground Truth. **(c)** FVR. **(d)** DCP. **(e)** SIIM. **(f)** BCCR. **(g)** CAP. **(h)** DN. **(i)** BDPK.

6.3.6 Complexity

The computational complexity is another critical assessment factor for the dehazing technique. Through analyzing, it can be inferred that the main computational overhead consumed in BDPK is the iteration module. Each iteration procedure mainly contains three convolution operations and other low-complex operations. Ignoring these simple calculations, for the given image with resolution res and the determined convolution kernel Λ, the theoretical complexity of BDPK is only $\mathrm{O}\left(res \cdot |\Lambda|\right) \cdot j_a$ ($|\Lambda|$ is the number of elements in Λ and j_a is the actual iteration number). Despite this, it may be more intuitive to see how many iterations are needed to empirically converge. Fig. 6.9(a) plots eight iteration

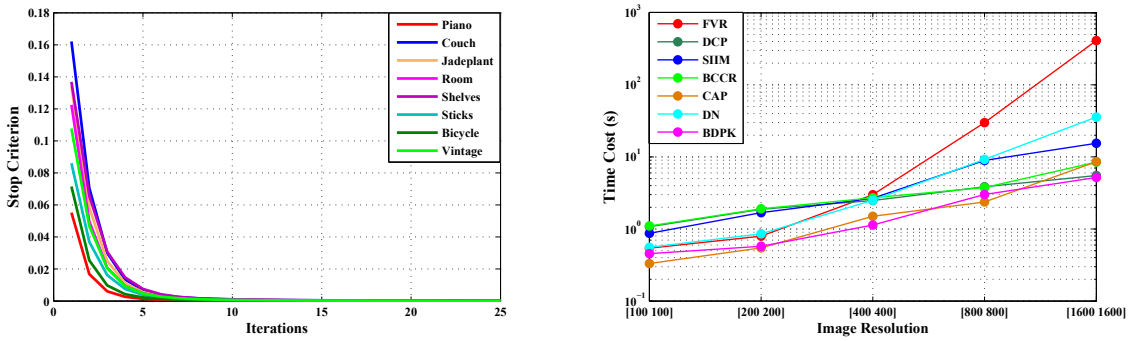

Figure 6.9: **(a)**: The convergence speed of the proposed BDPK in this work. The images used in this experiment are shown in Fig. 6.8. **(b)**: Time comparison of different techniques with varying image sizes.

curves for the images shown in Fig. 6.8. From these plots, we notice that the changing trends of the eight plots are similar to each other, and the actual iteration number is approximately 10 iterations for all tests. Fig. 6.9(b) gives the comparison between FVR, DCP, SIIM, BCCR, CAP, DN, and the proposed BDPK in terms of time costs (In the same PC described above, all the calculation times are recorded by running the authors' codes or the projects simulated by us on the hazy images with different resolutions). As we expected, the BDPK proposed in this work is much faster than FVR, DN, SIIM, DCP and BCCR, as well as is very close to the CAP with high efficiency. Even when the given hazy image is very large, BDPK still achieves high-speed processing.

6.4 Discussion and Conclusion

According to our previous Sb-ASM and the observation of atmospheric particles distribution, this chapter redefined a novel atmospheric scattering model (Pb-ASM) to overcome the issue of inhomogeneous haze. Afterwards, a single image dehazing algorithm called BDPK was further proposed based on this Pb-ASM. Unlike previous works, the

key contribution of BDPK is to convert the haze removal into an optimization function by combining Bayesian theory and prior knowledge. This allows us to directly restore the scene albedo using an alternating minimizing technique (AMT). Experimental results demonstrate the superiority of the proposed BDPK in terms of the dehazing effectiveness and the robustness compared with the state-of-the-art techniques.

Chapter 7

Remote Sensing Image Haze Removal Using Gamma-Correction-Based Dehazing Model

The main problems related to single image haze removal have been solved in previous chapters. This chapter focuses on fast remote sensing data (RS) restoration because RS images are more likely to be interfered by haze. In this chapter, a exponent-form ASM (Ef-ASM) with significantly enhanced robustness is introduced. Then, a scene albedo restoration formula (SARF) used for RGB-channel RS (RRS) images is derived by combining the existing priori constraint and this Ef-ASM. The propsoed SARF is able to simultaneously exclude the interferences of haze and non-uniform-illumination with less calculation load. Finally, according to Rayleigh's law, a proportional function of gamma variables corresponding to different wavelengths is established, which enables us to deduce an expansion restoration formula (E-SARF) for multi-spectral RS (MRS) data. With the proposed E-SARF, the haze in each band can be successfully removed regardless of uniform haze and non-uniform haze.

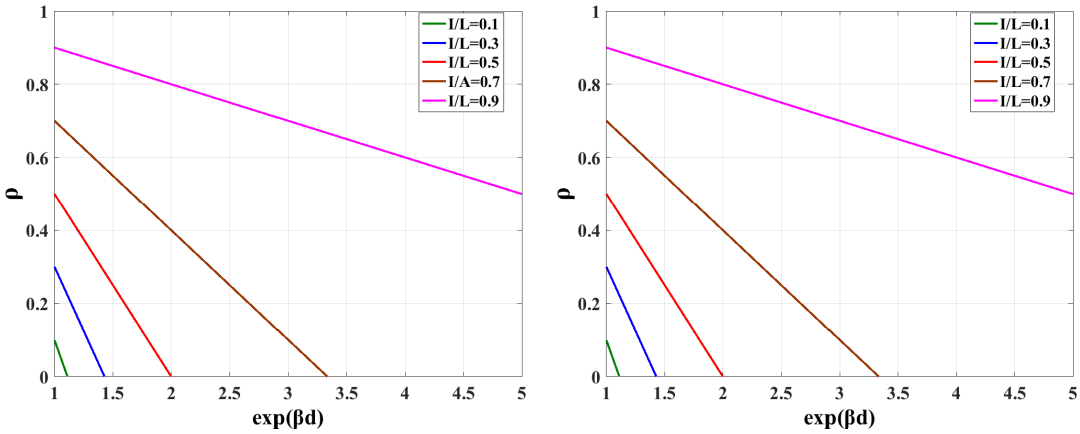

Figure 7.1: **Left**: Changing rate of the scene albedo corresponding to the ASM. **Right**: Changing rate of the scene albedo corresponding to Ef-ASM

7.1 Exponent-form ASM (Ef-ASM)

Chapter 3 analyzed that the failure reason for using gamma correction (GC) dehazing is attributed to the fixed coefficient Γ, that is to say a smaller scene depth leads to a stronger dehazing strength and vice versa. Following a simple derivation, the variable $\check{\Gamma}$ to ensure β can be written as

$$\check{\Gamma} = e^{\beta \cdot d(x,y)}, \tag{7.1}$$

where β and d are the scattering coefficient and scene depth, respectively. Referring to pervious Sb-ASM and Pb-ASM, uneven illumination problem can be addressed by dividing the scene incident light L into the corresponding color channels. Accordingly, a more concise exponent-form ASM (Ef-ASM) for haze removal is defined as

$$\boldsymbol{\rho} = \left(\frac{\boldsymbol{I}}{L}\right)^{\check{\Gamma}} = \left(\frac{\boldsymbol{I}}{L}\right)^{e^{\beta \cdot d}} \tag{7.2}$$

where Ef-ASM bridges the relationship between GC and traditional ASM. The benefit of using Ef-ASM is that it has a slower response of scene albedo with respect to its

independent variable compared to that of ASM [20], as shown in Fig. 7.1. This relieves the sharp change of pixel values in the edge-discontinuities regions, thus avoiding the halo/blocking artifacts.

7.2 Methodology

7.2.1 SARF for RRS Images

In this subsection, a scene albedo restoration formulae (SARF) is proposed for RGB-channel remote sensing (RRS) images. To simplify the subsequent refining process and address the non-uniform illumination problem, SARF is employed the Ef-ASM instead of Sb-ASM, Pb-ASM, or ASM to model RS data. In specific, following a simple derivation, Ef-ASM can be rewritten into

$$ln(\boldsymbol{\rho}(x,y)) = \check{\Gamma} \cdot (ln(\boldsymbol{I}(x,y)) - ln(L(x,y))) \tag{7.3}$$

Then, we assume that the ambient light of logarithmic domain $ln(L(x,y))$ and gamma variable $\check{\Gamma}$ in a local patch $\Omega(x,y)$ are both constant, and are denoted by $\widetilde{L}$ and $\widetilde{\Gamma}$, respectively. Taking the min operation and max operation on Eq. 7.3 yields

$$\begin{cases} dark(ln(\boldsymbol{\rho})) = \widetilde{\Gamma} \cdot dark(ln(\boldsymbol{I})) - \widetilde{\Gamma} \cdot \widetilde{L} \\ bright(ln(\boldsymbol{\rho})) = \widetilde{\Gamma} \cdot bright(ln(\boldsymbol{I})) - \widetilde{\Gamma} \cdot \widetilde{L}, \end{cases} \tag{7.4}$$

where

$$\begin{cases} dark(ln(\boldsymbol{\rho}(x,y))) \\ = \min\limits_{c\in\{R,G,B\}} (\min\limits_{(x',y')\in\Omega(x,y)} (ln(\rho^c(x',y')))) \\ dark(ln(\boldsymbol{I}(x,y))) \\ = \min\limits_{c\in\{R,G,B\}} (\min\limits_{(x',y')\in\Omega(x,y)} (ln(I^c(x',y')))) \\ bright(ln(\boldsymbol{\rho}(x,y))) \\ = \max\limits_{c\in\{R,G,B\}} (\max\limits_{(x',y')\in\Omega(x,y)} (ln(\rho^c(x',y')))) \\ bright(ln(\boldsymbol{I}(x,y))) \\ = \max\limits_{c\in\{R,G,B\}} (\max\limits_{(x',y')\in\Omega(x,y)} (ln(I^c(x',y')))) \end{cases} \tag{7.5}$$

Since $ln(\cdot)$ is monotonically increasing function, Eq. set 7.5 is equivalent to

$$\begin{cases} dark(ln(\boldsymbol{\rho}(x,y))) = ln(dark(\boldsymbol{\rho}(x,y))) \\ = ln(\min\limits_{c\in\{R,G,B\}}(\min\limits_{(x',y')\in\Omega(x,y)}(\rho^c(x',y')))) \\ dark(ln(\boldsymbol{I}(x,y))) = ln(dark(\boldsymbol{I}(x,y))) \\ = ln(\min\limits_{c\in\{R,G,B\}}(\min\limits_{(x',y')\in\Omega(x,y)}(I^c(x',y')))) \\ bright(ln(\boldsymbol{\rho}(x,y))) = ln(bright(\boldsymbol{\rho}(x,y))) \\ = ln(\max\limits_{c\in\{R,G,B\}}(\max\limits_{(x',y')\in\Omega(x,y)}(\rho^c(x',y')))) \\ bright(ln(\boldsymbol{I}(x,y))) = ln(bright(\boldsymbol{I}(x,y))) \\ = ln(\max\limits_{c\in\{R,G,B\}}(\max\limits_{(x',y')\in\Omega(x,y)}(I^c(x',y')))) \end{cases} \tag{7.6}$$

Bright channel prior (BCP) [106] and translational dark channel prior (TDCP) [107] are the statistics of high-quality images that is based on the key observation that – in most local patches in such images, at least one color channel exists pixels with high intensity close to one and with low intensity close to C. Formally, they can be described as

$$\begin{cases} bright(\boldsymbol{\rho}(x,y)) = \max\limits_{c\in\{R,G,B\}}(\max\limits_{(x',y')\in\Omega(x,y)}(\rho^c(x',y'))) \to 1 \\ dark(\boldsymbol{\rho}(x,y)) = \min\limits_{c\in\{R,G,B\}}(\min\limits_{(x',y')\in\Omega(x,y)}(\rho^c(x',y'))) \to C. \end{cases} \tag{7.7}$$

Accordingly, combining Eq. sets 7.4, 7.5, 7.6, the gamma variable and ambient light are computed as

$$\begin{cases} \check{\Gamma} \approx \widetilde{\Gamma} = \frac{ln(C)}{ln(dark(\boldsymbol{I}))-ln(bright(\boldsymbol{I}))} \\ L \approx e^{\widetilde{L}} = bright(\boldsymbol{I}) \end{cases} \tag{7.8}$$

Substituting Eq. set 7.8 into Eq. 7.3, the scene albedo can be easily restored by

$$\boldsymbol{\rho} = (\frac{\boldsymbol{I}}{bright(\boldsymbol{I})})^{\frac{ln(C)}{ln(dark(\boldsymbol{I}))-ln(bright(\boldsymbol{1}))}} \tag{7.9}$$

Note that the min and max operations are both based on the local-constant assumption, some block effects might appear in the $dark(I)$ and $bright(I)$. Thanks to the less sensitive feature of scene albedo in Ef-ASM, we are able to use a mean filter with low complexity to relieve the block effects. Therefore, the SARF for RRS images is derived as

$$\boldsymbol{\rho} = (\frac{\boldsymbol{I}}{mean(bright(\boldsymbol{I}))})^{\frac{ln(C)}{ln(mean(dark(\boldsymbol{I})))-ln(mean(bright(\boldsymbol{I})))}} \tag{7.10}$$

where $mean(\cdot)$ represents the mean filter operator.

7.2.2 Expansion of SARF for MRS data

To achieve haze removal for multi-spectral remote sensing (MRS) data, an expansion strategy for SARF is further proposed. Intuitively, we firstly normalize the input MRS image $\boldsymbol{I}_{MRS} = \boldsymbol{I'}_{MRS}/2^b \in [0,1]$ ($\boldsymbol{I'}_{MRS}$ is the original MRS data and b is the bit depth of pixels contained in $\boldsymbol{I'}_{MRS}$). Then, adopting the derivation process similar to that of SARF, gamma variable $\check{\Gamma}_{MRS}$, ambient light L_{MRS} and scene albedo ρ^j_{MRS} of j^{th} band in $\boldsymbol{I}_{MRS}$ can be derived as

$$\begin{cases} \check{\Gamma}_{MRS} \approx \frac{ln(C)}{ln(mean(dark(\boldsymbol{I}_{MRS})))-ln(mean(bright(\boldsymbol{I}_{MRS})))} \\ L_{MRS} \approx mean(bright(\boldsymbol{I}_{MRS})) \\ \rho^j_{MRS} = (\frac{\boldsymbol{I}^j_{MRS}}{L_{MRS}})^{\check{\Gamma}_{MRS}} \end{cases} \tag{7.11}$$

where $\boldsymbol{I}^j_{MRS}$ is the j^{th} band in $\boldsymbol{I}_{MRS}$, $dark(\boldsymbol{I}_{MRS})$ and $bright(\boldsymbol{I}_{MRS})$ are computed via

$$\begin{cases} dark(\boldsymbol{I}_{MRS}(x,y)) = \\ \min\limits_{j\in\{1,2,\ldots,n\}}(\min\limits_{(x',y')\in\Omega(x,y)}(I^j_{MRS}(x',y'))) \\ bright(\boldsymbol{I}_{MRS}(x,y)) = \\ \max\limits_{j\in\{1,2,\ldots,n\}}(\max\limits_{(x',y')\in\Omega(x,y)}(I^j_{MRS}(x',y'))) \end{cases} \tag{7.12}$$

Since Landsat 8 OLI data ate freely available in website [https://earthexplorer.usgs.gov], thus the experiment for MRS images haze removal is based on the collected Landsat 8 OLI data (its band information is listed in Table 7.1). Please note that the band 9 in Landsat 8 OLI image is used for detecting cloud distribution, it does not record the real information of earth surface. Therefore, in this work, haze removal is only performed in the remaining eight bands. Fig. 7.2 gives a recovery result via Eq. 7.11 on a hazy Landsat 8 OLI image. As can be seen, although the texture details of bands 5, 6, 7 have been enhanced markedly, the recovery scenes of bands 1, 2, 3, 4, 8 still exist the haze residue phenomenon, especially in the true color combined by bands 4, 3, 2. This is because the influence of haze is reduced gradually with the wavelength increasing, which implies these bands with different wavelengths should adopt the different gamma variables to exclude

the interference of haze. To solve this issue, a repair mechanism for Eq. 7.11 is provided. First, based on the proposed Ef-ASM, the gamma variable $\check{\Gamma}^{j}_{MRS}$ of j^{th} band in a MRS image I_{MRS} is defined as

$$\check{\Gamma}^{j}_{MRS} = e^{\beta^{j}_{MRS} \cdot d_{MRS}} \tag{7.13}$$

where β^{j}_{MRS} is scattering coefficient of j^{th} band, and d_{MRS} is scene depth of $\boldsymbol{I}_{MRS}$. Taking logarithm operation of each side in Eq. 7.13 yields

$$ln(\check{\Gamma}^{j}_{MRS}) = \beta^{j}_{MRS} \cdot d_{MRS} \tag{7.14}$$

According to Rayleigh's law [19, 20], the relationship between the scattering coefficient and the wavelength is expressed as

$$\beta^{j}_{MRS} \propto \frac{1}{(\lambda^{j}_{MRS})^{\gamma}} \tag{7.15}$$

where $\gamma \in [0, 4]$ depending on the particle size suspended in the atmosphere, λ^{j}_{MRS} is the center wavelength of band j. Substituting Eq. 7.15 into Eq. 7.14, we can get

$$ln(\check{\Gamma}^{j}_{MRS}) \propto \frac{1}{(\lambda^{j}_{MRS})^{\gamma}} \cdot d_{MRS} \tag{7.16}$$

Then, the relationship of $ln(\check{\Gamma}_{MRS})$ between any two bands j_1, j_2 in MRS image $\boldsymbol{I}_{MRS}$ can be described as

$$\begin{gathered} \frac{ln(\check{\Gamma}^{j_1}_{MRS})}{ln(\check{\Gamma}^{j_2}_{MRS})} = (\frac{\lambda^{j_2}_{MRS}}{\lambda^{j_1}_{MRS}})^{\gamma} \Rightarrow \check{\Gamma}^{j_1}_{MRS} = e^{(\frac{\lambda^{j_2}_{MRS}}{\lambda^{j_1}_{MRS}})^{\gamma} \cdot ln(\check{\Gamma}^{j_2}_{M\_RS})} \\ j_1 \; and \; j_2 \in \{1, 2, ..., n\} \end{gathered} \tag{7.17}$$

where $\check{\Gamma}^{j_1}_{MRS}$, $\lambda^{j_1}_{MRS}$ and $\check{\Gamma}^{j_2}_{MRS}$, $\lambda^{j_2}_{MRS}$ are the gamma variables and wavelengths of band j_1 and band j_2, respectively. Once the gamma variable of any one band has been determined, the gamma variables of remaining bands can be accurately calculated via Eq. 7.17. In Eq. 7.11, gamma variable $\check{\Gamma}_{MRS}$ is computed from all the bands contained in MRS images.

Table 7.1: Spectral Bands and the corresponding wavelengths of Landsat 8 OLI with 12-bit radiometric resolution (μm).

Spectral Band	Wavelength Range	Center Wavelength
Band1–Coastal	0.433-0.453	0.443
Band2–Blue	0.450-0.515	0.4825
Band3–Green	0.525-0.600	0.5625
Band4–Red	0.630-0.680	0.655
Band5–Iear Infrared	0.845-0.885	0.865
Band6–Short Wavelength Infrared	1.560-1.660	1.61
Band7–Short Wavelength Infrared	2.100-2.300	2.2
Band8–Panchromatic	0.500-0.680	0.59
Band9–Cirrus	1.360-1.390	1.375

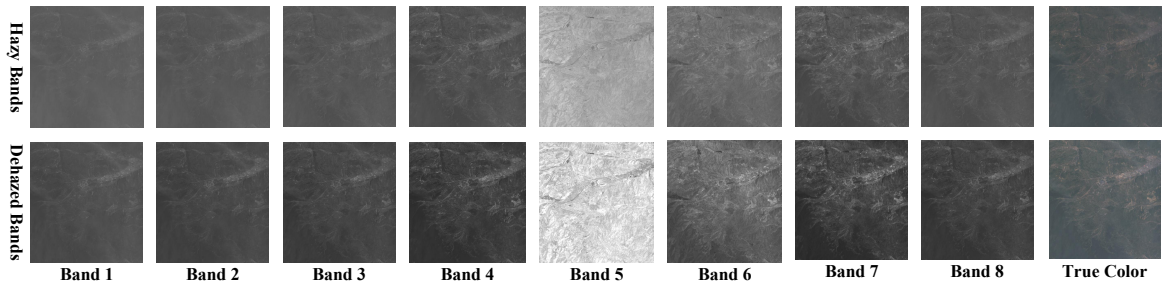

Figure 7.2: Limitation of setting same transmission for all bands in MRS data (True color is combined by bands 4, 3, 2).

Based on this fact, here we assume that the wavelength $\overline{\lambda}^{M}_{MRS}$ matching to $\check{\Gamma}_{MRS}$ equals the average value of all the bands' center wavelengths. Accordingly, Eq. 7.17 can be transformed as

$$\check{\Gamma}^{j}_{MRS} = e^{(\frac{\overline{\lambda}^{M}_{MRS}}{\lambda^{j}_{MRS}})^{\gamma} \cdot ln(\check{\Gamma}_{MRS})} \qquad j \in \{1, 2, ..., n\} \tag{7.18}$$

Combining Eq. 7.11 and Eq. 7.18, the expanded recovery formula (E-SARF) for MRS data is proposed as

$$\rho^{j}_{MRS} = (\frac{\boldsymbol{I}^{j}_{MRS}}{L_{MRS}})^{e^{(\frac{\overline{\lambda}^{M}_{MRS}}{\lambda^{j}_{MRS}})^{\gamma} \cdot ln(\check{\Gamma}_{MRS})}} \qquad j \in \{1, 2, ..., n\} \tag{7.19}$$

where γ is set according to [108].

7.3 Experimental Results

In this section, the performance analysis of different parameters used in proposed SARF and E-SARF was first illustrated experimentally, and then comparisons between the proposed methods (SARF and E-SARF) and other well-known techniques were conducted from both qualitative and quantitative perspectives to assess the performance. Experiments were implemented by MATLAB2010 on a PC with Intel(R) Core(Tm) i5-4210UCPU@ 1.70GHz 8.00 GB RAM. In our experiments, the hazy RRS images were downloaded from Google Earth or other satellite sources, and the MRS data were collected in website [https://earthexplorer.usgs.gov].

7.3.1 Parameter Analysis

In the proposed SARF and E-SARF, the patch size of DCP S_1, the patch size of BCP S_2, and the mean filter size S_3 need to be initialized manually. To investigate that how the parameters affect the dehazing performance, we conducted recovery quality test for SARF and E-SARF by adjusting these corresponding parameters. Fig. 7.3(a) shows the results restored via SARF on a RRS image with different patch sizes S_1 and S_2. It can be concluded from this figure that a smaller patch size leads to stronger haze removal ability and more adequate light compensation. However, too small patch size also arouses the adverse over-enhanced and over-saturated in processing results. Through comparison, the dehazed result using patch sizes $S_1 = S_2 = 15$ obtains the best visual quality. Fig. 7.3(b) illustrates the influences of filter size S_3 on dehazing performance. As can be seen, too small filter size would result in the over-saturated in yellow rocks, while too large size can not completely uncover the scene contents in the region with

dense haze. In contrast, the recovery result using filter size $S_3 = 65$ is able to achieve a better balance in terms of visual quality. The above conclusion is also suitable to E-SARF, and the corresponding experimental results can be found in author's homepage: https://www.researchgate.net/profile/Mingye_Ju. According to the above analysis, the patch sizes of DCP and BCP were set as $S_1 = S_2 = 15$, and the mean filter size S_3 was initialized as 65 in following experiments.

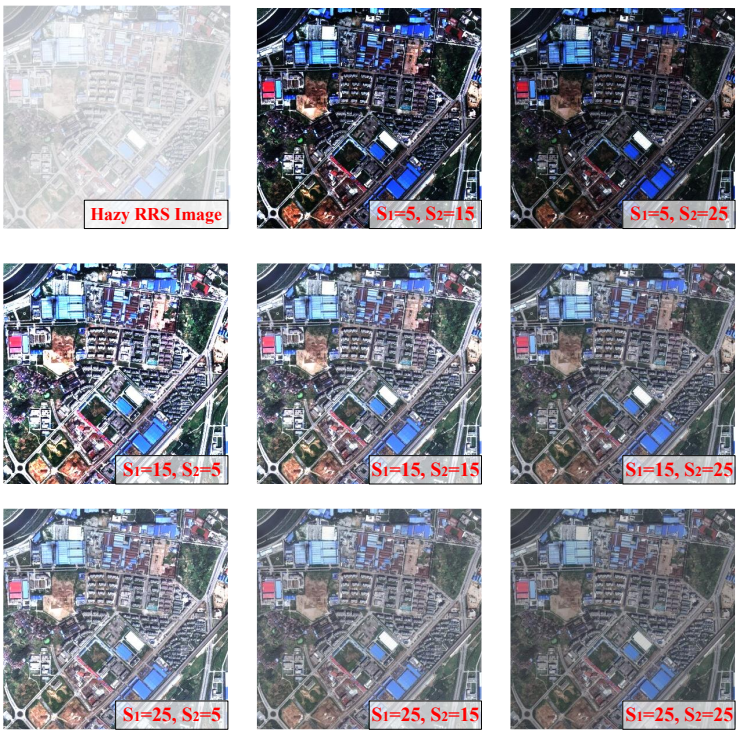

(a) Performance influence of the different patch sizes of DCP and BCP

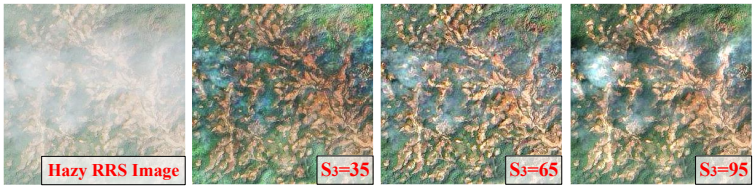

(b) Performance influence of the different sizes of mean filter

Figure 7.3: Performance Analysis of different parameters used in SARF.

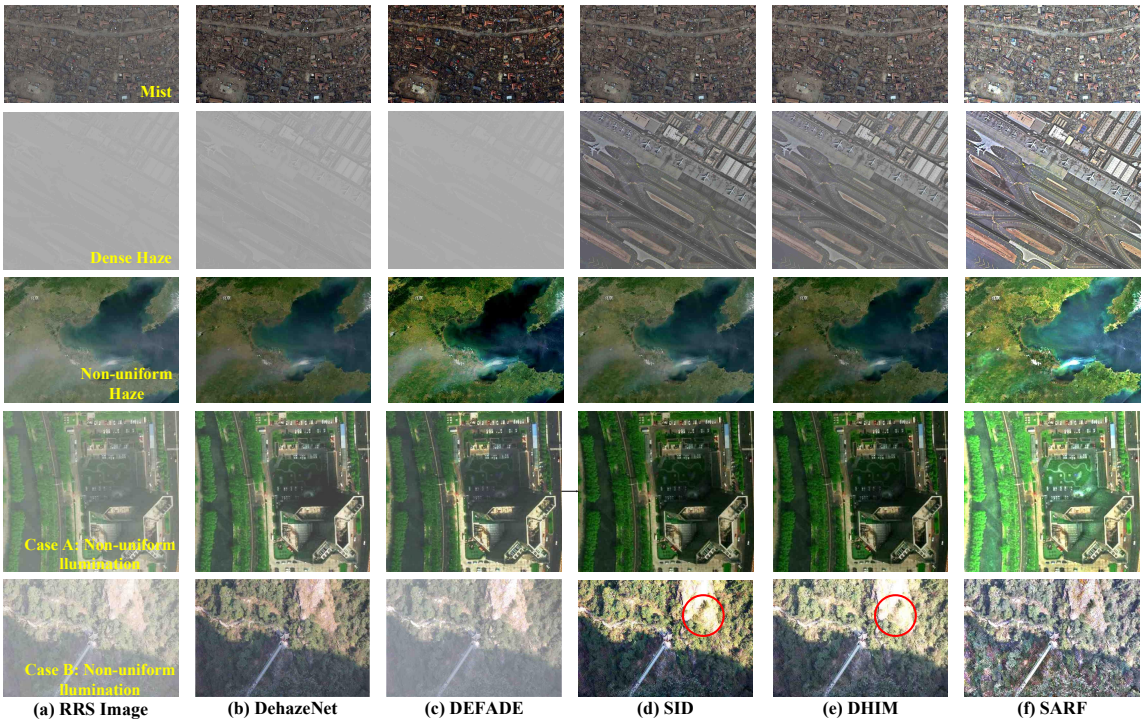

Figure 7.4: Qualitative comparison between state-of-art RRS image dehazing techniques and the proposed SARF.

7.3.2 Comparison between State-of-the-art Techniques and SAR-F on RRS Images

7.3.2.1 Qualitative Comparison

Being able to handle hazy RRS images with complex environment, for example, heavy haze, non-uniform haze and non-uniform illumination, is also compulsory but challenging for dehazing techniques. Therefore, five challenging RRS images are picked for facilitating the comparison between SARF and the sate-of-the-art methods, as shown in Fig. 7.4(a). Figs. 7.4(b∼f) give the results dehazed via DehazeNet [85], DEFADE [34], SID [109], DHIM [107], and the proposed SARF.

As we observed in Figs. 7.4(b,c), DehazeNet and DEFADE mainly used for convention-

al hazy outdoor images lack any competitiveness compared to the remaining specialized approaches that used for RRS images, their dehazing results for given RRS images always suffer from over-saturated or haze residue problem. The main reason can be attributed to the prior knowledge or the haze features used in DehazeNet and DEFADE are discovered from hazy outdoor images rather than those of RRS images. In Figs. 7.4(d,e), due to inaccurate estimation of atmospheric light, the dehazed images via SID and DHIM unfortunately lead into over-saturated in bright regions, thus the original information in the corresponding scenes is lost (see the red circles). Morevoer, SID cannot handle the non-uniform haze situation well. The part with thick haze in the recovered results is still surrounded by some mist. Apart from the aforementioned problems, these techniques all lack the light compensation ability for shadow scene, the texture details in the recovered low-illumination regions still appear quite blurry (see the last two examples). Different from these methods, SARF is free from the above negative interferences, and can reveal richer target contours regardless whether the haze and illumination are non-uniform or uniform.

7.3.2.2 Quantitative comparison

To avoid the subjective bias of the above quality comparison, the dehazed results are also assessed quantitatively. In this work, three widely-recognized non-reference indexes, namely fog aware density evaluator (FADE) [34], mean ratio of the gradients at visible edge ($\bar{r}$) [86], and new visible edge ratio (e) [86] were employed to quantitatively evaluate the proposed method and other techniques. In general, the lower FADE indicates the stronger dehazing ability, the greater $\bar{r}$ and e indicate the richer information contained in the recovery results. The state-of-art techniques and the proposed SARF are assessed by these indexes on dealing with the hazy images shown in Fig. 7.4. The values of the assessment indexes are summarized in Table 7.2. It can be concluded from the table

Table 7.2: Quantitative comparison between state-of-art techniques and the proposed SARF on RRS images shown in Fig. 7.4

Examples	Metric	DehazeNet	DEFADE	SID	DHIM	SARF
Mist	e	-0.098	-0.1842	-0.0347	0.0065	**0.0314**
	$\bar{r}$	1.0984	1.3105	1.0115	1.0944	**1.6131**
	FADE	0.1841	**0.0786**	0.1952	0.1899	0.2909
Dense Haze	e	-0.0996	0.0209	4.5629	4.4178	**4.8252**
	$\bar{r}$	1.2052	1.0081	8.6074	8.3976	**14.6976**
	FADE	5.1999	7.8503	0.8298	0.9745	**0.3854**
Non-uniform Haze	e	0.1386	0.1481	0.0886	0.1657	**0.2817**
	$\bar{r}$	1.0326	1.716	1.6766	1.7185	**2.4215**
	FADE	**0.2366**	0.2954	0.2862	0.2493	0.364
Case A	e	0.3309	0.2875	0.2275	0.2475	**0.335**
	$\bar{r}$	1.6654	1.6517	1.2067	1.1971	**2.5002**
	FADE	0.6929	0.7141	0.4543	0.3908	**0.2412**
Case B	e	0.0257	-0.1942	0.0734	0.0657	**0.1614**
	$\bar{r}$	1.636	2.9961	1.5414	1.7398	**1.7511**
	FADE	0.4865	1.0688	0.3551	0.3315	**0.3186**

that the proposed SARF has the highest values of $\bar{r}$ and e for all the given examples, which validates that SARF removes the haze more completely and uncovers clearer scenes. However, for the first and third examples in Fig. 7.4, the FADE's values of SARF are larger than others. This is due to the fact that the results restored by SARF have brighter scene contents, which is misidentified as haze by FADE. Moreover, another significant advantage of the proposed SARF is its high efficiency and real-time performance. SARF only contains the simple min, max, and mean filters, and these operations can be further accelerated via box filter [29]. Thus the theoretical complexity of SARF is only $\mathcal{O}(m, n)$ where m and n are image high and width, respectively. Table 7.3 further summarized the time cost on dehazing the first image in Fig. 7.4 with different resolutions by different dehazing techniques as an example. It is demonstrated that SARF exhibits a significantly faster calculation time compared to other techniques.

Table 7.3: Processing time of state-of-art techniques and SARF on RRS images with different resolution (s)

Image Size	DehazeNet	DEFADE	SID	DHIM	SARF
189×385	1.9263	18.3517	1.1423	1.3880	**0.1626**
378×769	7.2718	59.3939	1.3637	1.7931	**0.3622**
576×1153	13.2079	159.0901	1.5603	2.1864	**0.6662**
756×1538	23.8423	227.5452	1.9924	3.1024	**1.2053**
945×1922	34.5520	334.3812	2.2588	4.2121	**1.9233**
1890×3844	110.6243	1153.5121	2.7327	9.9121	**2.5233**

7.3.3 Comparison between State-of-the-art Techniques and E-SARF on MRS Data

7.3.3.1 Qualitative Comparison

To check the utility of E-SARF proposed in this paper, we compare it with three dehazing algorithms used for MRS images, including IMCR [110], P-DCP [111] and HR [2]. Fig. 7.5 shows the experimental instances on the hazy Landsat 8 OLI images using the proposed E-SARF and three compared techniques. In each case of Fig. 7.5, the first row is the MRS image, and the remaining four rows are the dehazing results of IMCR, P-DCP, HR and E-SARF, respectively.

By observing these comparison results in Fig. 7.5(b), it can be noticed that IMCR is able to uncover the reasonable texture details for most bands, but it cannot deal with the scenes with non-uniform haze (see case B). In Fig. 7.5(c), the results produced via P-DCP always emerge adverse spectral distortions or mist residue in its dehazed bands. This is because P-DCP sets the transmission maps of all bands as same component, thus neglects the effect of wavelength on haze interference. Moreover, P-DCP also lacks the ability to handle the case with non-uniform haze (see case B). Although HR is capable of eliminating the haze and unveil the scenic surface for given examples, the too dim

restored textures are bound to make the visual effect appear unrealistic (see Fig. 7.5(d)). In contrast, E-SARF's results have gentle sharpness and contrast for each band, as well as the hue in recovered true color combined by bands 4, 3, 2 always looks very nature.

Table 7.4: Quantitative comparison between state-of-art techniques and the proposed E-SARF on MRS images shown in Fig. 7.5

Examples	Metric	IMCR	P-DCP	HR	E-SARF
Case A	e	2.0722	1.3471	1.5241	**2.1457**
	$\bar{r}$	3.5945	1.2701	1.3371	**3.7323**
	FADE	0.6545	0.9642	**0.4749**	0.5922
Case B	e	2.3217	2.0233	2.2035	**2.7209**
	$\bar{r}$	3.4048	1.475	1.5555	**3.5441**
	FADE	0.7519	1.2105	**0.5451**	0.6832

Table 7.5: Processing time of state-of-art techniques and E-SARF on MRS images with different resolution (s)

Image Size	IMCR	P-DCP	HR	E-SARF
935×879×9	8.6728	3.3135	2.257	**1.834**
1870×1757×9	35.9198	6.2983	5.799	**3.4701**
2805×2636×9	105.4598	13.474	8.8706	**6.2077**
3740×3514×9	252.7485	29.7514	18.0837	**16.5727**
4675×4393×9	538.1793	70.8266	40.7123	**35.3377**

7.3.3.2 Quantitative comparison

Using the three aforementioned non-reference metrics, namely FADE, $\bar{r}$, and e, as the test criteria for quantitatively evaluating these dehazing algorithms for MRS data. The quantitative scores of these metrics corresponding to the recovered results in Fig. 7.5 are depicted in Table 7.4. Please note that values of $\bar{r}$ and e listed in Table 7.4 are the mean of assessed value of all the dehazed bands, and FADE's values were calculated from the true colors combined by bands 4, 3, 2. Analyzing these data, it can be found that the scores of $\bar{r}$ and e of E-SARF outperform the the remaining methods in the given

experimental examples, which fully proves that the proposed E-SARF can gain the richer scene textures. However, as we discussed in above, FADE mistakenly judges the brighter scenes caused by light compensation ability as the dense haze ones, which leads to FADE's values of the proposed E-SARF are larger than those of HR. The running times of the three comparison algorithms and E-SARF on the first example (with different resolutions) shown in Fig. 7.5 are listed in Table 7.5. As we expected, E-SARF proposed in this work is much faster than IMCR and P-DCP, as well as is slightly faster than the HR with high efficiency.

7.4 Conclusion

In this chapter, a robust exponent-form ASM (Ef-ASM) is proposed to describe the images degraded by haze, fog, and shadow. Combining this Ef-ASM and the existing prior knowledge, a scene albedo restoration formula (SARF) for RGB-channel remote sensing (RRS) images is derived. Then, an expansion restoration formula (E-SARF) for multi-spectral remote sensing (MRS) data is further provided according to Rayleigh's law. Qualitative and quantitative comparisons between the proposed methods (SARF and E-SARF) and other state-of-arts techniques are conducted. It is demonstrated that the proposed methods not only thoroughly removes the haze or fog in such images, but also effectively excludes the interference of non-uniform illumination. More importantly, SARF and E-SARF perform much faster than other comparable dehazing techniques which makes them the excellent candidates for real-time applications.

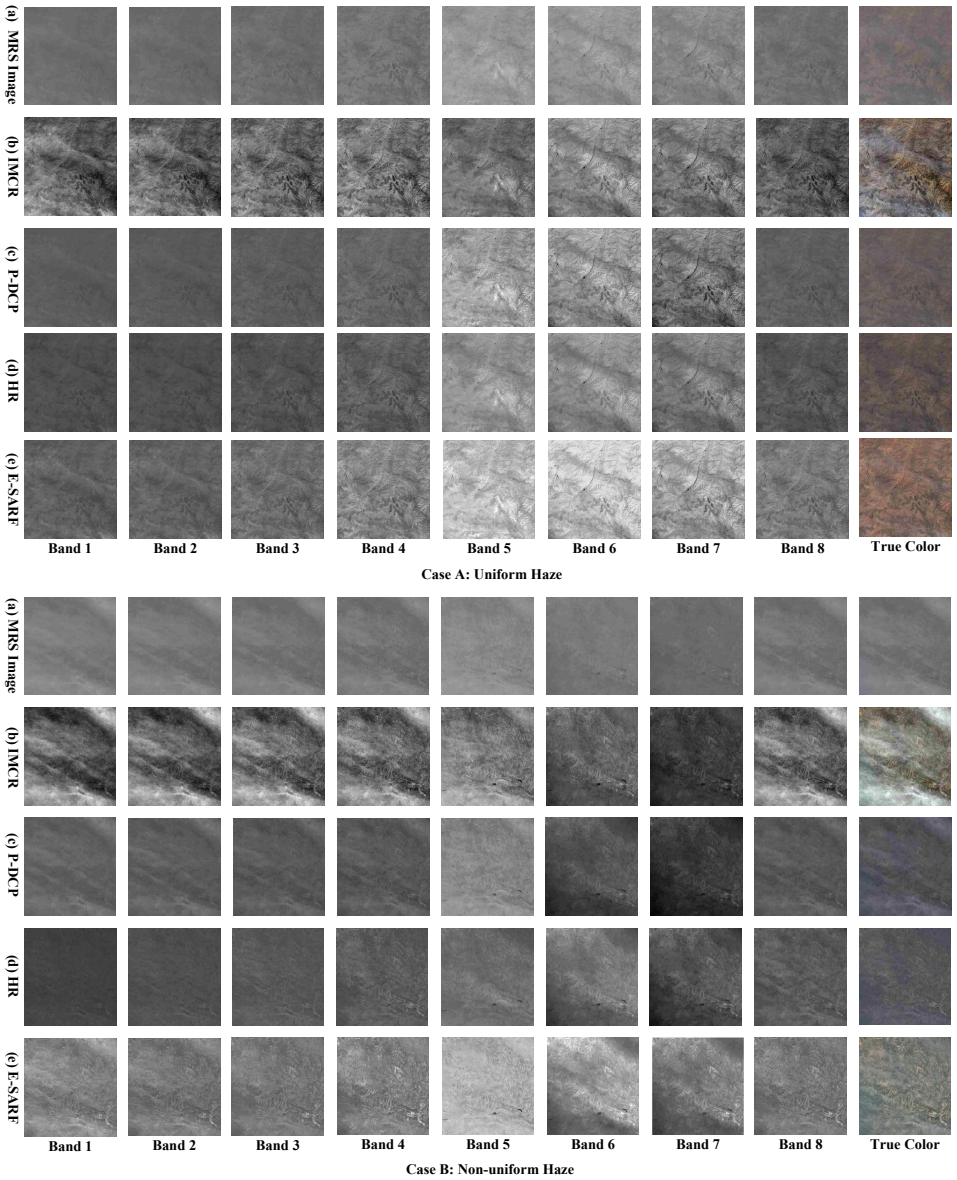

Figure 7.5: Qualitative comparison between state-of-art MRS image dehazing techniques and the proposed E-SARF.

Chapter 8

Conclusions and Future Work

8.1 Conclusions

This dissertation focuses on exploring a high efficiency and strong robust single image haze removal technique to meet the demands of outdoor vision systems that need high-quality input. Initially, formation mechanism of hazy image and atmospheric scattering model (ASM) used in computer vision are briefly illustrated. Through in-depth study of the state-of-the-art methods, three challenging yet promising issues related to image dehazing are summarized, i.e., low robustness, low real-time performance, and failure on images with inhomogeneous haze image and uneven illumination. Motivated by this, five simple and effective visibility recovery techniques are presented to fully bridges the research gap on the above problems. The main contributions in this include the following five aspects:

1. For efficiency, based on the proposed gamma correction prior, IDGCP (ASM-based) converts single image dehazing problem into multiple images haze removal one. The benefit is to ease the uncertainty of depth information, so that the haze removal task can be redefined as a global-wise optimization function to determine only one unknown

constant. Furthermore, IDGCP is able to obtain high-quality transmission map without any time-consuming refining process, which further reduces the processing time.

2. Another technique for accelerating dehazing (VROHI) is to make full use of imaging model used in remote sensing data restoration, i.e., additive haze model (AHM), to simulate the hazy image. In specific, by combining the low-frequency feature of hazy image and the saturation prior, VROHI only needs to determine two unknown constants rather than estimating the highly uncertain transmission to achieve a haze-free result, thereby significantly increasing the execution efficiency of haze removal.

3. To solve the uneven illumination issue, Sb-ASM-based IDSL firstly attempts to redefine the atmospheric light in imaging model as scene incident light to better model the hazy scenes. Meanwhile, IDSL simplifies the imaging parameter estimation process by constructing a lineal model for modeling the transmission, thus it is able to remove the haze from hazy images with low computational overhead.

4. To solve the inhomogeneous haze issue, Pb-ASM-based BDPK is proposed to by transforming the single image dehazing problem into a maximum a-posteriori probability (MAP) one. In this method, we employed the low complexity alternating minimizing technique to solve this MAP, which ensures the processing speed of haze removal. Thanks to the powerful Bayesian theory, BDPK is capable of producing a high-quality recovery result on inhomogeneous-haze images by merging the advantage of some multi-priors.

5. To achieve high efficiency dehazing for remote sensing (RS) data, SARF is proposed according to an exponent-form ASM (EASM) which is modified according to equivalence infinitesimal theorem. The key advantage of SARF is that its low complexity and it can simultaneously eliminate the interferences of haze and non-uniform illumination for RS images. More importantly, according to Rayleighąś law, SARF can be expanded to achieve haze removal for multi-spectral RS (MRS) data. Using the expanded SARF (E-SARF), the spatially varying haze in each band can be thoroughly removed without

using any extra information.

8.2 Future Work

Although several advanced single image dehazing approaches have been developed in this dissertation, there are still some interesting work that should be done on in the future:

1. In Chapter 4, VROHI was developed to achieve ultra-high efficiency while maintaining good restoration quality for most scenes. Previous experimental results show that this goal has been well achieved. However, VROHI also has a drawback, i.e., it lacks the ability to deal with images captured in night with low light intensity. This is because VROHI employs the atmospheric light correction (ALC) to enhance the visual quality, which is suitable for day-time images illuminated by natural light. However, in night-time images, the light usually come from a point source, thus ALC is not suitable. Moreover, the saturation prior employed in VROHI was summarized from the statistics of thousands of daytime images, thus cannot be directly used for night-time images. In the future, VROHI needs to be further improved to better deal with night-time images.

2. In Chapter 5, the transmission in each training sample used in IDSL is obtained by employing the dark channel prior (DCP) descried in [4]. However, DCP cannot fully suitable to the case where the scene brightness is naturally similar to the airlight, which would lead to IDSL also lacks the ability to deal with the images with gray-white scenes. Therefore, in the future, an adaptive adjustment of transmission is desired to overcome this limitation.

3. In Chapter 6, atmospheric conditions are required to be artificially determined in B-DPK. Therefore, seeking an adaptive approach to detect the atmospheric conditions

in hazy images is of practical significance. Moreover, considering that the weights involved in alternating minimizing technique (AMT) are empirically determined, a learning-based strategy is a good choice to pursue a set of optimal coefficients that can achieve a better balance between dehazing quality and computational efficiency.

Bibliography

[1] B.-H. Chen and S.-C. Huang, "Edge collapse-based dehazing algorithm for visibility restoration in real scenes," *Journal of Display Technology*, vol. 12, no. 9, pp. 964–970, 2016.

[2] A. Makarau, R. Richter, R. MÍźller, and P. Reinartz, "Haze detection and removal in remotely sensed multispectral imagery," *IEEE Transactions on Geoscience and Remote Sensing*, vol. 52, no. 9, pp. 5895–5905, Sep. 2014.

[3] B.-H. Chen and S.-C. Huang, "An advanced visibility restoration algorithm for single hazy images," *ACM Transactions on Multimedia Computing, Communications, and Applications (TOMM)*, vol. 11, no. 4, p. 53, 2015.

[4] K. He, J. Sun, and X. Tang, "Single image haze removal using dark channel prior," *IEEE Transactions on Pattern Analysis and Machine Intelligence*, vol. 33, no. 12, pp. 2341–2353, Dec 2011.

[5] G. R. Ceballos and V. M. Larios, "A model to promote citizen driven government in a smart city: Use case at gdl smart city," in *2016 IEEE International Smart Cities Conference (ISC2)*, 2016, pp. 1–6.

[6] E. Mardacany, "Smart cities characteristics: importance of buit environments components," in *IET Conference on Future Intelligent Cities*, 2014, pp. 1–6.

[7] Y. Y. Schechner and Y. Averbuch, "Regularized image recovery in scattering media," *IEEE Transactions on Pattern Analysis and Machine Intelligence*, vol. 29, no. 9, pp. 1655–1660, 2007.

[8] Ying Zhang and B. Guindon, "Quantitative assessment of a haze suppression methodology for satellite imagery: effect on land cover classification performance," *IEEE Transactions on Geoscience and Remote Sensing*, vol. 41, no. 5, pp. 1082–1089, 2003.

[9] D. Dai and W. Yang, "Satellite image classification via two-layer sparse coding with biased image representation," *IEEE Geoscience and Remote Sensing Letters*, vol. 8, no. 1, pp. 173–176, 2011.

[10] X. Huang, X. Guan, J. A. Benediktsson, L. Zhang, J. Li, A. Plaza, and M. Dalla Mura, "Multiple morphological profiles from multicomponent-base images for hyperspectral image classification," *IEEE Journal of Selected Topics in Applied Earth Observations and Remote Sensing*, vol. 7, no. 12, pp. 4653–4669, 2014.

[11] L. M. Linnett, D. R. Carmichael, and S. J. Clarke, "Texture classification using a spatial-point process model," *IEEE Proceedings - Vision, Image and Signal Processing*, vol. 142, no. 1, pp. 1–6, 1995.

[12] C. Brogle, C. Zhang, K. L. Lim, and T. Br?unl, "Hardware-in-the-loop autonomous driving simulation without real-time constraints," *IEEE Transactions on Intelligent Vehicles*, vol. 4, no. 3, pp. 375–384, 2019.

[13] L. Ma, J. Xue, K. Kawabata, J. Zhu, C. Ma, and N. Zheng, "Efficient sampling-based motion planning for on-road autonomous driving," *IEEE Transactions on Intelligent Transportation Systems*, vol. 16, no. 4, pp. 1961–1976, 2015.

[14] M. Aldibaja, N. Suganuma, and K. Yoneda, "Robust intensity-based localization method for autonomous driving on snowĺcwet road surface," *IEEE Transactions on Industrial Informatics*, vol. 13, no. 5, pp. 2369–2378, 2017.

[15] N. Amrouche, A. Khenchaf, and D. Berkani, "Multiple target tracking using track before detect algorithm," in *2017 International Conference on Electromagnetics in Advanced Applications (ICEAA)*, 2017, pp. 692–695.

[16] Q. Wei, "Research on automatic target acquisition and tracking in an infrared tracking system," in *2017 16th International Conference on Optical Communications and Networks (ICOCN)*, 2017, pp. 1–3.

[17] C. Mtzler, "Matlab functions for mie scattering and absorption," 2002.

[18] W. J. Wiscombe, "Improved mie scattering algorithms," *Applied Optics*, vol. 19, no. 9, pp. 1505–1509, 1980.

[19] E. J. McCartney, "Optics of the atmosphere: scattering by molecules and particles," *New York, John Wiley and Sons, Inc., 1976. 421 p.*, 1976.

[20] S. G. Narasimhan and S. K. Nayar, "Contrast restoration of weather degraded images," *IEEE Transactions on Pattern Analysis and Machine Intelligence*, vol. 25, no. 6, pp. 713–724, 2003.

[21] W. Frei, "Image enhancement by histogram hyperbolization," *Computer Graphics and Image Processing*, vol. 6, no. 3, pp. 286–294, 1977.

[22] S. M. Pizer, E. P. Amburn, J. D. Austin, R. Cromartie, A. Geselowitz, T. Greer, B. ter Haar Romeny, J. B. Zimmerman, and K. Zuiderveld, "Adaptive histogram equalization and its variations," *Computer vision, graphics, and image processing*, vol. 39, no. 3, pp. 355–368, 1987.

[23] D. J. Jobson, Z. Rahman, and G. A. Woodell, "A multiscale retinex for bridging the gap between color images and the human observation of scenes," *IEEE Transactions on Image Processing*, vol. 6, no. 7, pp. 965–976, Jul 1997.

[24] B. Funt, F. Ciurea, and J. McCann, "Retinex in matlab," *Journal of electronic imaging*, vol. 13, no. 1, pp. 48–57, 2004.

[25] Z.-u. Rahman, G. A. Woodell, and D. J. Jobson, "A comparison of the multiscale retinex with other image enhancement techniques," 1997.

[26] S. C. Huang, F. C. Cheng, and Y. S. Chiu, "Efficient contrast enhancement using adaptive gamma correction with weighting distribution," *IEEE Transactions on Image Processing*, vol. 22, no. 3, pp. 1032–1041, March 2013.

[27] J. Weickert, "A review of nonlinear diffusion filtering," *Scale-space theory in computer vision*, pp. 1–28, 1997.

[28] M.-J. Seow and V. K. Asari, "Ratio rule and homomorphic filter for enhancement of digital colour image," *Neurocomputing*, vol. 69, no. 7, pp. 954–958, 2006.

[29] K. He, J. Sun, and X. Tang, "Guided image filtering," *IEEE Transactions on Pattern Analysis and Machine Intelligence*, vol. 35, no. 6, pp. 1397–1409, June 2013.

[30] J. Kopf, B. Neubert, B. Chen, M. Cohen, D. Cohen-Or, O. Deussen, M. Uyttendaele, and D. Lischinski, "Deep photo: Model-based photograph enhancement and viewing," in *ACM transactions on graphics (TOG)*, vol. 27, no. 5. ACM, 2008, p. 116.

[31] Y. Y. Schechner, S. G. Narasimhan, and S. K. Nayar, "Instant dehazing of images using polarization," in *Computer Vision and Pattern Recognition, 2001. CVPR 2001.*

Proceedings of the 2001 IEEE Computer Society Conference on, vol. 1. IEEE, 2001, pp. I–I.

[32] S. Shwartz, E. Namer, and Y. Y. Schechner, "Blind haze separation," in *2006 IEEE Computer Society Conference on Computer Vision and Pattern Recognition (CVPR'06)*, vol. 2, 2006, pp. 1984–1991.

[33] C. O. Ancuti and C. Ancuti, "Single image dehazing by multi-scale fusion," *IEEE Transactions on Image Processing*, vol. 22, no. 8, pp. 3271–3282, Aug 2013.

[34] L. K. Choi, J. You, and A. C. Bovik, "Referenceless prediction of perceptual fog density and perceptual image defogging," *IEEE Transactions on Image Processing*, vol. 24, no. 11, pp. 3888–3901, Nov 2015.

[35] A. Galdran, J. Vazquez-Corral, D. Pardo, and M. Bertalmío, "Enhanced variational image dehazing," *SIAM Journal on Imaging Sciences*, vol. 8, no. 3, pp. 1519–1546, 2015.

[36] V. W. De Dravo and J. Y. Hardeberg, "Stress for dehazing," in *Colour and Visual Computing Symposium (CVCS), 2015*. IEEE, 2015, pp. 1–6.

[37] A. Galdran, J. Vazquez-Corral, D. Pardo, and M. BertalmÍło, "Fusion-based variational image dehazing," *IEEE Signal Processing Letters*, vol. 24, no. 2, pp. 151–155, Feb 2017.

[38] G. Fan, T. Jin, and Z. Cai, "Fusion strategy for single image dehazing," *International Journal of Digital Content Technology and Its Applications*, vol. 7, no. 1, pp. 19–28, 2013.

[39] R. T. Tan, "Visibility in bad weather from a single image," in *2008 IEEE Conference on Computer Vision and Pattern Recognition*, June 2008, pp. 1–8.

[40] R. Fattal, "Single image dehazing," *ACM transactions on graphics (TOG)*, vol. 27, no. 3, p. 72, 2008.

[41] ——, "Dehazing using color-lines," *ACM transactions on graphics (TOG)*, vol. 34, no. 1, p. 13, 2014.

[42] A. Levin, D. Lischinski, and Y. Weiss, "A closed-form solution to natural image matting," *IEEE Transactions on Pattern Analysis and Machine Intelligence*, vol. 30, no. 2, pp. 228–242, Feb 2008.

[43] D. K. Jha, B. Gupta, and S. S. Lamba, "l 2-norm-based prior for haze-removal from single image," *IET Computer Vision*, vol. 10, no. 5, pp. 331–341, 2016.

[44] S. C. Huang, J. H. Ye, and B. H. Chen, "An advanced single-image visibility restoration algorithm for real-world hazy scenes," *IEEE Transactions on Industrial Electronics*, vol. 62, no. 5, pp. 2962–2972, May 2015.

[45] L. Zeng and Y. Dai, "Single image dehazing based on combining dark channel prior and scene radiance constraint," *Chinese Journal of Electronics*, vol. 25, no. 6, pp. 1114–1120, 2016.

[46] S. C. Huang, B. H. Chen, and Y. J. Cheng, "An efficient visibility enhancement algorithm for road scenes captured by intelligent transportation systems," *IEEE Transactions on Intelligent Transportation Systems*, vol. 15, no. 5, pp. 2321–2332, Oct 2014.

[47] K. B. Gibson, D. T. Vo, and T. Q. Nguyen, "An investigation of dehazing effects on image and video coding," *IEEE Transactions on Image Processing*, vol. 21, no. 2, pp. 662–673, Feb 2012.

[48] S. C. Huang, B. H. Chen, and W. J. Wang, "Visibility restoration of single hazy images captured in real-world weather conditions," *IEEE Transactions on Circuits and Systems for Video Technology*, vol. 24, no. 10, pp. 1814–1824, Oct 2014.

[49] J. Yu, C. Xiao, and D. Li, "Physics-based fast single image fog removal," in *IEEE 10th INTERNATIONAL CONFERENCE ON SIGNAL PROCESSING PROCEEDINGS*, Oct 2010, pp. 1048–1052.

[50] C. Xiao and J. Gan, "Fast image dehazing using guided joint bilateral filter," *The Visual Computer*, vol. 28, no. 6-8, pp. 713–721, 2012.

[51] G. Meng, Y. Wang, J. Duan, S. Xiang, and C. Pan, "Efficient image dehazing with boundary constraint and contextual regularization," in *2013 IEEE International Conference on Computer Vision*, Dec 2013, pp. 617–624.

[52] B.-H. Chen, S.-C. Huang, and J. H. Ye, "Hazy image restoration by bi-histogram modification," *ACM Transactions on Intelligent Systems and Technology (TIST)*, vol. 6, no. 4, p. 50, 2015.

[53] L. He, J. Zhao, N. Zheng, and D. Bi, "Haze removal using the difference- structure-preservation prior," *IEEE Transactions on Image Processing*, vol. 26, no. 3, pp. 1063–1075, March 2017.

[54] Y. H. Lai, Y. L. Chen, C. J. Chiou, and C. T. Hsu, "Single-image dehazing via optimal transmission map under scene priors," *IEEE Transactions on Circuits and Systems for Video Technology*, vol. 25, no. 1, pp. 1–14, Jan 2015.

[55] J.-H. Kim, W.-D. Jang, J.-Y. Sim, and C.-S. Kim, "Optimized contrast enhancement for real-time image and video dehazing," *Journal of Visual Communication and Image Representation*, vol. 24, no. 3, pp. 410–425, 2013.

[56] Q. Zhu, J. Mai, and L. Shao, "A fast single image haze removal algorithm using color attenuation prior," *IEEE Transactions on Image Processing*, vol. 24, no. 11, pp. 3522–3533, Nov 2015.

[57] W. Ren, L. Ma, J. Zhang, J. Pan, X. Cao, W. Liu, and M. Yang, "Gated fusion network for single image dehazing," in *2018 IEEE/CVF Conference on Computer Vision and Pattern Recognition*, June 2018, pp. 3253–3261.

[58] L. Li, Y. Dong, W. Ren, J. Pan, C. Gao, N. Sang, and M. Yang, "Semi-supervised image dehazing," *IEEE Transactions on Image Processing*, vol. 29, pp. 2766–2779, 2020.

[59] H. Zhang, V. Sindagi, and V. M. Patel, "Joint transmission map estimation and dehazing using deep networks," *IEEE Transactions on Circuits and Systems for Video Technology*, pp. 1–1, 2019.

[60] Y. Pang, J. Xie, and X. Li, "Visual haze removal by a unified generative adversarial network," *IEEE Transactions on Circuits and Systems for Video Technology*, vol. 29, no. 11, pp. 3211–3221, Nov 2019.

[61] N. Silberman, D. Hoiem, P. Kohli, and R. Fergus, "Indoor segmentation and support inference from rgbd images," in *Computer Vision – ECCV 2012*, A. Fitzgibbon, S. Lazebnik, P. Perona, Y. Sato, and C. Schmid, Eds. Berlin, Heidelberg: Springer Berlin Heidelberg, 2012, pp. 746–760.

[62] A. Saxena, M. Sun, and A. Y. Ng, "Learning 3-d scene structure from a single still image," in *2007 IEEE 11th International Conference on Computer Vision*, Oct 2007, pp. 1–8.

[63] J. Tarel and N. HautiÍÍre, "Fast visibility restoration from a single color or gray level image," in *2009 IEEE 12th International Conference on Computer Vision*, 2009, pp. 2201–2208.

[64] W. Wang, X. Yuan, X. Wu, and Y. Liu, "Fast image dehazing method based on linear transformation," *IEEE Transactions on Multimedia*, vol. 19, no. 6, pp. 1142–1155, June 2017.

[65] M. Ju, C. Ding, D. Zhang, and Y. J. Guo, "Bdpk: Bayesian dehazing using prior knowledge," *IEEE Transactions on Circuits and Systems for Video Technology*, vol. 29, no. 8, pp. 2349–2362, 2019.

[66] ——, "Gamma-correction-based visibility restoration for single hazy images," *IEEE Signal Processing Letters*, vol. 25, no. 7, pp. 1084–1088, 2018.

[67] M. Y. Ju, Z. F. Gu, and D. Zhang, "Single image haze removal based on the improved atmospheric scattering model," *Neurocomputing*, vol. 260, pp. 180–191, 2017.

[68] T. M. Bui and W. Kim, "Single image dehazing using color ellipsoid prior," *IEEE Transactions on Image Processing*, vol. 27, no. 2, pp. 999–1009, 2018.

[69] W. Ren, S. Liu, H. Zhang, J. Pan, X. Cao, and M.-H. Yang, "Single image dehazing via multi-scale convolutional neural networks," in *Computer Vision – ECCV 2016*, B. Leibe, J. Matas, N. Sebe, and M. Welling, Eds. Cham: Springer International Publishing, 2016, pp. 154–169.

[70] B. Li, X. Peng, Z. Wang, J. Xu, and D. Feng, "Aod-net: All-in-one dehazing network," in *2017 IEEE International Conference on Computer Vision (ICCV)*, 2017, pp. 4780–4788.

[71] M. Y. Ju, D. Zhang, and X. M. Wang, "Single image dehazing via an improved atmospheric scattering model," *Visual Comput*, vol. 33, no. 12, pp. 1613–1625, 2017.

[72] H. Yuan, C. Liu, Z. Guo, and Z. Sun, "A region-wised medium transmission based image dehazing method," *IEEE Access*, vol. 5, pp. 1735–1742, 2017.

[73] G. Bi, J. Ren, T. Fu, T. Nie, C. Chen, and N. Zhang, "Image dehazing based on accurate estimation of transmission in the atmospheric scattering model," *IEEE Photonics Journal*, vol. 9, no. 4, pp. 1–18, 2017.

[74] D. Berman, T. Treibitz, and S. Avidan, "Non-local image dehazing," in *2016 IEEE Conference on Computer Vision and Pattern Recognition (CVPR)*, 2016, pp. 1674–1682.

[75] ——, "Single image dehazing using haze-lines," *IEEE Transactions on Pattern Analysis and Machine Intelligence*, vol. 42, no. 3, pp. 720–734, 2020.

[76] Y. Bahat and M. Irani, "Blind dehazing using internal patch recurrence," in *2016 IEEE International Conference on Computational Photography (ICCP)*, 2016, pp. 1–9.

[77] C. Liu, J. Zhao, Y. Shen, Y. Zhou, X. Wang, and Y. Ouyang, "Texture filtering based physically plausible image dehazing," *Visual Computer*, vol. 32, no. 6-8, pp. 911–920.

[78] Xuan Dong, Guan Wang, Yi Pang, Weixin Li, Jiangtao Wen, Wei Meng, and Yao Lu, "Fast efficient algorithm for enhancement of low lighting video," in *2011 IEEE International Conference on Multimedia and Expo*, 2011, pp. 1–6.

[79] L. Li, R. Wang, W. Wang, and W. Gao, "A low-light image enhancement method for both denoising and contrast enlarging," in *2015 IEEE International Conference on Image Processing (ICIP)*, 2015, pp. 3730–3734.

[80] X. Guo, Y. Li, and H. Ling, "Lime: Low-light image enhancement via illumination map estimation," *IEEE Transactions on Image Processing*, vol. 26, no. 2, pp. 982–993, 2017.

[81] D. Scharstein and R. Szeliski, "A taxonomy and evaluation of dense two-frame stereo correspondence algorithms," *International Journal of Computer Vision*, vol. 47, no. 1-3, pp. 7–42.

[82] D. Scharstein and R. Szeliski, "High-accuracy stereo depth maps using structured light," in *2003 IEEE Computer Society Conference on Computer Vision and Pattern Recognition, 2003. Proceedings.*, vol. 1, 2003, pp. I–I.

[83] D. Scharstein and C. Pal, "Learning conditional random fields for stereo," in *2007 IEEE Conference on Computer Vision and Pattern Recognition*, 2007, pp. 1–8.

[84] B. Cai, X. Xu, K. Jia, C. Qing, and D. Tao, "Dehazenet: An end-to-end system for single image haze removal," *IEEE Transactions on Image Processing*, vol. 25, no. 11, pp. 5187–5198, 2016.

[85] B. Li, W. Ren, D. Fu, D. Tao, D. Feng, W. Zeng, and Z. Wang, "Benchmarking single-image dehazing and beyond," *IEEE Transactions on Image Processing*, vol. 28, no. 1, pp. 492–505, 2019.

[86] N. Hautiere, J.-P. Tarel, D. Aubert, and E. Dumont, "Blind contrast enhancement assessment by gradient ratioing at visible edges," *Image Analysis and Stereology*, 2008.

[87] Zhou Wang, A. C. Bovik, H. R. Sheikh, and E. P. Simoncelli, "Image quality assessment: from error visibility to structural similarity," *IEEE Transactions on Image Processing*, vol. 13, no. 4, pp. 600–612, 2004.

[88] J. Li, Q. Hu, and M. Ai, "Haze and thin cloud removal via sphere model improved dark channel prior," *IEEE Geoscience and Remote Sensing Letters*, vol. 16, no. 3, pp. 472–476, March 2019.

[89] N. Ahmed, T. Natarajan, and K. R. Rao, "Discrete cosine transform," *IEEE transactions on Computers*, vol. 100, no. 1, pp. 90–93, 1974.

[90] Z. Gu, M. Ju, and D. Zhang, "A single image dehazing method using average saturation prior," *Mathematical Problems in Engineering*, vol. 2017, 2017.

[91] Y. Zhu, J. Liu, and Y. Hao, "An single image dehazing algorithm using sky detection and segmentation," in *2014 7th International Congress on Image and Signal Processing*, Oct 2014, pp. 248–252.

[92] S. Dai and J. Tarel, "Adaptive sky detection and preservation in dehazing algorithm," in *2015 International Symposium on Intelligent Signal Processing and Communication Systems (ISPACS)*, Nov 2015, pp. 634–639.

[93] Z. Fu, Y. Yang, C. Shu, Y. Li, H. Wu, and J. Xu, "Improved single image dehazing using dark channel prior," *Journal of Systems Engineering and Electronics*, vol. 26, no. 5, pp. 1070–1079, 2015.

[94] Bo Yuan, G. J. Klir, and J. F. Swan-Stone, "Evolutionary fuzzy c-means clustering algorithm," in *Proceedings of 1995 IEEE International Conference on Fuzzy Systems.*, vol. 4, 1995, pp. 2221–2226 vol.4.

[95] J. Wu, G. Shi, W. Lin, A. Liu, and F. Qi, "Just noticeable difference estimation for images with free-energy principle," *IEEE Transactions on Multimedia*, vol. 15, no. 7, pp. 1705–1710, 2013.

[96] T. Yu, I. Riaz, J. Piao, and H. Shin, "Real-time single image dehazing using block-to-pixel interpolation and adaptive dark channel prior," *IET Image Processing*, vol. 9, no. 9, pp. 725–734, 2015.

[97] Y. Gao, H.-M. Hu, S. Wang, and B. Li, "A fast image dehazing algorithm based on negative correction," *Signal Processing*, vol. 103, pp. 380–398.

[98] L. Kratz and K. Nishino, "Factorizing scene albedo and depth from a single foggy image," in *2009 IEEE 12th International Conference on Computer Vision*, Sept 2009, pp. 1701–1708.

[99] D. Nan, D.-y. Bi, C. Liu, S.-p. Ma, and L.-y. He, "A bayesian framework for single image dehazing considering noise," *The Scientific World Journal*, vol. 2014, 2014.

[100] W. Duochao, W. Yongguo, D. Xuemei, H. Xi-Yuan, and P. Si-Long, "Single image dehazing based on bayesian framework," *Journal of Computer-Aided Design & Computer Graphics*, vol. 22, no. 10, pp. 1756–1761, 2010.

[101] K. Nishino, L. Kratz, and S. Lombardi, "Bayesian defogging," *International journal of computer vision*, vol. 98, no. 3, pp. 263–278, 2012.

[102] J. Pan, D. Sun, H. Pfister, and M. H. Yang, "Blind image deblurring using dark channel prior," in *2016 IEEE Conference on Computer Vision and Pattern Recognition (CVPR)*, June 2016, pp. 1628–1636.

[103] Z. Shi, J. Long, W. Tang, and C. Zhang, "Single image dehazing in inhomogeneous atmosphere," *Optik-international journal for light and electron optics*, vol. 125, no. 15, pp. 3868–3875, 2014.

[104] K. Dabov, A. Foi, V. Katkovnik, and K. Egiazarian, "Bm3d image denoising with shape-adaptive principal component analysis," in *SPARS'09-Signal Processing with Adaptive Sparse Structured Representations*, 2009.

[105] J. Kim and R. Zabih, "Factorial markov random fields," in *European Conference on Computer Vision*. Springer, 2002, pp. 321–334.

[106] Y. Wang, S. Zhuo, D. Tao, J. Bu, and N. Li, "Automatic local exposure correction using bright channel prior for under-exposed images," *Signal Processing*, vol. 93, no. 11, pp. 3227–3238, 2013.

[107] X. Pan, F. Xie, Z. Jiang, and J. Yin, "Haze removal for a single remote sensing image based on deformed haze imaging model," *IEEE Signal Processing Letters*, vol. 22, no. 10, pp. 1806–1810, Oct 2015.

[108] P. S. Chavez Jr, "An improved dark-object subtraction technique for atmospheric scattering correction of multispectral data," *Remote sensing of environment*, vol. 24, no. 3, pp. 459–479, 1988.

[109] J. Long, Z. Shi, W. Tang, and C. Zhang, "Single remote sensing image dehazing," *IEEE Geoscience and Remote Sensing Letters*, vol. 11, no. 1, pp. 59–63, Jan 2014.

[110] F. Chun, M. Jian-wen, D. Qin, and C. Xue, "An improved method for cloud removal in aster data change detection," in *Geoscience and Remote Sensing Symposium, 2004. IGARSS'04. Proceedings. 2004 IEEE International*, vol. 5. IEEE, 2004, pp. 3387–3389.

[111] L. Wang, W. Xie, and J. Pei, "Patch-based dark channel prior dehazing for rs multi-spectral image," *Chinese Journal of Electronics*, vol. 24, no. 3, pp. 573–578, 2015.